Doctoral Dissertation
Doctoral Program in Mechanical Enginering (31st cycle)

Multi-scale Modelling and Design of Composite Structures

By

Yanchuan Hui
* * * * * *

Supervisors
Dr. Gaetano Giunta, Supervisor
Prof. Erasmo Carrera, Supervisor
Dr. Salim Belouettar, Supervisor
Prof. Heng Hu, Supervisor

Doctoral Examination Committee:
Prof. Lanc Domagoj, University of Rijeka, Croazia
Dr. Maiaru Marianna, Referee, University of Massachusetts Lowell
Prof. De Rosa Sergio, Università di Napoli Federico II
Prof. Dozio Lorenzo, Politecnico di Milano
Dr. Fiorenzo Fazzolari, Referee, University of Liverpool

Politecnico di Torino
December 21, 2018

I hereby declare that, the contents and organization of this thesis constitutes my original work and does not compromise in any way the rights of third parties, including those related to personal data security. Wherever the contributions of others are involved, make every effort to clearly demonstrate this and make appropriate references to the literature and acknowledge collaborative research and discussion. This work was done under the guidance of my supervisors, Dr. Giunta, Professor Carrera, Dr. Belouettar and Professor Hu.

. . . .

Yanchuan Hui

Turin, December 21, 2018

Summary

This dissertation proposes a new paradigm for Carrera's Unified Formulation (CUF) based multi-scale structural modelling by bridging micromechanics, and the advanced one-dimensional/beam structural theory. The achievements in the exploration process can be summarised in the following two aspects: a geometrically nonlinear macro-scale CUF-based beam model and a geometrically nonlinear multi-scale CUF-based beam model.

The exploration started from a study of nonlinear structural modelling established by coupling the nonlinear CUF and Asymptotic Numerical Method (ANM). This geometrically nonlinear CUF-based beam model has been accomplished in collaboration with G. De Pietro. It is one of the first studies that extends one-dimensional equivalent single layer CUF models coupled with ANM to account for geometrical non-linearities using a total Lagrangian formulation (large deformation and rotation but small strains). Static nonlinear, post-buckling and snap-through analyses of beam structures have been presented, and the corresponding load-displacement and load-stress curves have been assessed. Results have been compared with two-dimensional FEM solutions. It has been shown that, for the considered cases, a quadratic through-the-thickness description ensures accurate displacements and normal axial stress component. A higher expansion order is required to predict the shear stress component accurately, especially for very high load levels. In the considered post-buckling analysis, both high-order and low-order one-dimensional CUF models have detected the bifurcation point accurately. However, accurate results for the shear stress call for a higher-order model. In the snap-through analysis, a refined beam theory is required to accurately track the equilibrium path.

To address geometrically nonlinear problems in beam structures from different scales, a geometrically nonlinear CUF-based multi-scale beam model has been derived by coupling the proposed macroscopic model and the Multilevel Finite Element (also known as FE^2) framework, which is also the main novelty of this thesis. The solution procedure consists of a macroscopic/structural analysis and a microscopic/material analysis. At the macroscopic scale, the unknown constitutive law is derived from a numerical homogenisation of a Representative Volume Element (RVE) at the microscopic level. Vice versa, the microscopic deformation gradient is calculated from the macroscopic

model. As far as the geometrically nonlinear problem is concerned, the resulting nonlinear mathematical system is solved by ANM, which is more reliable and less time to consume compared to classical iterative methods. The proposed framework is used in investigating the effect of microscale imperfections (not straight carbon fibres) on the macroscale response (instability). Results are analysed in terms of accuracy and computational costs towards full FEM solutions. Three factors have been identified for an imperfection sensitivity parametric analysis: the wavelength, the amplitude and the size of RVE.

Sommario

Questa dissertazione propone un nuovo paradigma per l'analisi multi-scala delle strutture di tipo trave, utilizzando la formulazione unificata di Carrera ("Carrera's Unified Formulation", CUF). La modellizzazione multi-scala collega la micromeccanica e la teoria strutturale macroscopica. I risultati del processo di esplorazione possono essere riassunti nei due aspetti seguenti: un modello macroscopico di trave, contenente non-linearità geometriche, ed un modello di trave multi-scala, anch'esso non-lineare da un punto di vista geometrico.

L'indagine qui presentata inizia con uno studio della modellazione macroscopica non lineare. Il modello strutturale viene stabilito accoppiando la CUF non-lineare con il Metodo Numerico Asintotico ("Asymptotic Numerical Method", ANM). Questo modello di trave, basato sulla CUF contenente non-linearità geometriche, è realizzato in collaborazione con G. De Pietro: si tratta di uno dei primi studi che estende i modelli CUF uni-dimensionali accoppiati con il metodo ANM. Si presentano analisi non lineari statiche, post-buckling e snap-through delle strutture traviformi e se ne valutano le corrispondenti curve carico-spostamento e carico-sforzo. I risultati sono confrontati con soluzioni agli elementi finiti bidimensionali. Si dimostra che, per i casi considerati, una descrizione quadratica attraverso lo spessore garantisce accurati spostamenti a componente di tensione assiale. Inoltre, si necessita di un ordine di espansione più elevato al fine di prevedere con precisione la componente di sollecitazione di taglio. Nell'analisi post-buckling considerata, i modelli CUF di ordine basso rilevano il punto di biforcazione in modo accurato. Tuttavia, al fine di ottenere risultati accurati riguardanti la sollecitazione di taglio, si richiede un modello di ordine superiore. Nell'analisi di snap-through, è necessaria una teoria raffinata per tracciare accuratamente il percorso di equilibrio.

Per affrontare problemi contenenti non-linearità geometriche provenienti da scale diverse, un modello di trave multi-scala, basato sulla CUF contenente non-linearità geometriche, viene derivato accoppiando il modello macroscopico proposto ed il framework agli Elementi Finiti Multilivello (noto anche come FE^2). La soluzione consiste in un'analisi macroscopico/strutturale e un'analisi microscopica/materiale. Alla scala macroscopica, la legge costitutiva incognita è calcolata attraverso un'omogeneizzazione numerica di un Elemento di Volume Rappresentativo ("Representative Volume Element", RVE). Viceversa, il gradiente di deformazione microscopico è calcolato tramite modello macroscopico. Il sistema matematico non-lineare risultante è risolto attraverso il metodo

ANM, il quale risulta essere più affidabile e meno dispendioso dal punto di vista dei tempi di calcolo, rispetto ai metodi iterativi classici. La metodologia proposta viene utilizzata per studiare l'effetto delle imperfezioni alla scala microscopica (fibre di carbonio non perfettamente diritte) sulla risposta macroscopica (instabilità). I risultati vengono analizzati in termini di accuratezza e costi computazionali, rispetto alle soluzioni FEM. Tre fattori sono identificati per un'analisi parametrica di sensibilità alle imperfezioni: lunghezza d'onda ed, ampiezza della imperfezione e dimensione dell'RVE.

Acknowledgements

First, I want to express my sincere gratitude to my parents for their understanding, support and give me birth.

Secondly, words fail me when I try to express my heartfelt gratitude to my mentors Dr. Gaetano Giunta, Prof. Erasmo Carrera, Dr. Salim Belouettar and Prof. Hu Heng for enriching my life and improving my quality. Many thanks for accepting me as a PhD student and trusting me, supporting me, encouraging me, and always infusing optimism. Many thanks for giving me technical advice, supporting me through my shortcomings, showing the direction, and helping in improving myself. Many thanks for being willing to train me despite their busy schedules. Many thanks for providing me with great study and working conditions. I feel very delightful and beneficial working with these excellent researchers.

Then, my sincere gratitude is extended to Prof. Potier-Ferry, Prof. Zahrouni from University De Lorraine, Prof. Ferreira from University of Porto, Prof. Reddy from Texas A&M University, Prof. Allix from ENS Paris-Saclay, Dr. Pineda from NASA Glenn Research Centre, Prof. Yu from Purdue University, Prof. Weaver from Bristol University, Prof. Jansen from Leibniz Universität Hannover for their worthwhile advice.

Furthermore, I would like to acknowledge and sincerely thank the members of the research team from Luxembourg Institute of Science and Technology, Gabriele, Qian, Hongjian, Chuanyu, Lilia, Sachin, Arpan, Pietro, Sandra, Carlos, Abdulla, Acerina, Arnaud, Edyta, Hongtao, Alex, Damian, Gaston, Ahmed and Yao; the members of research team from Politecnico, Marco, Alfonso, Enrico, Matteo, Maria, Ibrahim, Luca, Riccardo, Alberto, Manish, Bin; and the members of research team from Wuhan University, Fu, Qian, Yin, Kun, Qun, Jie, Wei, Rui, Jian, Jongchol, Jianan, Wei, Zengtao; the other members from the FULLCOMP project, Georgios, Pietro, Lorenzo, Mayank, Sergio, Sander, Margarita. It is very fortunate for me to learn knowledge, share ideas, and communicate with you.

Last but not least, I wish to thank my PhD committee members for their expertise, precious time and valuable advises.

This dissertation is lovingly dedicated to my mother and my father.

Contents

List of Tables

List of Figures

XIV

xv

Chapter 1

Introduction

1.1 Background

In this thesis, a multi-scale framework for nonlinear problems is developed using a FE^2 approach where at macro-scale CUF higher-order structural theories are used, and the resulting non-linear problem is solved by means of the advanced ANM nonlinear solver.

In continuum and structural mechanics, the objects under investigation are usually macroscopic structures, which are made of some given materials. Materials can be classified as homogeneous and heterogeneous. Homogeneous materials are formed of a single component with a uniform spatial distribution, some examples being metals, alloys or plastics. Heterogeneous materials are composed of a plurality of components or a single component with a non-uniform spatial distribution. Fibre-reinforced materials are an example of this class. They are formed from two components: a matrix and a fibre, allowing to increase overall strength and stiffness (see Petrone et al. [136]).

For addressing the mechanical problems of heterogeneous materials, a multi-scale modelling accounting for both structural and material level has been proposed in the literature in order to improve accuracy and efficiency. Multi-scale modelling refers to a modelling approach in which multiple models of different scales are employed simultaneously to describe the system under investigation to achieve a reasonable compromise between accuracy and efficiency (see E and Lu [52]). This approach has been suggested to overcome some issues presented by separate structural level/macroscopic modelling and material-level/microscopic modelling. First, a single structural-level/macroscopic model neglects interactions between different components at the material level, the response at material level caused by the reaction of the macroscopic structure and the change of the macroscopic material properties. For instance, macroscopic failure might originate from microscopic instabilities, defects and cracks (see Jochum and Grandidier [98]). If these interactions between material and structural level are neglected, a model at structural level cannot accurately describe the problems under investigation, especially when considering nonlinearity. In a nonlinear problem, the response not only

depends on the initial state but also on the evolution of the material properties and the geometric features. Secondly, it is cumbersome and often impossible to start modelling directly from the microscopic scale considering the vast requirement of computing resources. A composite structure consists of several representative units, and a representative unit contains several single phases. Thus, the geometric dimensions of a single phase are much smaller than that of a single unit, which is much smaller than the entire structure. If FEM is applied at the finest scale, the element size should be smaller than a representative size of a single phase to ensure accuracy. This level of mesh refinement requires a prohibitive computational cost.

Multiscale methods are gradually being adopted by the industry, and there are already some software products based on semi-analytical and numerical methods, such as DIGI-MAT or SwiftComp. Many multiscale software developers came from research institutes or universities. This trend has also promoted the use of many of the latest theories and techniques.

As far as macro-scale modeling is concerned, in different engineering sectors, one-dimensional/beam, two-dimensional/plate or three-dimensional/solid composite structures are widely applied. It can be beneficial to straightforwardly connect micromechanics with structural theories, especially for the one-dimensional/beam structures. For example, beam theories reduce the number of problem dimensions from three to one, thus significantly reducing the total number of unknown variables. However, classical structural theories are not always applicable due to an expansion of the application range of heterogeneous materials (see Giunta [74]). Carrera's Unified Formula (CUF) is a powerful framework to accurately describe beams, plates and shells with a significant improvement in computational efficiency. Using CUF, accurate results can be obtained by assuming a suitable high-order model, which is especially evident when addressing short beams. CUF advanced theories are here coupled in a FE^2 sense to micromechanical finite element homogenisation and localisation.

For the general linear problem of multi-scale modelling, the solution involves only one step, more specifically, one homogenisation and localisation. However, for a nonlinear geometric problem in a multi-scale framework, this requires multiple homogenisations and localisations, resulting in an exponential increase of the computational cost. Especially for the multi-scale analysis of problems presenting a strong nonlinearity, in the process of tracking the solution path, as the solution step length becomes smaller and smaller, the number of solution steps increases. Compared with the structural-level model, the calculation needed in one more step is far more expensive in a multi-scale problem. Consequently, the rise in computational costs has prompted an urgent need for an accurate and efficient nonlinear solver. This solver should be able to accurately track the nonlinear equilibrium path while minimising the number of solution steps. The asymptotic numerical method (ANM) nonlinear solver is a very good choice to address this aspect since it ensures accurate yet efficient path tracking for strong nonlinear problems. Finally, the multi-scale finite element (FE^2) framework enables nesting macroscopic and microscopic models.

1.2   Outline of the Thesis

This thesis is divided into three parts: a literature review presented in Chapter 2, the theoretical developments addressed in Chapter 3 and Chapter 4 and, finally, some numerical results shown in Chapter 5 and Chapter 6. The layout of each chapter is briefly outlined:

- Following this introductory chapter, a review of beam theories, multiscale methods and nonlinear solvers is presented in Chapter 2.

- Chapter 3 focuses on the description of the structural model for geometrically nonlinear analyses. Within the framework of a total Lagrangian approach, a finite element solution based on nonlinear CUF is provided. More specifically, highly nonlinear problems, such as post-buckling and snap-through problems are considered. The critical points for coupling ANM and CUF are there all presented.

- In Chapter 4, a model for the geometrically nonlinear multiscale problems analysis is derived. The theoretical derivation of this model is an extension of what addressed in Chapter 3. Homogenisation and localisation are derived under the framework of the FE^2 method.

- Chapter 5 presents some numerical examples of the proposed non-linear structural model. Post-buckling and snap-through analyses are carried out. Results are compared in terms of accuracy and computational costs towards FEM solutions using solid finite elements.

- Chapter 6 addresses some numerical analyses where the proposed multiscale modelling has been used. The case of a heterogeneous material with a round inclusion is first presented. The case of a fibre-reinforced material is then studied with particular attention being paid in assessing the effect of imperfections.

- Conclusion and outlooks are provided in Chapter 7.

3

Chapter 2

State of the Art

To the best of this author's knowledge, a brief review is conducted for a handful of widely used beam theories, multi-scale methods and nonlinear solvers. Section 2.1 presents the summary of beam theories, including the classic beam theories, Vlasov-Reddy beam theory, generalised beam theory and Carrera's unified formula. Section 2.2 focuses on the multi-scale methods, which are classified into solving the RVE/UC problem and building the link for the multi-scale problem. The methods for addressing the RVE problems are categorised as analysis, semi-analysis and numerical methods. As for building the link for the multi-scale problem, fine-scale oriented and coarse-scale oriented methods are presented. In Section 2.3, the nonlinear solvers are grouped into the path-corrector methods and perturbation methods.

2.1   Review of the Beam Theories

For the structural analysis, slender structures usually can be simplified into beams. In essence, a beam model is to transform the three-dimensional problems into a set of one-dimensional variables. These variables are only subject to the coordinates along the axis. Since the size of the thickness is much minor than the size of the length, it can be approximated that the components of the displacement, strain, and stress are distributed based on the thickness. Therefore, beam theories are much simpler plate/shell or solid theories. The calculation efficiency is also much higher with the reduction of unknowns. Due to these excellent features, beam theories are still very appealing for various static and dynamic analyses.

Started by Leonardo da Vinci, beams were studied theoretically. The proof is a manuscript called "Madrid Codex" written in 1493 (see Carrera et al. [134]). For a thin beam, a correct description is shown for the bending behaviour. Besides, the well-known hypothesis was made: the axial strain on the cross-section is distributed linearly. In 1638, the

earliest systematic study of beam structures was proposed by Galilei Galileo in the "Dialogues concerning two new sciences". In this book, he proposed two questions about beam theory: one is the strength of the cantilever beam. The other is the strength of the beam under its weight. Since the neutral surface of the beam is taken on the underside of the beam, the proposed problem is not solved correctly. In 1826, the neutral surface problem was solved by Navier Claude-Louis in "Mechanical and Structural Applications in Mechanics". An accurate definition is given: the neutral surface passes through the centroid of the section. In 1856, de Saint-Venant gave general references and solutions to the problem of bending and torsion of beams. The concept of a curved centre is provided, and the cylinder does not twist when the resultant force of the lateral forces passes through the centre of the bend. By controlling the position at which the external force generates a lateral force, it is possible to avoid the occurrence of bending and torsion coupling of the beam. At the same time, the method of calculating the centre position of the bend on the section is also deduced. A Cartesian coordinate system is adopted in this section for the beam structures as depicted in Fig. 2.1,
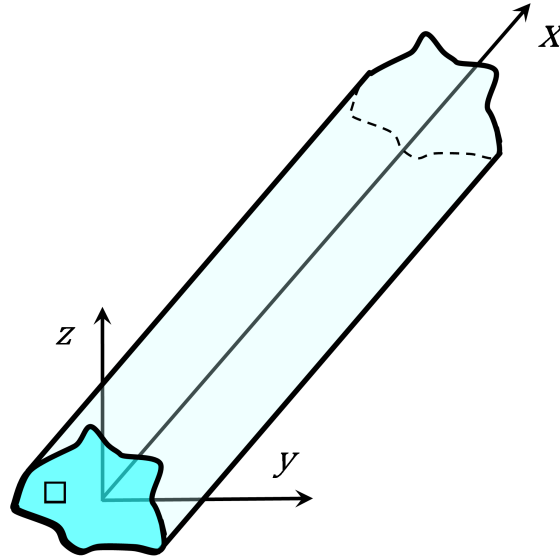
Figure 2.1: A beam structure in the Cartesian coordinate system.

where "□" stands for the cross-section, which is achieved by intersecting the beam structure with a plane orthogonal to its axial direction. y- and z-axis symbolise two orthogonal directions laying on □. The extension on the axial direction "x" is higher than any other dimension orthogonal to it.

$$\mathbf{u}^T(x, y, z) = \left\{ \ u_x(x, y, z) \quad u_y(x, y, z) \quad u_z(x, y, z) \ \right\} \tag{2.1}$$

where u_x, u_y and u_z are the displacement components along x-, y- and z-axis, respectively. The transposition operator is addressed by superscript 'T'.

2.1.1 Classical Theory: Euler Bernoulli Beam Theory (EBBT)

From the perspective of deformation, the first accurate study of the beam is started from the EBBT theory. It was invented by Leonhard Euler and Johann Bernoulli in 1705, it was not the previous study of beams from stress, but the earliest use of calculus tools to study beam deformation. This theory assumes that the cross-section is still flat and keeps perpendicular to the midplane of the beam after deformation. The transverse shear effect in cross-sectional deformation is not considered. Based on this assumption, the derived differential equation of the deformation of the cantilever beam is represented by the displacement of the beam centreline. Within this theory, the displacement field is written as

$$
\begin{aligned}
u_x &= u_{x1} - u_{y1,x}y - u_{z1,x}z, \\
u_y &= u_{y1}, \\
u_z &= u_{z1}
\end{aligned}
\tag{2.2}
$$

u_{x1}, u_{y1} and u_{z1} respectively represent the first-order components of the displacement in the x, y, and z direction. As a consequence of the neglecting the shear strain, deflection is underestimated, but natural frequencies and buckling loads are overestimated. Therefore, a more refined beam theory is in need.

2.1.2 Classical Theory: Timoshenko Beam Theory (TBT)

As one of the most adopted first-order beam theories, the TBT is developed by Timoshenko (see Carrera et al. [26]). Regarding the deformation of the beam, the following assumption is made: the cross-section perpendicular to the midplane of the beam remains flat after deformation, but it is no longer assumed to be the midplane after vertical deformation. The displacement of each point in the beam can be represented by the axial displacement and the angle of the thickness direction. That is, along with the thickness of the beam, the shear deformation is continuous, and shear stress is constant. The value of stiffness decreased compared to the EBBT. The displacement field is written as

$$
\begin{aligned}
u_x &= u_{x1} + u_{x2}y + u_{x3}z, \\
u_y &= u_{y1}, \\
u_z &= u_{z1}
\end{aligned}
\tag{2.3}
$$

In TBT, the shear correction coefficient is neglected. Consequently, the shear stress and strain components are constant along the thickness. By employing TBT, Timoshenko and Gere [159] studied the linear bifurcation problems of thin-walled beams. Song and Waas [152] presented a buckling analysis on laminated beams by employing the EBBT,

TBT and a simple three-order beam theory, where no coefficient correction is introduced for each order. Compared to the simple three-order beam theory, TBT still can be regarded as a practical solution. However, the TBT's assumption about the distribution of shear stress is not appropriate, because the top and bottom surfaces are under zero loading. Mindlin and Deresiewicz [124], Cowper [36] calculated the shear coefficient to correct strain energy. The shear coefficient is determined by the geometry of the cross-section. At the same time, as more and more advanced composite materials are adopted in engineering, further development on beam theories is needed to eliminate the limitations of this theory.

2.1.3   Higher-order Theory: Vlasov-Reddy Theory

For improving the TBT, additional higher-order terms are needed to reflect the local effect in displacement fields. This initial work is introduced by Vlasov [162] and Reddy [141]. This improvement aims at meeting the requirement of zero shear strain/stress condition. Meanwhile, these terms should be limited by their corresponding coefficients. One of the most prominent theories is Vlasov-Reddy Theory as follows.

$$
\begin{aligned}
u_x &= u_{x1} + f_1(y)\phi_z + f_2(z)\phi_x + g_1(y)u_{z1,x} + z\phi_{x,x} + g_2(z)u_{z1,x} - z\phi_{x,x}, \\
u_y &= u_{y1} + z\phi_x, \\
u_z &= u_{z1} - y\phi_x
\end{aligned}
\tag{2.4}
$$

in which $f_1(y)$, $g_1(y)$, $f_2(z)$ and $g_2(z)$ are three-order functions. They are related to the y and z coordinate along the thickness.

$$
\begin{aligned}
f_1(x) &= x - \frac{4}{3b^2}x^3, \\
g_1(x) &= -\frac{4}{3b^2}x^3, \\
f_2(z) &= z - \frac{4}{3h^2}z^3, \\
g_2(x) &= -\frac{4}{3h^2}z^3,
\end{aligned}
\tag{2.5}
$$

In which the b is the width along the y axis, and h is the height along the z axis.
This theory was applied to the linear bifurcation problems of thin-walled beams by Vlasov [162], and further used for bending and free-vibration analysis by Thai and Vo [156] and buckling analysis by Lanc et al. [110]. The Euler-Bernoulli and Timoshenko models can be derived in this theory as special cases. However, Vlasov-Reddy beam theory is not sufficient when considering more complex engineering problems, such as warping outside the plane. Therefore, several higher order beam theories are proposed to meet the requirements. It is because the precise displacement field captures small value perturbation with respect to displacement and results in more accurate results. However, it leads to more computational cost. Therefore, It is better to select the appropriate order of beam theories according to the need. It is very comfortable to make the process of selection automated. Carrera's Unified Formulation realises this magnificent

contribution (refer to subsection 2.1.7).

EBBT, TBT and higher-order theory can be referred to as the axiomatic hypothesis method. These approaches are systematically summarised by Kapania and Raciti [102]. In his article, buckling and post-buckling studies of beam theories, as well as the implementation process combined within the FEM framework are also well reviewed.

2.1.4 Asymptotic Method

The asymptotic method in beam theories refers to the variational asymptotic method proposed by Berdichevsky [14] and Volovoi et al. [163], which establishes the deformation-based model by studying the effects of various variables on the disturbance parameters. The disturbance parameter is usually a small value parameter of the geometry, such as the height-to-length ratio of the beam. At the same time, the name "asymptotic method" also exists in multi-scale methods and nonlinear solvers. They share the same basic idea of expanding the function with a small-valued parameter.

First, expand the characteristic parameters (e.g. deformation) into series according to the disturbance parameter. Secondly, construct the strain energy according to the characteristic parameters. Then, retain those terms having the same order of magnitude as the disturbance parameters. Finally, obtain the unknown function by minimising the strain energy. Compared with axiomatic theory such as EBBT and TBT, the development of asymptotic theory is more difficult (see Carrera et al. [23]). However, when the characteristic parameter is taken to be zero, this theory can obtain an exact solution. This theory was gradually improved, and the research problem was extended from the bending and twisting problems to the warping problem (see Hodges [83]). After that, Cesnik and Hodges. [31] compiled the variational asymptotic beam sectional analysis (VABS) code, which aims at dealing with modelling of the rotor blades.

2.1.5 Generalised Beam Theory (GBT)

GBT is an analytical method initially developed by Schardt [149]. Warping in cross-section is a foremost consideration in the characterisation of thin-walled beams. In this theoretical framework, the beam structure is considered to have a deformable cross-section. A variety of cross-sectional characteristics are defined as parameters. Some of them are employed to describe the deformation of the whole structure, and some of them are also applied to characterise the deformation of the cross-section. In the first-order GBT (see Davies and Leach [43]), the first-order derivation of the cross-section parameters are employed to calculate the stress and deflection within the cross-section. In the second-order GBT (see Davis et al. [44]), the second-order derivation of the cross-section parameters are utilised to solve the buckling problem. Additionally, the third-order GBT (see Chiu [33]) is proposed for the study of post-buckling with large deflection behaviour. Dinis [47] further extended the theory to analyse buckling deformation. Based on this analysis, an improved model is proposed by Basaglia and Camotim [10]

for global and local buckling problems.

2.1.6 Beam Theory based on Saint-Venant Solution

Combined with Hook's law and force boundary conditions, when the values of the body and surface forces are zero, solving the three-dimensional elastic equation is a classic Saint-Venant solution. When the body and surface force densities are not limited, it is called the extension of the Saint-Venant solution or the Almansi-Michell solution (see Michell [121]), which was solved by Iesan [97]. For settling the problem of beam structures, Ladevèze and Simmonds [108] proposed an approach by reducing the three-dimensional elastic equation and extended the classic Saint-Venant solution for the non-symmetrical cross-section. The result of solving the equation consists of two parts, the Saint-Venant part and the residual part. Dong et al. [48] deduced the extension of the Saint-Venant solution to a non-uniform cross-section of an anisotropic material. As a continuous work, Ladevèze et al. [107] applied this solution to study anisotropic elastic tubes with arbitrary closed sections.

2.1.7 Carrera's Unified Formula (CUF)

Carrera's Unified Formulation is a framework for efficiently deriving higher-order structural (plates, shells and beams) theories. The acronym, CUF, first appeared Demasi [45], whereas before it was known as Unified Formulation (UF). CUF uses index notation to unify structural theories development in one single formula. As far as beam modelling is concerned, CUF was first applied to the study of beams by Carrera and Giunta [25] and Carrera et al. [26]. Over the cross-section, the kinematic field is axiomatically assumed along the thickness as follows:

$$\mathbf{u}(x, y, z) = F_\tau(y, z)\, \mathbf{u}_\tau(x) \quad \text{with} \quad \tau = 1,\, 2,\, \dots,\, N_u. \tag{2.6}$$

According to Einstein's notation, the subscript τ stands for the implicit summation convention. $F_\tau(y, z)$ indicates the functions of the cross-section coordinates y and z, and N_u denotes the number of accounted terms. $\mathbf{u}_\tau$ is an unknown function of the axial coordinate whose form depends upon the solution method.

It is arbitrary to select the expansion functions $F_\tau(y, z)$ and order N_u. Therefore, several higher-order beam theories can be obtained by changing them. Mac Laurin's polynomials are first employed as approximating functions F_τ. As functions of the theoretical order N, both N_u and F_τ are obtained from Pascal's triangle, see Table 2.1.

N	N_u	F_τ
0	1	$F_1 = 1$
1	3	$F_2 = y \quad F_3 = z$
2	6	$F_4 = y^2 \quad F_5 = yz \quad F_6 = z^2$
3	10	$F_7 = y^3 \quad F_8 = y^2z \quad F_9 = yz^2 \quad F_{10} = z^3$
$\vdots$	$\vdots$	$\vdots$
N	$N_u^{(a)}$	$F_{N_u-N} = y^N \quad F_{N_u-N+1} = y^{N-1}z \quad \dots \quad F_{N_u-1} = yz^{N-1} \quad F_{N_u} = z^N$

(a): $N_u = \frac{(N+1)(N+2)}{2}$

Table 2.1: Mac Laurin's polynomials terms via Pascal's triangle.

Consequently, the explicit form of a generic N-order displacement field can be written as

$$
\begin{aligned}
u_x &= \underbrace{u_{x1}}_{0} \underbrace{+u_{x2}y + u_{x3}z}_{1} + \dots \underbrace{+u_{x(N_u-N)}y^N + \dots + u_{xN_u}z^N}_{N}, \\
u_y &= u_{y1} +u_{y2}y + u_{y3}z + \dots +u_{y(N_u-N)}y^N + \dots + u_{yN_u}z^N, \\
u_z &= u_{z1} +u_{z2}y + u_{z3}z + \dots +u_{z(N_u-N)}y^N + \dots + u_{zN_u}z^N.
\end{aligned}
\tag{2.7}
$$

Lagrangian Polynomials (see Carrera and Petrolo [29]), Chebyshev Polynomials (see Filippi et al. [61]), Legendre Polynomials (see Carrera et al. [27]), and Newton Polynomials (see Giunta et al. [76]) were also used in the framework of CUF. Regarding the displacements variation along the axial direction, a one-dimensional finite element approximation is employed:

$$
\mathbf{u}(x, y, z) = F_\tau(y, z)\, N_i(x)\, \mathbf{q}_{\tau i} \quad \text{with} \quad \tau = 1, 2, \dots, N_u \quad \text{and} \quad i = 1, 2, \dots, N_n^e. \tag{2.8}
$$

where $N_i(x)$ is a C^0 shape function. N_n^e indicates the number of nodes per element and $\mathbf{q}_{\tau i}$ denotes the nodal displacement unknown vector. The specific form of shape functions $N_i(x)$ is not presented. It can be found in Bathe [11]. By employing $F_\tau(y, z)$ and $N_i(x)$, the displacement field is grouped into two parts as shown in Fig 2.2.
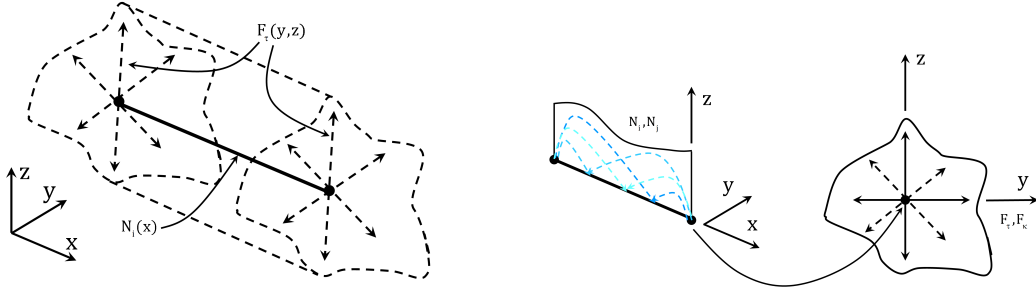
(a) Beam approximation   (b) Axial approximation and cross-section approximation

Figure 2.2: Under the framework of CUF, beam models are separated as the axial approximation and the expansion over the cross-section.

By introducing CUF into the variational principle, the governing equations of any order can be derived in a simple and elegant form for beam models. A nucleus form for the stiffness and mass matrix can be obtained. This form depends on the approximation of the displacement field. By choosing proper approximation orders, results can be achieved both accurately and efficiently. The versatility of CUF is one of its significant advantages. Carrera and Ciuffreda [21] provided solutions for Navier analytical types, while Carrera and Demasi [22] offer solutions to FEM numerical types. Under the framework of this approach, the derivation is made formally general regardless the through-the-thickness approximating functions. He et al. [79] coupled the CUF with Arlequin Method (see Hu et al. [86], Hu et al. [87]) to build a meso-macro coupling sandwich model. Based on the CUF high-order beam theory, Miguel et al. [123] generated a microscopic model through the Legrende-type interpolation. Recently, CUF was exploited to build a Component-Wise (CW) model (see Carrera et al. [28] and Maiarú et al. [114]), which can be applied as an efficient approach for fibre-reinforced materials with periodic microstructures. This CW model was adopted for studying the microscopic progressive failure by Kaleel et al. [99]. It is worth mentioning that, Pagani and Carrera [135] deduced CUF format based on total Lagrangian formulation with consideration of geometric nonlinearity. This work is one of the theoretical foundations of the macroscopic model for this thesis.

As the laminated structures get more applications in engineering, the corresponding theories are also developed including the equivalent single layer theory, layerwise theory, and zigzag theory (see Carrera [20] and Hu et al. [89]). These laminated-structural theories were also realised under the framework of CUF by Carrera and Giunta [24], Ciunta et al. [75]. It is worth mentioning that in recent years, on the basis of CUF-based laminated model from D'ottavio and Carrera [39], D'Ottavio [41] proposed the Sublaminate Generalised Unified Formula (S-GUF), which can be regarded as an extension of the symbol system defined by the CUF framework to the laminated structures. That is, considering the laminated structures with any number of layers, each sub-layer can adopt

any kinematic formula, and each sub-layer has a clear associated polynomial. Recently, S-GUF was exploited to resolve the buckling and wrinkling problems by D'Ottavio et al. [40] and Vescovini [161].

2.2 Review of the Multi-scale Methods: Information Passing Methods/Upscaling Methods

Multi-scale methods can be grouped into information-passing/upscaling/sequential and concurrent approaches (see Kanouté et al. [101], Geers et al. [69], Klusemann and Svendsen [103], Fish [63], E and Lu [52]). If a fine-scale (or micro-structural) model and a coarse-scale (or structural) model coexist in the same region, the problem is solved by employing information-passing methods. If fine-scale models and coarse-scale models exist in different regions that may be disjoint or overlapping, the problem is solved by employing the concurrent methods, which process simultaneously at least two regions involved different scales. This section focuses on upscaling methods.

Upscaling approaches are based on the concept of scale separation. To quantitatively separate the different scales, the scale separation assumption is introduced and has the following expression:

1. Atomic and nanoscale: representative size of this scale is less than 1 μ m. Quantum mechanics or nanomechanics must be applied.

2. Microscale and mesoscale: the scale is between 1 μm and 1 mm. When the analysis is at this scale, it is solved under the framework of micromechanics and continuum mechanics.

3. Macroscale: This scale is higher than 1mm. The problem is also solved in the framework of continuum mechanics or structural mechanics.

It is worth mentioning that the definitions of mesoscale and microscale have not been unified yet, in other words, they are still controversial. This thesis deals with the latter two scales, microscale and macroscale.

A multi-scale method should be able to pass the Accuracy and Cost Requirement (ACR) test (see Fish [62]):

$$\begin{array}{c} \text{Error in quantities of interest} \leq \text{tolerance,} \\ \dfrac{\text{Cost of the multi-scale model}}{\text{Cost of the microscale model}} \ll 1 \end{array} \quad . \tag{2.9}$$

To pass the test, some prerequisites should be satisfied. Consequently, before constructing a multi-scale model, assumptions such as ***scale separation*** and ***self-similarity***

need to be met. Scale separation means that the characteristic lengths of the different scales are well separated (see Hou [84]). As shown in Fig 2.3, the discrete feature-length at the microscale $\ell_{discrete}$ is usually less than, or equal to, the shortest distance between two inclusions, which is assumed to be much smaller than the microscopic feature-length ℓ_{micro}, while the latter is much smaller than the macroscopic feature-length ℓ_{macro}. The following relation should be satisfied:

$$\ell_{discrete} \ll \ell_{micro} \ll \ell_{macro}. \tag{2.10}$$

Self-similarity means that shapes/patterns of structures observed at different scales
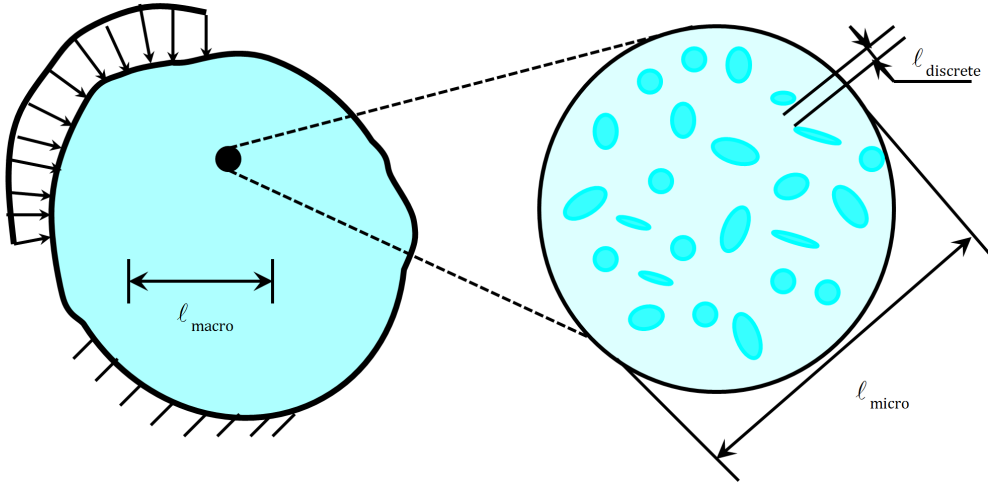
Figure 2.3: Schema of scale separation, which is reproduced based on the work of Matouš et al. [117]

are geometrically similar. A representative example is the Sierpinski triangle shown in Fig 2.4. For self-similar structures, a kinematic model with a continuous sequence form can be established. The function of several parameters (such as strain) can be transformed into a power series, which depends on its exponent called the scaling parameter (see E and Yue [53] and Dyskin [50]). In this model, the most elementary microstructure can be seen as a RVE. Meanwhile, the self-similarity, being a strong constraint, inheres between the macroscale and the RVE.

For the information passing methods/upscaling methods, building the link for the multi-scale problem and solving the UC/RVE problem are two main topics.
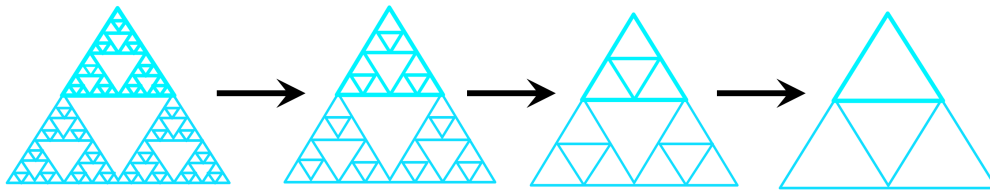
Figure 2.4: Schema of Sierpinski triangles.

2.2.1 Solving the UC/RVE problem
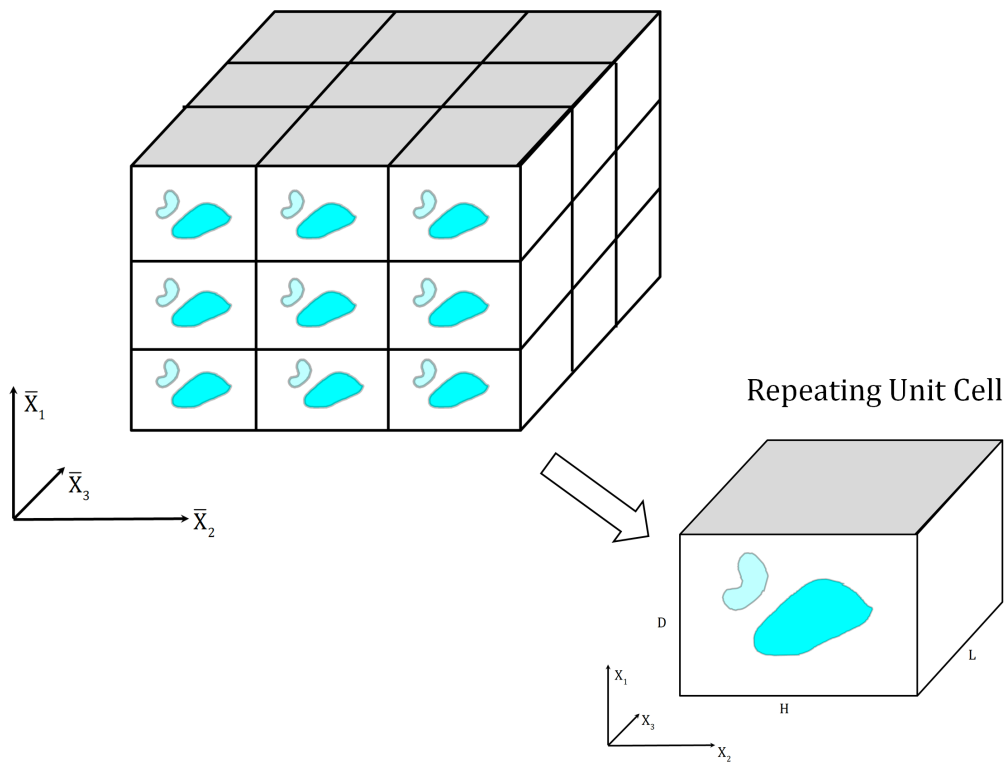
Figure 2.5: A heterogeneous composite with periodic microstructures and the RUC, which is reproduced based on the work of Aboudi [3].

Three concepts need to be clarified in the beginning: 1) UC, 2) Repeating Unit Cell (RUC) and 3) RVE. UC is a basic microstructure taken for analysis. The physical length is arbitrary. As shown in Fig 2.5, if UCs are arranged by repeating each other in a domain, they are RUCs. The periodicity of the microstructure is considered. As a type of UC,

RUC also has no relevant physical length limitation. However, its spatial arrangement must be orthogonal due to its underlying assumption.

RVE is defined as a sufficiently large volume to characterise the microstructure adequately. Firstly, It should be representative. All microscopic distribution characteristics should be covered. Secondly, it should be small enough. Meanwhile, an associated physical length must be given. Both the shape and size requirements of RVE is broader than UC or RUC. The selection of its size or shape is not unique as shown in Fig. 2.6. However, the size of RVE has a specific impact on the convergence as shown in Fig. 2.7. There are three kinds of boundary conditions considered: Periodic, linear displacement and uniform traction boundary condition. When the RVE size is small, the convergence speed is fast under periodic boundary conditions. When the RVE size is large, the convergence of the three boundary conditions tends to be uniform. If the microstructure lacks periodicity, instead of RVE, statistical volume elements should be used in the framework of stochastic micromechanics (see Schröder [150]).

To be noticed, scale separation can be considered to be satisfied when the number of RVE/UCs is infinite.
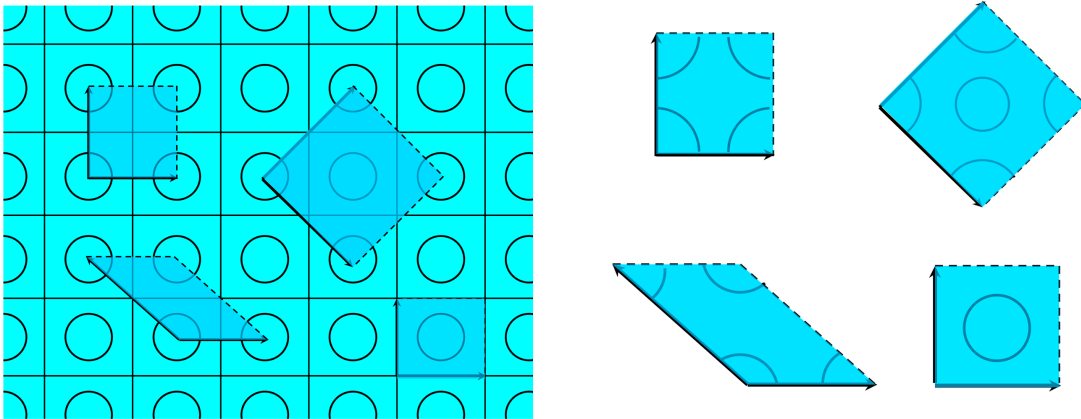
Figure 2.6: RVE with periodic structure selection is not unique, which is based on the work of Schröder [150].
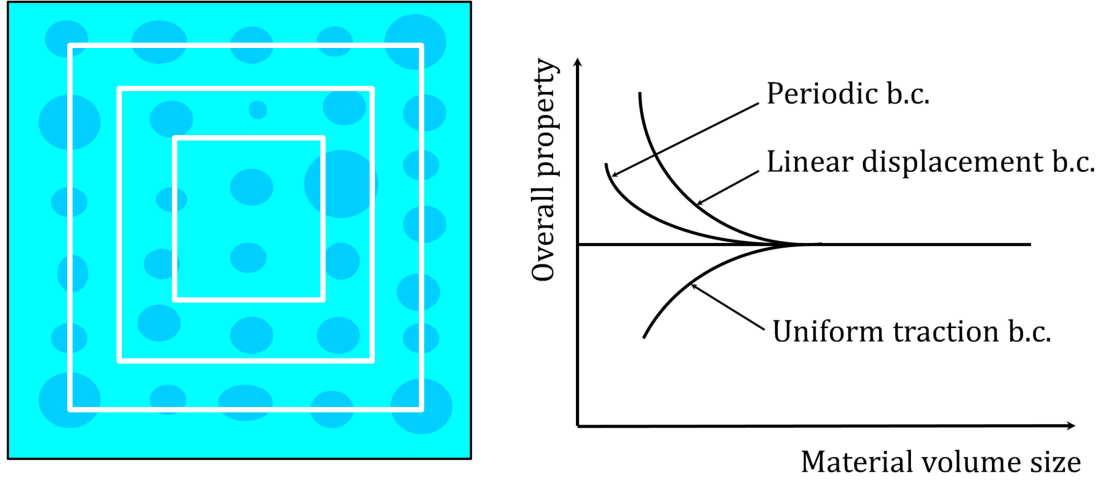
Figure 2.7: RVE size and convergence under different boundary conditions, which is reproduced based on the work of Terada et al. [154].

Analytical Method

For solving the problem of UC/RUC, analytical methods are first proposed. Here is a brief review of Hill-Reuss-Voigt Bounds, Self-consistent Method and Mori-Tanaka method.

Hill-Reuss-Voigt Bounds. Hill-Reuss-Voigt Bounds are applied to predict the upper and lower bounds for predicting the effective property of UC/RVE. In the beginning, Voigt (Taylor) assumption and Reuss (Hill) assumption [144] are applied for structural level. Then, it is proposed by Hill [82] by extending these assumption to micromechanics. The underlying assumption is the macroscopic constitutive tensor $\overline{C}_{ijkl}$ is obtained from the area average of the microscopic constitutive tensor C_{ijkl} as

$$\overline{C}_{ijkl} = \frac{1}{|\omega|} \int_{\omega} C_{ijkl} d\omega. \tag{2.11}$$

where ω is the microscopic domain, and "$|\omega|$" represents the modulus of ω. $\overline{C}_{ijkl}$ and C_{ijkl} represents the macroscopic and microscopic constitutive tensor, respectively. To be noticed, the macroscopic variables are marked with an overline "$\overline{\cdot}$" in this chapter.

Voigt (Taylor) assumption. The strain of coarse scale $\overline{\epsilon}_{ij}$ equals the fine scale ϵ_{ij}:

$$\overline{\sigma}_{ij} = \overline{C}_{ijkl}^{Voigt} \overline{\epsilon}_{kl} = \overline{C}_{ijkl}^{Voigt} \epsilon_{kl}. \tag{2.12}$$

17

$\overline{C}_{ijkl}^{Voigt}$ is the Voigt's macroscopic constitutive tensor as follows

$$\overline{C}_{ijkl}^{Voigt} = \frac{1}{|\omega|} \int_{\omega} C_{ijkl} d\omega. \tag{2.13}$$

Reuss (Hill) assumption. The stress of coarse scale $\overline{\sigma}_{ij}$ equals the fine scale σ_{ij}:

$$\overline{\epsilon}_{ij} = (\overline{C}_{ijkl}^{Reuss})^{-1}\overline{\sigma}_{kl} = (\overline{C}_{ijkl}^{Reuss})^{-1}\sigma_{kl}. \tag{2.14}$$

$\overline{C}_{ijkl}^{Reuss}$ is the Reuss's macroscopic constitutive tensor as

$$\overline{C}_{ijkl}^{Reuss} = (\frac{1}{|\omega|} \int_{\omega} (C)^{-1} d\omega)^{-1}. \tag{2.15}$$

The strain in fine scale is decomposed into two parts including the strain from the coarse scale $\overline{\epsilon}_{ij}$ and the fluctuation/perturbation ϵ_{ij}^*:

$$\epsilon_{ij} = \overline{\epsilon}_{ij} + \epsilon_{ij}^*. \tag{2.16}$$

Likewise, the stress can also be decomposed as the stress from the coarse scale and the fluctuation/perturbation:

$$\sigma_{ij} = \overline{\sigma}_{ij} + \sigma_{ij}^*. \tag{2.17}$$

The upper bound Because C_{ijkl} is positively defined, it can be derived as:

$$\begin{aligned} 0 &\leq \frac{1}{|\omega|}\epsilon_{ij}^* C_{ijkl}\epsilon_{kl}^* d\omega \\ &= \frac{1}{|\omega|}(\epsilon_{ij} - \overline{\epsilon}_{ij})C_{ijkl}(\epsilon_{kl} - \overline{\epsilon}_{kl})d\omega \\ &= \overline{\epsilon}_{ij}(\frac{1}{|\omega|} \int_{\omega} C_{ijkl} d\omega - \overline{C}_{ijkl})\overline{\epsilon}_{kl} \end{aligned} \tag{2.18}$$

By using the Eq. (2.13), it becomes:

$$\overline{\epsilon}_{ij}(\overline{C}_{ijkl}^{Voigt} - \overline{C}_{ijkl})\overline{\epsilon}_{kl} \geq 0. \tag{2.19}$$

It leading to a form as follows:

$$\alpha_{ij}\overline{C}_{ijkl}^{Voigt}\alpha_{kl} \geq \alpha_{ij}\overline{C}_{ijkl}\alpha_{kl} \ \forall \alpha_{ij} \tag{2.20}$$

Therefore, it is called the upper bound condition.
The lower bound Compliance tensor M_{ijkl} is defined as:

$$M_{ijkl} = \frac{1}{C_{ijkl}}. \tag{2.21}$$

Likewise, another equation can be obtained since the internal work should be equal to or larger than zero (due to $C_{ijkl} \geq 0$):

$$
\begin{aligned}
0 &\leq \frac{1}{|\omega|}\sigma_{ij}^* M_{ijkl}\sigma_{kl}^* d\omega \\
&= \frac{1}{|\omega|}(\sigma_{ij} - \overline{\sigma}_{ij})M_{ijkl}(\sigma_{kl} - \overline{\sigma}_{kl})d\omega \\
&= \overline{\sigma}_{ij}(\frac{1}{|\omega|}\int_\omega (C_{ijkl})^{-1}d\omega - (\overline{C}_{ijkl})^{-1})\overline{\sigma}_{kl}
\end{aligned}
\qquad . \qquad (2.22)
$$

By using the Eq. (2.15), it can be rewritten as:

$$
\overline{\sigma}_{ij}(\overline{C}_{ijkl}^{Reuss-1} - (\overline{C}_{ijkl})^{-1})\overline{\sigma}_{kl} \geq 0. \qquad (2.23)
$$

It can be revised as:

$$
\alpha_{ij}\overline{C}_{ijkl}^{Reuss}\alpha_{kl} \leq \alpha_{ij}\overline{C}_{ijkl}\alpha_{kl} \ \forall \alpha_{ij}. \qquad (2.24)
$$

By combining Eq. (2.20) and Eq. (2.24), it becomes the Hill-Reuss-Voigt Bounds:

$$
\alpha_{ij}\overline{C}_{ijkl}^{Reuss}\alpha_{kl} \leq \alpha_{ij}\overline{C}_{ijkl}\alpha_{kl} \leq \alpha_{ij}\overline{C}_{ijkl}^{Voigt}\alpha_{kl}. \qquad (2.25)
$$

Self-consistent Method. Eshelby [57] proposed an analytical solution of ellipsoidal inclusion in a homogeneous infinite matrix. The inclusion and matrix are supposed to be merged seamlessly. A strain without constraint is assumed to exist, which is caused by the heterogeneity. Through a hypothetical test, this tensor is derived in the form of the Green's function. The Green's function is defined as the displacement at one point caused by force at another position. In a homogeneous infinite matrix, Eshelby tensor is constant for an ellipsoidal inclusion.

Inspired by this hypothetical test, Hill [80] and Budiansky [18] initiated original works for the self-consistent method. Within this method, both the matrix and inclusion/fibre is supposed to be transversely isotropic. The effective property can be derived through the Eshelby tensor.

Mori-Tanaka method It was developed by Mori and Tanaka [125]. The underlying assumption is the same as the self-consistent method. However, there is an additional assumption: If volume fraction of the inclusion equals 1, properties of the whole UC/RVE is assumed to be equal to the properties of the inclusion. A tensor is defined to relate the average strain in the inclusion and the one in the matrix. The effective property can be deduced by using this tensor.

Semi-analytical Method

Compared with analytical methods, differences at fine scale can be specified. Compared with fully computational methods, it is more efficient. Here is a brief review of three representative semi-analytical methods, including the Fourier series approach,

Transformation Field Analysis (TFA) and Generalised Method of Cells (GMC) and High Fidelity Generalised Method of Cells (HFGMC). To be mentioned, TFA, GMC and HFGMC fall into the category of reduced order method.

Fourier series approach. Fourier series approach is proposedby Nemat-Nasser and Taya [127] for the heterogeneous elastic material. The derivation of the effective properties of periodic composites in this method relies primarily on representations in Fourier space. Due to periodic assumptions, the Fourier expansion form automatically satisfies the continuity of the boundary condition. An integral equation can be derived based on the equilibrium equation. Then, this integral equation is transformed into a system of linear equations with unknown Fourier coefficients. Finally, the Eshelby tensor is introduced to express the effective properties. This approach is then employed for crack problems by Nemat-Nasser et al. [128].

TFA. TFA is proposed by Dvorak and Rao [49]. For each UC, a so-called localised operator is determined by replacing the continuous strain field with a piecewise constant field. A reduced set of constitutive relationships of heterogeneous materials can be derived. Therefore, only a small number of microscopic coefficients need to be calculated, and the number of degrees of freedom is significantly reduced. Michel and Suquet [120] expanded TFA to the plastic analysis. The strain field is not taken as a piecewise constant to avoid overestimating stiffness effective properties. TFA was successfully applied to nonlinear composites (see Fish et al. [67]), damage analysis (see Chaboche et al. [32]) and fatigue analysis (see Yu [64]).

GMC and HFGMC. GMC is developed by Aboudi [2]. RUCs are orthotopically arranged in three dimensions. The global structure is divided into RUCs, and a RUC can be divided into several subcells. The whole system is described by the global coordinate and local coordinate system. The global coordinate system is related to RUCs and a single RUC, and the local-coordinate system is about the subcells.

Each cell can also be divided into many subcells. Through volume average of stress and strain, the homogenised stress and strain can be derived for each subcell. By applying RUC's continuity conditions of displacements and tractions, each subcell gets a set of displacements. The set of displacements is then expanded by terms related to centre coordinates and local coordinates of subcells. Based on this form of expansion, a concentrated tensor $\mathscr{A}^{(subcell)}$ is introduced to connect the global strain $\overline{\epsilon}$ with the homogenised strain of each subcell $\overline{\epsilon}^{(subcell)}$:

$$\overline{\epsilon}_{ij}^{(subcell)} = \mathscr{A}_{ijkl}^{(subcell)}\overline{\epsilon}_{kl}. \tag{2.26}$$

Then the global constitutive law can be derived as follows:

$$\overline{\mathbf{C}}_{ijkl} = \frac{1}{V}\sum_{subcell=1}^{N_{subcell}}(\mathbf{C}_{ijmn}^{(subcell)}\mathscr{A}_{mnkl}^{(subcell)}V^{(subcell)}). \tag{2.27}$$

By employing a second-order displacement field, HFGMC was developed by Aboudi [4]. As a result, HFGMC retains an advantage for complicated fine scale situation. Under the

framework of HFGMC, Pineda et al. [138] conducted a failure study and a sensitivity analysis on the effect of the size of the RUC on the stiffness and strength of the RUC. However, due to the lack of consideration of different load conditions and the limitation on sample size limitations, no rigorous statistical analysis was performed.

Numerical Methods

As the development of the computer, the numerical methods for RVE/UC problem are more accessible to solve. Therefore, numerical methods are widely developed and used, which are often referred to as computational upscaling methods or computationally homogenisations. Accordingly, various multi-scale computational methods were designed to ensure computational efficiency and accuracy.

Computationally homogenisation/FE^2 method Computational homogenisation is a more general concept than FE^2. The numerical methods applied for discretisation are not limited to FEM, and methods such as finite difference methods, finite volume methods, and spectral element methods can also be employed. The initial theoretical work was proposed by Sánchez-Palencia [148], Huet [93], and Zohdi et al. [171]. The governing equations are obtained from the virtual work principle. The unknown macroscopic material properties are derived from the microscopic Representative Volume Element (RVE). The flow of information follows two ways: Homogenisation (micro to macro) and Localisation (macro to micro). Homogenisation is obtained by volume (3D problems) or area (2D problems) average. Localisation is done by retrieving the average displacement deformation gradient in an RVE from the structural analysis. Homogenisation and localisation both realised by addressing microscopic and macroscopic boundary value problems (BVP) and nested with each other.

Feyel and Chaboche [60] applied the FEM for solving both macroscopic and microscopic BVPs and denoted this method as FE^2. Thanks to the development of FEM, FE^2 achieved a dominant position in the computational homogenisation methods, which evolved to represent the category of computational homogenisations.

Figure 2.8: Decomposition of the microscopic displacement **u**, which is reproduced based on the work of Tikarrouchine et al. [158]

As shown in Fig 2.8, the microscopic displacement **u** can be decomposed into two

parts. One part related to slowly varying macroscopic deformation $\overline{\epsilon}\mathbf{X}$, where $\overline{\epsilon}$ is the macroscopic infinitesimal/Cauchy strain. The other part is a disturbance field caused by heterogeneity $\mathbf{w}_{,\mathbf{X}}(\mathbf{X})$ as:

$$\mathbf{u} = \overline{\epsilon} \cdot \mathbf{X} + \mathbf{w}_{,\mathbf{X}}(\mathbf{X}). \tag{2.28}$$

For a two-dimensional problem, the macroscopic Cauchy strain is derived by area averaging as:

$$\overline{\epsilon} = \frac{1}{|\omega|} \int_{\omega} \epsilon \, d\omega. \tag{2.29}$$

where $|\omega|$ is the volume of RVE. Besides, the macroscopic Cauchy stress is also obtained by area average as:

$$\overline{\sigma} = \frac{1}{|\omega|} \int_{\omega} \sigma \, d\omega. \tag{2.30}$$

The Hill-Mandel condition is eventually be derived as follows

$$\overline{\sigma} : \overline{\epsilon} = \frac{1}{|\omega|} \int_{\omega} \sigma : \epsilon \, d\omega. \tag{2.31}$$

For addressing a large deformation problem, instead of using σ and ϵ, Miehe et al. [122] employed the PK1 stress $\mathbf{P}$ and Green-Lagrangian strain $\mathbf{E}$ for derivation. A framework for addressing large deformation problems is built up as shown in Fig. 2.9.
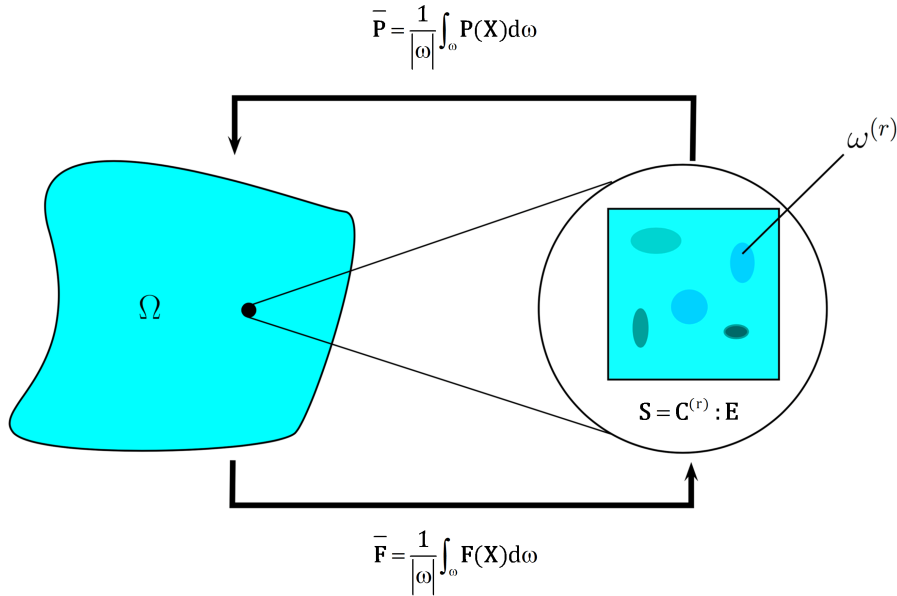
Figure 2.9: Schema of FE^2 for addressing large deformation problems.

Compared to the Green-Lagrangian strain $\mathbf{E}$, the Cauchy strain ϵ is a linearised fraction by neglecting the second order term as:

$$\mathbf{E} = \frac{1}{2}(\mathbf{F}^T \cdot \mathbf{F} - \mathbf{I}) = \frac{1}{2}(\nabla\mathbf{u} + \nabla\mathbf{u}^T + \nabla\mathbf{u} \cdot \nabla\mathbf{u}^T) \tag{2.32}$$

$$\epsilon = \frac{1}{2}(\mathbf{F}^T + \mathbf{F} - \mathbf{I}) = \frac{1}{2}(\nabla\mathbf{u} + \nabla\mathbf{u}^T). \tag{2.33}$$

where $\mathbf{F}$ is the material deformation gradient. In this thesis, it is abbreviated as deformation gradient. As shown in Fig. 2.10, deformation gradient $\mathbf{F}$ represents the relationship between the variations in reference/undeformed and current/deformed configuration:

$$\mathbf{F}(\mathbf{x}, \mathbf{X}) = \nabla\mathbf{u} + \mathbf{I}. \tag{2.34}$$
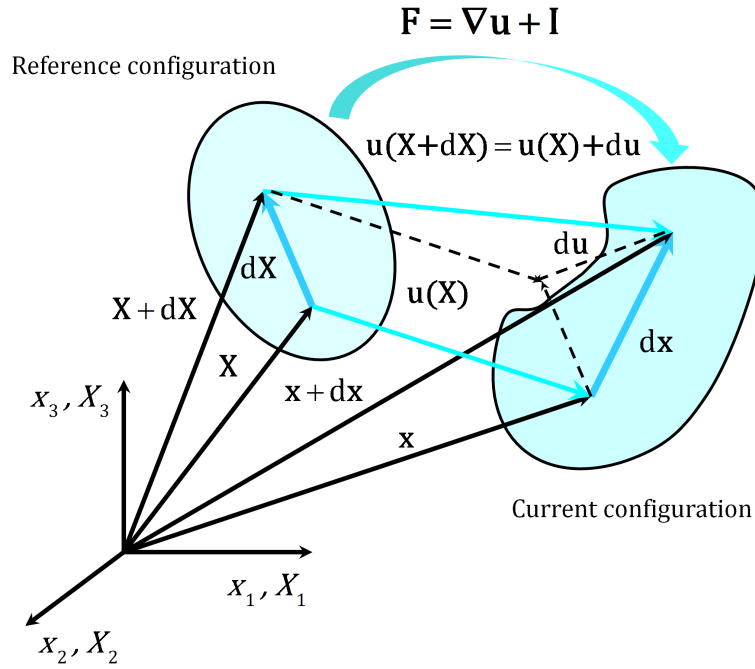
Figure 2.10: Schema of deformation gradient $\mathbf{F}$

Where $\mathbf{I}$ is the identity tensor. According to the large deformation framework, the expansion of the microscopic coordinates $\mathbf{x}$ in the current configuration is decomposed as:

$$\mathbf{x} = \overline{\mathbf{F}} \cdot \mathbf{X} + \mathbf{w}. \tag{2.35}$$

where $\overline{\mathbf{F}} \cdot \mathbf{X}$ represents the part related to slowly varying macroscopic deformation, and $\mathbf{w}$ stands for a disturbance field part caused by heterogeneity. The macroscopic

deformation gradient is derived by area averaging as:

$$\overline{\mathbf{F}} = \frac{1}{|\omega|} \int_\omega \mathbf{F} d\omega. \tag{2.36}$$

where $|\omega|$ is the volume of RVE. Besides, the macroscopic PK1 stress is also obtained by area average as:

$$\overline{\mathbf{P}} = \frac{1}{|\omega|} \int_\omega \mathbf{P} d\omega, \tag{2.37}$$

where

$$\mathbf{P} = \mathbf{F} \cdot \mathbf{S} = \mathscr{H} : (\mathbf{F} - \mathbf{I}). \tag{2.38}$$

A four-order tensor $\mathscr{H}$ is defined as (see Nezamabadi [5]):

$$\mathscr{H} = (\mathbf{F} \,\overline{\underline{\otimes}}\, \mathbf{I}) : \mathbf{C}^{(r)} : \mathbb{B} + \mathbf{I} \,\overline{\otimes}\, \mathbf{S}. \tag{2.39}$$

where $\overline{\underline{\otimes}}$ is the Kronecker product as:

$$(\mathbf{a} \,\overline{\underline{\otimes}}\, \mathbf{b})_{ijkl} = \frac{1}{2}(a_{ik}b_{jl} + a_{il}b_{jk}), \tag{2.40}$$

and $\overline{\otimes}$ means

$$(\mathbf{a} \,\overline{\otimes}\, \mathbf{b})_{ijkl} = a_{ik}b_{jl}. \tag{2.41}$$

$\mathbb{B}$ and $\mathbf{S}$ can be expressed as follows:

$$\mathbb{B} = \frac{1}{2}(\mathbf{F}^T \,\underline{\otimes}\, \mathbf{I} + \mathbf{I} \,\overline{\otimes}\, \mathbf{F}) \tag{2.42}$$

$$\mathbf{S} = \mathbf{C}^{(r)} : \mathbf{E}. \tag{2.43}$$

where $\underline{\otimes}$ means

$$(\mathbf{a} \underline{\otimes} \mathbf{b})_{ijkl} = a_{il}b_{jk}. \tag{2.44}$$

The corresponding Hill-Mandel condition is derived as follows:

$$\delta\overline{\mathbf{F}}^T : \overline{\mathbf{P}} = \delta\overline{\mathbf{E}}^T : \overline{\mathbf{S}} = \int_{\omega_0} \delta\mathbf{F}^T : \mathbf{P} d\omega = \int_\omega \delta\mathbf{E}^T : \mathbf{S} d\omega. \tag{2.45}$$

Several analyses were carried out under the framework of the first order FE^2. Kanit et al. [100] studied the RVE size effects on elastic, thermal, and geometrical properties. A parallel algorithm was introduced by Matsui et al. [118] to achieve computational efficiency. Tchalla et al. [153] implemented the FE^2 method in the commercial software ABAQUS by applying the parallel computation. A simulation of plastic behaviour of composite materials was presented by Azoti et al. [7]. Later, El Hachemi et al. [55] extended computational homogenisation to complex viscoelastic composite materials.

For a better prediction of the microscopic response with large macroscopic deformation gradient, the second-order FE^2 was built and developed by Geers et al. [68] and Kouznetsova et al. [106]. The variation of microscopic position $\Delta\mathbf{x}$ in the current system is separated into three parts as follows:

$$\Delta\mathbf{x} = \overline{\mathbf{F}}\Delta X + \frac{1}{2}\Delta\mathbf{X}^T\overline{\mathbf{G}}\Delta X + \Delta\mathbf{w}. \tag{2.46}$$

where a third-order tensor $\overline{\mathbf{G}}$ is introduced as:

$$\overline{\mathbf{G}} = \nabla\overline{\mathbf{F}}. \tag{2.47}$$

For heterogeneous materials, to deal with the buckling instability that may occur at macroscopic and mesoscale, Nezamabadi et al. [130] developed a method called Multiscale-ANM by coupling FE^2 and Asymptotic Numerical Method (see Subsection 2.3.2) This method has covered several topics, including the buckling analysis of elastoplastic (see Nezamabadi et al. [131]), a vibration analysis (see Attipou et al. [5]) and a failure analysis (see Nezamabadi et al. [132]) of fibre-reinforced material.

Voronoi Cell FEM (VCFEM) The parenchyma in plants can be thought of as consisting of randomly distributed cells. Mattea et al. [119] generated their microstructure hinged on a two-dimensional formula of the Voronoi tessellation algorithm. The basic idea of the Voronoi diagram is as follows: First, random points are generated in the domain, and a line connects two adjacent points. These lines connecting adjacent points can be regarded as the nerves of the cells in the Voronoi diagram and constitute the Delaunay triangulation as shown in 2.11. Then, cell walls perpendicular to these lines are introduced to generate the cell structure. This morphological-based cell generation process mimics natural evolution. Based on this theory, Ghosh and Liu [72] proposed VCFEM modelling for microstructures with heterogeneity. VCFEM treats each Voronoi unit with embedded inclusions as a single element. There is no discretisation in the framework of VCFEM. VCFEM is further extended to apply to a wide variety of micromechanical problems including elasto-plastic problems (Ghosh et al. [70]), thermal-mechanical problems (see Ghosh and Liu [71]), and damage problems (see Ghosh and Raghavan [73]).

Voronoi diagram   Delaunay Triangulation
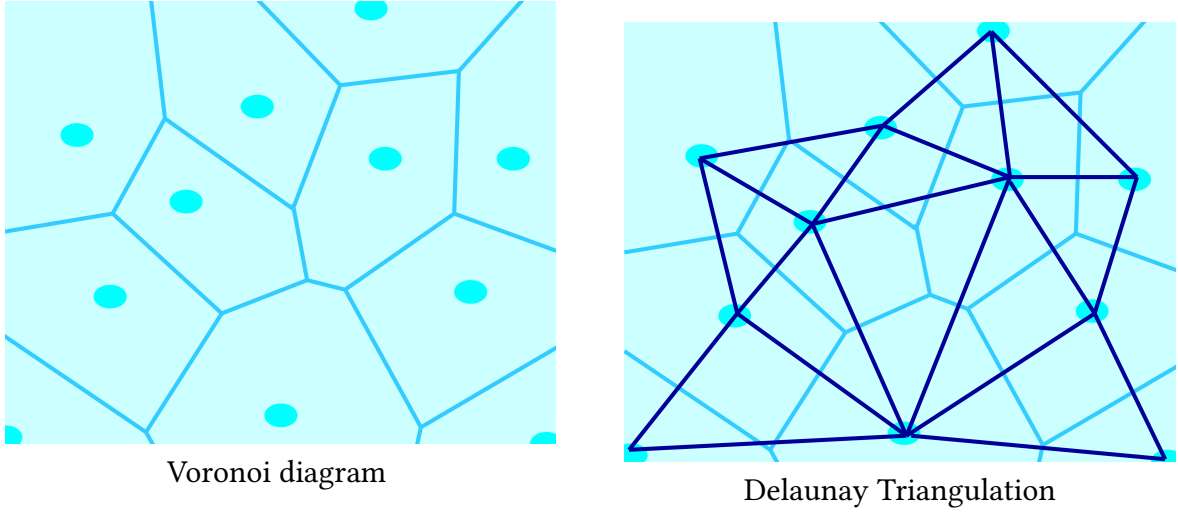
Figure 2.11: Schema of Voronoi diagram and Delaunay Triangulation.

2.2.2 Building the Link for the Multi-scale Problem

After solving the problem in UC/RVE, another major topic is to link different scales. Methods to link different scales can be separated into two categories: Fine scale oriented and coarse scale oriented methods.

Fine Scale Oriented Methods

The following three methods are regarded as mainstream fine scale oriented methods. The link between two scales is by getting Effective Properties from Finer Scale.
Asymptotic method. Asymptotic Method/Homogenisation is proposed by Bensoussan et al. [13]. Under the framework of this method, problems are limited to cases of periodic oscillations. The salient point is to asymptotically expand the displacements at two scales $(\mathbf{X}, \overline{\mathbf{X}})$:

$$u(\overline{\mathbf{X}}, \mathbf{X}) = u^0(\overline{\mathbf{X}}, \mathbf{X}) + \zeta u^1(\overline{\mathbf{X}}, \mathbf{X}) + O(\zeta^2). \tag{2.48}$$

where u is the fine-scale displacement, whereas ζ $(0 < \zeta \ll 1)$ is the characterised size of the fine scale. Coarse scale's strain is supposed to be computed from fine-scale strain by domain averaging:

$$\overline{\epsilon}_{ij} = \frac{1}{|\omega|} \int_\omega \epsilon_{ij}(\overline{\mathbf{X}}, \mathbf{X}) d\omega. \tag{2.49}$$

where all the terms of coarse scale are marked with overline.
The subscript "ζ" represents the real field. Likewise, the coarse scale stress is also derived in the same way:

$$\overline{\sigma}_{ij} = \frac{1}{|\omega|} \int_{\omega} \sigma_{ij}(\overline{\mathbf{X}}, \mathbf{X}) d\omega. \tag{2.50}$$

The variation of constitutive tensor and stress can be separated into two groups: slow variation and fast variation. Slow variation is affected by the coarse scale ($\overline{\mathbf{X}}$). Fast variation depends on the fine scale ($\mathbf{X}$). Through expanding the terms in balance equation, different terms can be grouped by the different order of the characterised term ζ.

The elastic strain influence function $\mathscr{E}_{kl}^{mn}(\mathbf{X})$ is introduced to connect the strain at fine and coarse scale following a manner as:

$$\overline{C}_{ijmn} = \frac{1}{|\omega|} \int_{\omega} C_{ijkl} \mathscr{E}_{kl}^{mn}(\mathbf{X}) d\omega. \tag{2.51}$$

Therefore, the unknown coarse scale constitutive relation is constructed. Several different specific topics are considered, and this theory is more and more generic. Lefik and Schrefler [112] improved this method with some corrective/additional terms (thermal expansion coefficient vector) for a thermal-mechanical analysis. Marcellini [116] extended this method for geometrically nonlinear problems. This method was well summarised in Boso et al. [16] and Fish et al. [67].

Hill-Mandel Condition. Hill Mandel Condition was formulated by Hill [81] and Mandel [115]. It is also called the average energy relation or Hill-Mandel principle of macro-homogeneity. For static problems, it determines the energy consistency between the fine and coarse scales (which determines the compatibility of energy rates, taking into account time factors). A domain holds:

$$\frac{1}{|\omega|} \int_{\omega} \sigma_{ij} \epsilon_{ij} d\omega = \overline{\sigma}_{ij} \overline{\epsilon}_{ij}. \tag{2.52}$$

For illustrating the constitutive relationship at the coarse scale, the concept of effective property $\overline{C}_{ijkl}$ is proposed:

$$\overline{\sigma}_{ij} = \overline{C}_{ijkl} \overline{\epsilon}_{kl}. \tag{2.53}$$

Meanwhile, it is also an essential assumption in the FE^2 method, which will be discussed later.

Heterogeneous Multi-scale Method (HMM): Finite element HMM. Heterogeneous Multiscale Method was proposed by E and Engquist [51]. It belongs to the upscaling methods. The constitutive tensor $\overline{C}_{ijkl}$ from the coarse scale is missing information. As the framework of HMM is entirely mathematical, a general form is presented here within the framework FEM (see Abdulle and Engquist [1]). Gauss integration is applied for computing the coarse scale stiffness. Therefore, the problem of the whole domain transforms into a series of issues related to Gauss quadrature points. Define the position of the Gauss quadrature point as $\hat{\mathbf{X}}_I$:

$$\overline{\sigma}_{ij}(\hat{\mathbf{X}}_I) = \overline{C}_{ijkl)}(\hat{\mathbf{X}}_I) \overline{\epsilon}_{kl}(\hat{\mathbf{X}}_I) = \frac{1}{|\omega|} (\int_{\omega} C_{ijkl}(\hat{\mathbf{X}}_I, X) \epsilon_{kl}(\hat{\mathbf{X}}_I, X) d\omega) \ . \tag{2.54}$$

The coarse scale strain is considered to be obtained by area average:

$$\bar{\epsilon}_{kl}(\hat{\mathbf{X}}_I) = \frac{1}{|\omega|} \int_\omega \epsilon_{kl}(\hat{\mathbf{X}}_I, X) d\omega. \tag{2.55}$$

in which $\hat{\mathbf{X}}_I$ is the fine-scale coordinate of quadrature point. 6 sets of unit strain e_{kl} are employed for coarse scale strain as:

$$\bar{\epsilon}_{kl}(\hat{\mathbf{X}}_I) = e_{kl}. \tag{2.56}$$

Then, Eq. (2.54) will be reformed as:

$$\overline{C}_{ijkl}(\hat{\mathbf{X}}_I) = \frac{1}{|\omega|} \int_\omega C_{ijkl}(\hat{\mathbf{X}}_I, \mathbf{X}) \epsilon_{kl}(\hat{\mathbf{X}}_I, \mathbf{X}) d\omega. \tag{2.57}$$

Thus, the macroscopic constitutive tensor $\overline{C}_{ijkl}(\hat{\mathbf{X}}_I)$ is obtained. After getting the effective property from the fine scale, the next step is to solve the coarse scale problem. Galerkin method is applied and the elemental stiffness matrix is obtained with the Gauss integration. Ren and E [143] has proposed an investigation of fluids with both temporal and spatial fields considered By coupling the FEM and HMM, A method called finite element HMM was addressed by Abdulle and Engquist [1].

Coarse Scale Oriented Method

Babuska [8] proposed this concept: Coarse-scale kinematical relationship could be enriched to reflect the fine scale details. Inspired by this idea, several generalised FEMs are developed, including Multi-scale FEM (MsFEM), Variational Multi-scale Method (VMS), Multi-scale Enrichment Based on the Partition of Unity (MEPU), and Discontinuous Enrichment Method (DEM). These generalised FEMs share the same process to obtain the coarse scale stiffness matrix. Firstly, enhanced strain-displacement matrix $\overline{\mathscr{B}}_{kli}$ is defined as follows:

$$\overline{\mathscr{B}}_{kli}(\overline{\mathbf{X}}, \mathbf{X}) = \overline{N}_{(si, \overline{X}_t)}(\overline{\mathbf{X}}) \mathscr{E}_{kl}^{st}(\mathbf{X}). \tag{2.58}$$

where $\mathscr{E}_{kl}^{st}$ is the elastic strain influence function as mentioned for Asymptotic Method. Then, the coarse scale stiffness can be derived as:

$$\overline{K}_{ij} = \int_\Omega \frac{1}{|\omega|} \int_\omega \overline{\mathscr{B}}_{kli} C_{klgh}(\mathbf{X}) \overline{\mathscr{B}}_{kli} d\omega d\Omega. \tag{2.59}$$

However, between these methods, integrations at the coarse scale, enrichment of the kinematic equations, and constraints at the fine scale are different. To these differences, the subsequent paragraphs give more details for these methods.

MsFEM. For heterogeneous material's modelling, Hou and Wu [84] proposed MsFEM

based on Babuska's method. Instead of building the enhanced strain-displacement matrix $\overline{\mathscr{B}}_{kli}$, the coarse-scale enriched shape function $\overline{N}_{gi}$ is obtained by addressing the following fine-scale BVPs:

$$
\begin{aligned}
(C_{klgh} N^{(e)}_{gi,h})_{,l}(\mathbf{X}) &= 0 \text{ in } \omega^{(e)} \\
N^{(e)}_{gi}(\mathbf{X}) &= \overline{N}^{(e)}_{gi}(\overline{\mathbf{X}}) \text{ on } \partial\omega^{(e)}
\end{aligned}
\tag{2.60}
$$

The boundary conditions shown in Eq. (2.60) are proposed in the initial works. It is assumed that the enhanced coarse scale shape function corresponds to a single element in the coarse scale. Subsequently, the oversampling technique is introduced to establish a relationship between an enhanced coarse scale shape function and their corresponding coarse-scale elements. This oversampling technique can improve the results as a consequence of the ability to collect more fine-scale information. Therefore, two corresponding boundary conditions are introduced including oversampling oscillating boundary condition and oversampling periodic boundary condition (see Efendiev and Hou [54]). Hou et al. [85] found that the supersample technique can effectively reduce the boundary effects under oscillating boundary conditions. Moreover, the convergence speed is faster, but it does not affect the linear boundary. Chu et al. [34] verified this result and discussed various supersample techniques.

VMS. VMS was proposed by Hughes et al. [94], which is also called Hughes Variational Multi-scale method. The idea of VMS is to use variable-consistent discretisation at the coarse scale, and only maintain the stability at the fine scale. The fine and coarse scale are coupled, where stability at the fine scale effects indirectly at the coarse scale.

Under the framework of this method, different scales are considered with only one axis system $\mathbf{X}$, instead of $\overline{\mathbf{X}}$ and $\mathbf{X}$. In other words, the unknowns of coarse and fine scales are coupled. Both the displacements fields and the corresponding weights are decomposed into two parts. One part is about the coarse scale, and the other part is related to the fine scale. Consequently, based on these parts of shape function and weights on different scales, the virtual work weak form can be discretised. An additional assumption is taken here to simplify the problem. The displacements and weights at fine scale will vanish at the boundary line at each element. However, this assumption causes troubles when dealing with crack problems. This method was furthermore developed with a combination of FEM by Gravemeier [77].

MEPU. Based on the basic idea of enriching the coarse scale's balance equation, Fish and Yuan [65] proposed a method called MEPU. This method modified the VMS, and apply the Galerkin Method to discretise the system. It was extended for nonlinear problems by Fish and Yuan [66].

DEM. DEM is another generalised FEM proposed by Farhat [58]. This enrichment basis function is continuous at the element interface. Lagrangian multiplier degrees of freedom is introduced to ensure the weak continuity of solutions at element interfaces. Besides, enrichment functions do not need to follow the high-order orthogonal rules to evaluate the stiffness matrix. The two-dimensional and three-dimensional problems

were benchmarked by Farhat et al. [59] and Tezaur and Farhat [155], respectively.

2.2.3 Summary of Software based on Multi-scale Methods

In 2015, Rithchey et al. [146] published a thorough review in the composites design and manufacture hub, and this work was further refined by Sertse et al. [151]. The strengths and weaknesses of 5 candidate software products are compared. Based on these works, several representative software products are briefly described below.

1. The NASA Glenn Research Centre's MAC/GMC is based on two semi-analytical models of GMC and HFGMC (refer to Subsection 2.2.1).

2. DIGIMAT is developed by e-Xstream engineering. Two kinds of multi-scale methods are applied: 1. Mori-Tanaka method (refer to Subsection 2.2.1); 2. FE^2 method (see [160] and refer to Subsection 2.2.1).

3. Multi-scale Design Systems is a family of products developed by Prof. Jacob Fish [64], and it was later acquired by Altair. These products were programmed in Python based on the method MEPU (refer to Subsection 2.2.2). The family of products include a set of plug-ins for commercial FEM software (ABAQUS, ANSYS, LS-DYNA) for implementing functionalities on multi-scale modelling.

4. SwiftComp is a code developed by Prof. Wenbin Yu based on structural mechanics and GMC (refer to Subsection 2.2.1). A new concept Structure Genome is introduced as an approach to link the microscopic mechanics and structural mechanics. The effective properties can be applied for building beam, plate and other structural models (see Yu [167]). Its graphical user interface is based on Gmsh, and the structural solver is based on Calculix. The nonlinear solver of Calculix is based on the Newton-Raphson method (see Dhondt [46] and refer to Subsection 2.3.1).

5. The Virtual Performance Solution is a multi-scale modelling software released by the ESI Group based on Computational homogenisation/FE^2 (refer to Subsection 2.2.1).

2.3 Review of the Nonlinear Solver

2.3.1 Incremental/Iterative/Path-corrector Methods

In structural calculations, incremental/iterative methods are used to calculate non-linear problems due to large geometric variations or material behaviour. Please note that this section only focuses on geometric nonlinearity, which means the structure undergoes massive displacement and large rotation during the load action. At this time, the geometric equation is no longer linear, and the equilibrium equation must be established in the deformed state. Suppose an object is under static load. If it is assumed that there is an infinitesimal virtual displacement inside the object, then from the actual configuration, the following variation equation is established:

$$\delta \mathscr{L}_{int} = \delta \mathscr{L}_{ext}. \tag{2.61}$$

$\delta \mathscr{L}_{int}$ is a virtual variation of internal energy, and $\delta \mathscr{L}_{ext}$ is a virtual variation of external work. The variational equation Eq (2.61) is reduced to a nonlinear algebraic equation with the following equivalent form:

$$\boldsymbol{\varphi}(\mathbf{q}, \mathscr{P}) = \mathscr{P}^{int}(\mathbf{q}) - \mathscr{P}^{ext} = \mathbf{K}(\mathbf{q})\mathbf{q} - \lambda \mathbf{f} = 0. \tag{2.62}$$

where $\boldsymbol{\varphi}$ is a nodal force composed of internal and external forces, $\mathscr{P}^{int}(\mathbf{q})$ is the internal force from the internal stress, $\mathscr{P}^{ext}$ is the external force vector. $\mathbf{q}$ is the node displacement vector, $\mathbf{K}$ being the stiffness matrix, λ being the load factor, and $\mathbf{f}$ being a constant loading force. The aim is to search the solution path from the initial m state to the $m + 1$ state (unknown) in its neighbourhood. The specific decomposed format follows Batoz and Dhatt [12] and Carrera [19]:

$$\mathscr{R}(\mathbf{q}, \lambda) = \boldsymbol{\varphi}_{,\mathbf{q}} \Delta \mathbf{q} + \boldsymbol{\varphi}_{,\mathscr{P}^{ext}} \Delta \mathscr{P}^{ext}. \tag{2.63}$$

The symbol Δ represents a global variation in one step. $\Delta \mathscr{P}^{ext}$, $\boldsymbol{\varphi}_{,\mathbf{q}}$ and $\boldsymbol{\varphi}_{,\mathscr{P}^{ext}}$ can be expressed as follows:

$$\begin{aligned} \Delta \mathscr{P}^{ext} &= \Delta \lambda \mathbf{f} \\ \boldsymbol{\varphi}_{,\mathbf{q}} &= \mathbf{K}(\mathbf{q}) \\ \boldsymbol{\varphi}_{,\mathscr{P}^{ext}} &= -\mathbf{I}, \end{aligned} \tag{2.64}$$

where $\mathbf{I}$ is the identity matrix, $\Delta \mathbf{q}$ being the incremental node displacement vector, and $\Delta \lambda$ being the incremental load vector. The loading factor is the residual of the nodal force. Then, Eq. (2.63) can be rewritten as follows:

$$\mathscr{R}(\mathbf{q}, \lambda) = \mathbf{K}\Delta \mathbf{q} - \Delta \lambda \mathbf{f}. \tag{2.65}$$

Where $\mathscr{R}(\mathbf{q}, \lambda)$ is the residual, and it is also called the unbalanced load, which is the difference between the required load and the calculated load. If the value of the imbalance is less than the specified tolerance, the solution is converged; if not, it must be the next

iteration, estimated from the results of the previous iteration. Within the incremental method, the load factor λ is divided into several steps. The corresponding displacement vector $\mathbf{q}$ is also divided into steps.

Newton-Raphson Method (NRM) NRM is one of the most basic algorithms for solving nonlinear equations. Based on the incremental form of Newton's method, the displacement vector $\mathbf{q}_m$ corresponding to the load factor λ_m of the mth step is known, and then the load factor is increased to $\lambda_{m+1} = \lambda_m + \Delta\lambda_m$ to solve the corresponding displacement $\mathbf{q}_{m+1}$.

It is assumed that the corresponding tangent stiffness matrix at mth step is $\mathbf{K}_m$. The $(n + 1)$th iteration of the $(m + 1)$th step can be expressed as:

$$\mathscr{R}(\Delta\mathbf{q}_{m+1}^n) - \mathbf{K}_{m+1}^n \delta\mathbf{q}_{m+1}^n + \Delta\lambda_{m+1}\mathbf{f} = 0, \tag{2.66}$$

where $\mathbf{K}_{m+1}^n$ is the nth modified value of $\mathbf{K}_{m+1}$, and the nth correction amount of $\Delta\mathbf{q}_{m+1}$ is $\Delta\mathbf{q}_{m+1}^n$, which is:

$$\delta\mathbf{q}_{m+1}^n = (\mathbf{K}_{m+1}^n)^{-1}(\mathscr{R}(\mathbf{q}_{m+1}^n) - \Delta\lambda_{m+1}\mathbf{f}). \tag{2.67}$$

The $(n + 1)$th update of $\mathbf{q}_{m+1}$ is:

$$\Delta\mathbf{q}_{m+1}^{n+1} = \Delta\mathbf{q}_{m+1}^n + \delta\mathbf{q}_{m+1}^n. \tag{2.68}$$

As shown in Eq. (2.66), each iteration needs to be reformed and decomposed into a tangent stiffness matrix $\mathbf{K}_{m+1}^n$ to work. The computational cost is quite significant, therefore, the modified NRM method has been proposed.

Modified Newton-Raphson Method (MNRM) For all iterations of the mth step, the tangent stiffness matrix remains the same, therefore, at each step, only a tangential stiffness matrix is assembled.

$$\mathbf{K}_{m+1} = \mathbf{K}_{m+1}^1 \tag{2.69}$$

The displacement increment of the mth step can be expressed as:

$$\Delta\mathbf{q}_{m+1}^{n+1} = (\mathbf{K}_{m+1})^{-1}(\mathscr{R}(\mathbf{q}_{m+1}^n) - \Delta\lambda_{m+1}^n\mathbf{f}). \tag{2.70}$$

A schematic diagram of the NRM and MNRM is shown in Fig. 2.12

(a) Newton-Raphson Method   (b) Modified Newton-Raphson Method
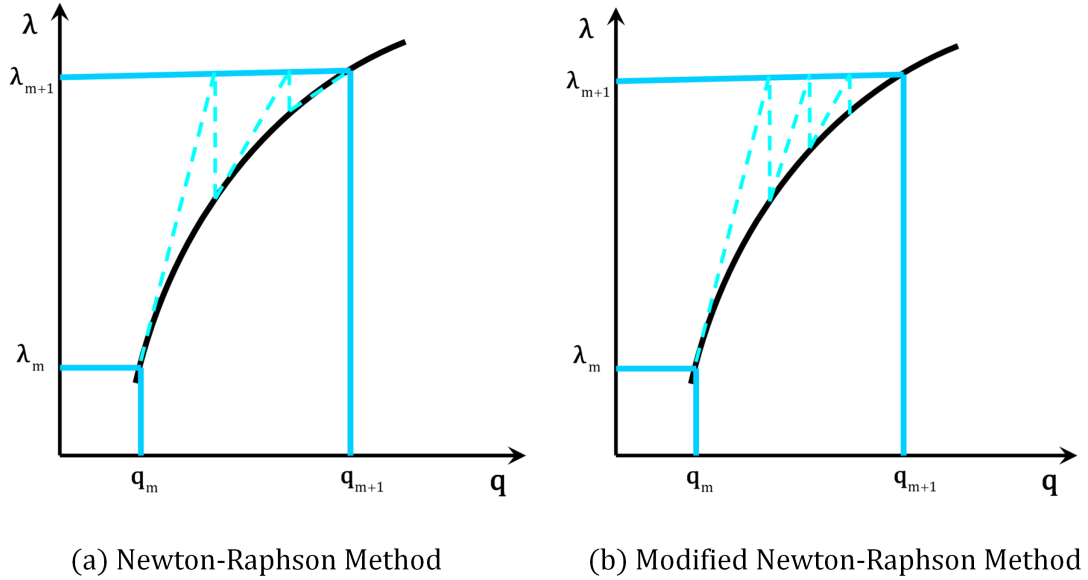
Figure 2.12: Schema of the NRM and Modified MNRM.

NRM and MRNM have been widely employed for analysing nonlinear problems. However, for the buckling problems, the NRM and the MNRM performs poorly because a sufficiently small step size must be specified to confirm that the calculation converges, and that leads to a tremendous calculation amount. If the step size is improperly defined, the solution may not converge.

Arc-length and other quadratic control methods

Riks-Wempner Method (RWM) NRM method and MNRM method are not sufficient for the problem with strong nonlinearity. As a consequence, several pioneering works for effectively passing the limit point were carried out by Phillips and Zienkiewicz [137], Bergan and Holand [15], Batoz and Dhatt [12]. Among a variety of methods, RWM (see Riks [145] and Wempner [164]) is the most effective solution for passing the limit point. For calculating the geometric nonlinear equilibrium path, a mixed load-displacement constraint equation is introduced by the vector $\mathbf{t} = \mathbf{q} + \lambda \mathbf{f}$. It represents the sum of all unknown vectors as:

$$(\Delta \lambda_m \psi)^2 \mathbf{f}^T \mathbf{f} + (\Delta \mathbf{q}_m)^T (\Delta \mathbf{q}_m) - \Delta \mathbf{t}^T \Delta \mathbf{t} = 0. \tag{2.71}$$

The above equation is called Riks-Wempner Arc Length Constraint equation. ψ is defined as the user-defined load scaling parameter. This constraint is a hyperspherical curve. In the case of $\psi = 1$ (as shown in Fig 2.13),
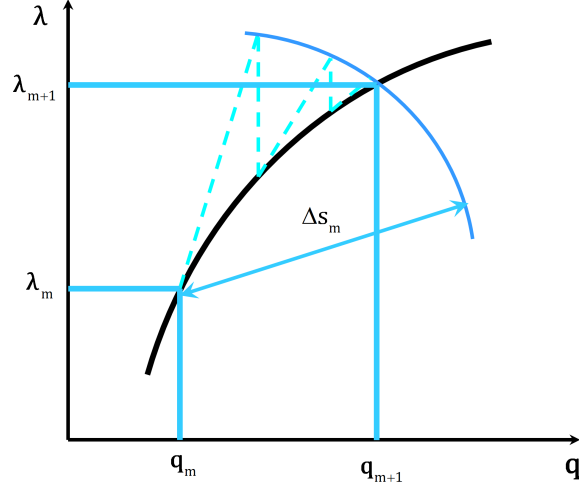
Figure 2.13: Schema of the Riks-Wempner Arc Length Method with $\psi = 1$.

Arc length Δs_m is defined as the distance between two step along the equilibrium path. It is expressed as follows:

$$\Delta s_m = |\Delta \mathbf{t}| = \sqrt{(\Delta \lambda_m)^2 \mathbf{f}^T \mathbf{f} + (\Delta \mathbf{q}_m)^T (\Delta \mathbf{q}_m)}. \tag{2.72}$$

The nth modification of increment in the $m + 1$ step is expressed as:

$$\begin{aligned}
\Delta \mathbf{t}_{m+1}^n &= \Delta \mathbf{t}_m^n + \delta \mathbf{t}_m^n \\
&= \Delta \mathbf{t}_{m+1}^n (\Delta \mathbf{q}_{m+1}^n, \Delta \lambda_{m+1}^n F) \\
&= \Delta \mathbf{t}_{m+1}^n (\Delta \mathbf{q}_m^n + \delta \mathbf{q}_m^n, \Delta \lambda_m^n + \delta \lambda_m^n \mathbf{f})
\end{aligned} \tag{2.73}$$

and δ representing the local variation of the nth iteration. Based on the orthogonality between the vector $\Delta \mathbf{t}_1 = \Delta \mathbf{q}_1 + \Delta \lambda_1 \mathbf{f}$ and $\delta \mathbf{t}_m^n = \delta \mathbf{q}_m^n + \delta \lambda_m^n \mathbf{f}$, the following governing equations can be derived as:

$$\mathscr{R}(\delta \mathbf{q}_{m+1}^n) = \mathbf{K}_{m+1} \delta \mathbf{q}_{m+1}^n - \delta \lambda_{m+1}^n \mathbf{f} \tag{2.74}$$

$$\Delta \mathbf{t}_{m+1}^1{}^T \delta \mathbf{t}_{m+1}^n = 0. \tag{2.75}$$

To be noticed, the value of $\Delta \mathbf{t}_{m+1}^n$ should be small enough to follow the strong nonlinear path.

Riks-Wempner-Ramm method (RWRM) Ramm [140] proposed an approach for improving RWM by updating t_{m+1}^{n-1} for the nth iteration at the $m + 1$ step based on the following control equations:

$$\mathcal{R}(\delta\mathbf{q}_{m+1}^n) = \mathbf{K}_{m+1}\delta\mathbf{q}_{m+1}^n - \delta\lambda_{m+1}^n\mathbf{f} \tag{2.76}$$

$$\Delta\mathbf{t}_{m+1}^{n-1}{}^T\delta\mathbf{t}_{m+1}^n = 0. \tag{2.77}$$

Ramm also studied the scaling parameters, found that the change in load does not affect the convergence significantly . In the case of $\psi = 0$, this method falls into the category of cylindrical arc length methods. The length of the displacement increment is supposed to be equal to the arc length for the first iteration of the first step:

$$\Delta\mathbf{q}_1^{1T}\Delta\mathbf{q}_1^1 = \Delta s_1^{1^2}. \tag{2.78}$$

Arc-length-Crisfield Method (ALCM) Not only the displacement increment of first iteration $\Delta\mathbf{q}_1^1$ equals to the arc length, Crisfied [38] successfully promoted RWRM and formed ALCM. It is supposed that the displacement increment equals the arc length of each iteration equals the corresponding arc length. Consequently, the control equations can be written as:

$$\mathcal{R}(\delta\mathbf{q}_{m+1}^n) = \mathbf{K}_{m+1}\delta\mathbf{q}_{m+1}^n - \delta\lambda_{m+1}^n\mathbf{f} \tag{2.79}$$

$$(\Delta\mathbf{q}_{m+1}^n)^T(\Delta\mathbf{q}_{m+1}^n) = \Delta s_{m+1}^2. \tag{2.80}$$

Eq. (2.80) is usually the additional equation for linear (RWM, RWRM) or quadratic (ALCM), which is different with the form shown in Eq. (2.71). It is because all load-related items are ignored, including all terms related to $\mathbf{f}$ ($\psi = 0$). This simplified form was recommended by Crisfield [37] due to the following two reasons. First, it is for avoiding ill-conditioned matrix near the limit points (see Crisfield [37]). Secondly, it is because the scaling parameters ψ affects the results slightly. The latter reason was validated by Ramm [140] and Crisfield [38]. In this case, the spherical ALCM ($\psi \neq 0$) is reduced to a so-called cylindrical ALCM ($\psi = 0$). Following the theory of cylindrical ALCM, a quadratic constraint equation is introduced for resolving ($\delta\lambda_{m+1}^n$). However, for a quadratic equation, there are two roots $(\delta\lambda_{m+1}^n)_{1,2}$. To determine the correct one of these two roots, Crisfield proposed a solution by employing the corresponding vector $(\delta\mathbf{t}_{m+1}^n)_{1,2}$ of the two roots. If the value of the angle between the nth iteration vector $(\Delta\mathbf{t}_{m+1}^n)_{1,2}$ and the $(n-1)$th iteration vector $(\Delta\mathbf{t}_{m+1}^{n-1})$ is positive, the root is appropriate. Furthermore, in the added constraint equation, multiple variables are introduced for a better selection of the root (see Carrera [19].

ALCM and RWRM are also called modified ALM. The result comparison shows that ALCM convergences faster than RWM and RWRM. Lam and Morley [109] proposed a quadratic ALM. The unbalanced load is decomposed into parallel and orthogonal components of the applied external load. This approach avoids the complex process of bringing back root into a quadratic constraint equation and determining the appropriate root.

This method verifies the robustness of dealing with Snap-through and Snap-back problems. Ritto-Corrêa and Camotim [147] presents the implementation of several quadric ALMs in a uniform way, further clearly describing the root selection and line search. A hybrid control method is proposed, where the angle predictor is based on a spherical ALCM and the path corrector is based on a cylindrical ALCM. In the presence of strong nonlinear problems, iterative linear (RWM, RWRM) algorithms sometimes converge to unwanted solutions, see Eriksson and Kouhia [56]. Therefore, it is advocated to use ALCM to solve strong nonlinear problems. Recently, a snap-through analysis for soft solid was carried out by Liu et al. [113], which revealed the effectiveness and robustness of this algorithm. ALCM has been adopted by a variety of commercial FEM software to achieve nonlinear analyses, and it has been extended to studies on advanced structures such as multistable/morphing structures by Groh and Pirrera [78].

2.3.2 Perturbation/Asymptotic Methods

Koiter's Perturbation Method

The Kotier's perturbation/stability method was proposed by Koiter [104], which is hinged on the combination of the perturbation and weighted residual methods. A FEM-based reduced order model with a handful of representative modes was established. First, a perturbation expansion of load and displacement is generated around the bifurcated buckling point. The first-order term in the perturbation expansion corresponds to the bifurcation buckling mode, while the second-order term reflects the correction of the buckling mode in the large deformation state. Then, a certain number of bifurcated buckling modes and second-order modes are employed to describe the initial post-buckling behaviour. The number of equations of the obtained nonlinear algebraic equations is equal to the selected buckling modes in the perturbation expansion. Lanzo and Garcea [111] extended the Koiter's perturbation theory to analyse the effect of residual stress. Additional terms related to residual stress were evaluated by the corresponding weight coefficients. Rahmen and Jansen [139] performed a post-buckling analysis on a cylindrical shell with consideration of the interactions between the representative modes.

Asymptotic Numerical Method

Contrasting Koiter's perturbation method, another category of perturbation methods not only perturbs around the determined bifurcated buckling point but disturbs along the whole path. In other words, the bifurcated buckling point is automatically detected, not artificially given. This perturbation method was initially introduced by Thompson and Walker [157] by coupling FEM to calculate the coefficients of the power series. Then, Noor et al. [133] improved it by coupling the vector basis reduction method. However, the efficiencies of these proposed nonlinear approaches are relatively low due to two reasons. First, the complexity of problem analysis increases dramatically as the

number of terms increases. Secondly, the power series for describing the equilibrium path holds a small convergence radius.

ANM was developed to overcome these barriers by Damil and Potier-Ferry [42] and Cochelin et al. [35], which falls into the category of second-order perturbation methods for resulting nonlinear equations. To illustrate, the equilibrium path solution is expanded into a power series by perturbating the parameters, thereby transforming the nonlinear problem into a set of linear problems. Compared to the previously mentioned path-corrector methods, the perturbation method can establish an analytical expression of the whole equilibrium path, and not only obtain discrete points on the equilibrium path. Consider the quadratic differential equation as:

$$\mathscr{R}(\mathbf{q}, \lambda) = \mathsf{L}(\mathbf{q}) + \mathsf{Q}(\mathbf{q}, \mathbf{q}) - \lambda\mathbf{f} = 0, \tag{2.81}$$

where L is a linear differential operator and Q is a quadratic differential operator, and $\mathbf{f}$ is a known external force. Nonlinearity of the equation comes from the quadratic term Q. The differential equation $\mathscr{R}$ is derived for the unknowns $\mathbf{q}$ and λ to obtain the following equations:

$$\begin{aligned} \frac{\partial\mathscr{R}}{\partial\mathbf{q}} &= \mathsf{L}^t(\mathbf{q}) = \mathsf{L}(\cdot) + 2\mathsf{Q}(\mathbf{q}, \cdot) \\ \frac{\partial\mathscr{R}}{\partial\lambda} &= \mathbf{f} \end{aligned} \tag{2.82}$$

Where $\mathsf{L}^t \in \mathbb{R}^{n\times n}$ is the tangent differential operator, n being the number of equations or the dimension of the unknown. The unknowns $\mathbf{q}$ and λ in the nonlinear systems are all expanded into power series form as:

$$\begin{aligned} \mathbf{q}_{m+1} &= \mathbf{q}_m + a^p\mathbf{q}^p, \\ \lambda_{m+1} &= \lambda_m + a^p\lambda^p \end{aligned} \quad \text{with } p = 1, 2, ..., N_{max}. \tag{2.83}$$

In the formula, $\mathbf{q}^p, \lambda^p(p = 1, 2, ..., N_{max})$ is the coefficient of the power series, which is the unknown quantity to be solved, and $(\mathbf{q}_m, \lambda_m)$ and $(\mathbf{q}_{m+1}, \lambda_{m+1})$ are points on the equilibrium path. For these two points, the differential equation is satisfied as:

$$\mathscr{R}(\mathbf{q}_m, \lambda_m) = \mathsf{L}(\mathbf{q}_m) + \mathsf{Q}(\mathbf{q}_m, \mathbf{q}_m) - \lambda_m\mathbf{f} = 0, \tag{2.84}$$

$$\mathscr{R}(\mathbf{q}_{m+1}, \lambda_{m+1}) = \mathsf{L}(\mathbf{q}_{m+1}) + \mathsf{Q}(\mathbf{q}_{m+1}, \mathbf{q}_{m+1}) - \lambda_{m+1}\mathbf{f} = 0. \tag{2.85}$$

Since $\mathscr{R}$ is a quadratic differential equation, the derivatives of the second and higher orders are all zero. Only the first order derivative of $\mathscr{R}$ is not zero, which is marked as $\nabla\mathscr{R}$ and can be also called as the gradient/Jacobi matrix of $\mathscr{R}$. Consequently, the following equation can be derived:

$$\mathscr{R}(\mathbf{q}_{m+1}, \lambda_{m+1}) = \mathscr{R}(\mathbf{q}_m, \lambda_m) \quad \begin{aligned} &+ a(\nabla\mathscr{R}(\mathbf{q}_m, \lambda_m)(\mathbf{q}^1, \lambda^1)^T) + ... \\ &+ a^p\left(\nabla\mathscr{R}(\mathbf{q}_m, \lambda_m)(\mathbf{q}^p, \lambda^p)^T + \mathbf{f}_{nl}^p\right). \end{aligned} \tag{2.86}$$

Eq ([2.86](2.86)) can be rewritten to the equivalent linear equations as follows

$$a : \nabla \mathcal{R}(\mathbf{q}_m, \lambda_m)(\mathbf{q}^1, \lambda^1)^T) = 0, \tag{2.87}$$

$$a^p : \nabla \mathcal{R}(\mathbf{q}_m, \lambda_m)(\mathbf{q}^p, \lambda^p)^T + \mathbf{f}_{nl}^p = 0 \text{ with } p = 1,2, ..., N_{max}, \tag{2.88}$$

where

$$\nabla \mathcal{R}(\mathbf{q}_m, \lambda_m) = (L^t(\mathbf{q}_m), \lambda_m \mathbf{f}) \tag{2.89}$$

and

$$\mathbf{f}_{nl}^p = \sum_{r=1}^{p-1} Q(\mathbf{q}_r, \mathbf{q}_{p-r}).. \tag{2.90}$$

By substituting Eq. ([2.90](2.90)) and ([2.89](2.89)) into Eq. ([2.87](2.87)) and ([2.88](2.88)) and grouping the terms of the same order, the quadratic differential can be transformed into a series of linear equations as:

$$a : L^t(\mathbf{q}) - \lambda^1 \mathbf{f} = 0, \tag{2.91}$$

$$a^p : L^t(\mathbf{q}) + \sum_{r=1}^{p-1} Q(\mathbf{q}_r, \mathbf{q}_{p-r}) - \lambda^p \mathbf{f} = 0. \tag{2.92}$$

The first order is a linear problem, where $(\mathbf{q}^1, \lambda^1)$ is the tangent vector at the position of $(\mathbf{q}_m, \lambda_m)$. $\mathbf{f}_{nl}^p$ is determined by the displacement vectors $\mathbf{q}^r (r = 1,2, ..., p-1)$. Based on the previous $p-1$ power series coefficients, the nonlinear force can be solved.

There is a total of $(N_{max} + 1)$ unknowns $((q^p, \lambda^p)$ and $a)$, but only $N_m ax$ equations are provided. Therefore, A equation defining the path parameter a is introduced to close the equations as:

$$a = \frac{1}{s^2}[(\mathbf{q}_{m+1} - \mathbf{q}_m)^T \mathbf{q}^1 + (\lambda_{m+1} - \lambda_m)\lambda^1], \tag{2.93}$$

where s is the scale factor. a being the projection of the increment $(\Delta \mathbf{q}_{m+1}, \Delta \lambda_{m+1})$ in the predicted direction (tangential direction) of the first-order solution $(\mathbf{q}^1, \lambda^1)$. By combining Eq. ([2.83](2.83)) with Eq. ([2.93](2.93)), the following equations can be derived by separating terms with the same order of a:

$$a : \mathbf{q}^{1T}\mathbf{q}^1 + \lambda^{12} = 1, \tag{2.94}$$

$$a^p : \mathbf{q}^{1T}\mathbf{q}^p + \lambda^{p2} = 0. \tag{2.95}$$

The above series form can only describe the equilibrium path properly within a certain range, and this range is called the series convergence radius ε. Usually, for ensuring the stability of the calculation, it is necessary to find an effective radius that is less than or equal to the convergence radius, and the latter is defined according to the convergence condition of the power series. At $(m+1)$th step, the displacement for the first N_* orders can be written as:

$$\mathbf{q}_{m+1}^{N_*} = \mathbf{q}_m + a^p \mathbf{q}^p \ p = 1,2, ..., N_*. \tag{2.96}$$

That is when the difference between $\mathbf{q}_{m+1}^{N_*}$ and $\mathbf{q}_{m+1}^{N_*-1}$ is tiny, it can be considered that the effective radius reaches the maximum value. Therefore, the displacement difference between two adjacent orders of the power series needs to be smaller than a given tolerance value ε as:

$$\frac{||\mathbf{q}_{m+1}^{N_*} - \mathbf{q}_{m+1}^{N_*-1}||}{||\mathbf{q}_{m+1}^{N_*} - \mathbf{q}_m||} \leq \varepsilon. \tag{2.97}$$

Obviously, $a^p \mathbf{q}^p$ with $p = 1, 2, ..., N_*$ satisfies as :

$$||a\mathbf{q}^1|| \leq ||\sum_{p=1}^{N_*} a^p \mathbf{q}^p||. \tag{2.98}$$

By the above formula, the effective range of the path parameter is derived as:

$$a \leq (\varepsilon \frac{||\mathbf{q}^1||}{||\mathbf{q}^{N_*}||})^{\frac{1}{N_*-1}}. \tag{2.99}$$

By substituting N_* by the highest order N_{max}, the maximum value of path parameter in the effective radius can be obtained as:

$$a_{max} = (\varepsilon \frac{||\mathbf{q}^1||}{||\mathbf{q}^{N_{max}}||})^{\frac{1}{N_{max}-1}}. \tag{2.100}$$

After assigning the error tolerance ε and the order of power series N_{max}, the step length can be calculated adaptively. By considering the overall relative residual of the differential equation, Zahrouni et al. [169] proposed another method for calculating the effective radius.

This nonlinear solver has two advantages. The first one is that is it step-adaptive. There is no need to set up a step length. This latter will be refined automatically, for instance in the proximity of an instability point. The second advantage is the reduction of matrixes inversion. For one single step, the tangent matrix is inverted only once. As a consequence, it is a robust and effective nonlinear solver.

In most of the numerical asymptotic methods, it is often necessary to derive the corresponding solution format for different problems, which limits the versatility of the ANM. Koutsawa et al. [105] proposed a diamond method based on automatic differentiation technology, which significantly improved the versatility of numerical asymptotic methods. Under the framework of the diamond method, it is feasible to generate the ANM format automatically.

By employing ANM as a nonlinear solver, a series of geometrically nonlinear studies are carried out on the beam structure. Najah [126] considering the two-dimensional cantilever beam model, similar conclusions have been drawn. The introduction of the diamond method marks a significant step forward in the application of numerical asymptotic method engineering. Compared to the RWM employed by the commercial code

ABAQUS, Zahrouni et al. [168] elaborated a study of the large rotational deformation and buckling response of the cantilever beam. Hu et al. [88] addressed the buckling instability of sandwich beams and used the ANM to capture the lowest critical load of the structure with positive symmetry and antisymmetric instability. Then, this work was further exploited by coupling the Arlinque method for a multi-scale (meso-macro) modelling presented by Yu et al. [166]. Recently, by combining with ANM and the slowly varying Fourier coefficients technique, several wrinkling analyses were carried out for thin films (see Huang et al. [91]), circular membranes (see Huang et al. [92]), sandwich plates (see Huang et al. [90]).

Chapter 3

Geometrically Nonlinear Models for Beam Structures

This chapter proposes the formulation of hierarchical macroscale beam models for geometrically nonlinear problems. These models will also serve as the basis for the multi-scale beam model for the geometrically nonlinear problem. A total Lagrangian formulation is used. The derivation is done in the framework of large displacements and rotation but small strains. The preliminary concepts of beam modelling are given. Then, the framework of CUF for the nonlinear beam is presented. Displacement field approximation, the tangent stiffness matrix and the resulting nonlinear problem are derived. Solution by means of ANM is, then, presented. The specific solution procedure for 1st order and 2nd up to a generic p^{th} order is discussed. To maintain a coherent format between the macroscale beam model and multi-scale beam model, the derivation in terms of PK1 stress $\mathbf{P}$ and deformation gradient $\mathbf{F}$ is presented in addition to the formulation in terms of PK2 stress $\mathbf{S}$ and Green-Lagrangian strain $\mathbf{E}$.

3.1   Preliminaries

In a beam structure, a point $\mathbf{X} \in \mathbb{R}^3$ is represented by a Cartesian reference system as:

$$\mathbf{X} = \left\{ \begin{array}{ccc} x & y & z \end{array} \right\}^{T}. \tag{3.1}$$

where y- and z-axis stand for two orthogonal directions laying on the beam cross-section $\square$. The axial direction "x" is in the range $[0, l]$, where l is the beam length. For a two-dimensional problem, terms along the y-axis are neglected. Therefore, the displacement field can be written in the following form:

$$\mathbf{u}(\mathbf{X}) = \mathbf{u}\left(x, z\right) = \left\{ \begin{array}{cc} u_x\left(x, z\right) & u_z\left(x, z\right) \end{array} \right\}^{T} \tag{3.2}$$

where u_x and u_z are the displacement components along $x-$ and z-axis, respectively. $\overleftarrow{\theta}(\mathbf{X}) \in \mathbb{R}^{2\times2}$ is defined as:

$$\overleftarrow{\theta} = \begin{bmatrix} u_{x,x} & u_{x,z} \\ u_{z,x} & u_{z,z} \end{bmatrix} \tag{3.3}$$

that is the matrix rearrangement of the displacement gradient vector $\theta \in \mathbb{R}^4$:

$$\theta(\mathbf{u}) = \nabla\mathbf{u} = \left\{ \begin{array}{cccc} u_{x,x} & u_{x,z} & u_{z,x} & u_{z,z} \end{array} \right\}^T. \tag{3.4}$$

The deformation gradient tensor $\overleftarrow{\mathbf{F}} \in \mathbb{R}^{2\times2}$ is defined as follows:

$$\overleftarrow{\mathbf{F}}(\mathbf{X}) = \overleftarrow{\theta}(\mathbf{u}(\mathbf{X})) + \mathbf{I} = \begin{bmatrix} u_{x,x} + 1 & u_{x,z} \\ u_{z,x} & u_{z,z} + 1 \end{bmatrix}. \tag{3.5}$$

Its vector form $\mathbf{F} \in \mathbb{R}^4$ is:

$$\mathbf{F}(\mathbf{X}) = \begin{bmatrix} u_{x,x} + 1 \\ u_{x,z} \\ u_{x,z} \\ u_{z,z} + 1 \end{bmatrix}. \tag{3.6}$$

Since $\delta\mathbf{I} = 0$ and $d\mathbf{I} = 0$, its virtual variation and infinitesimal variation can be written in the following manner:

$$\delta\mathbf{F} = \delta\theta(\mathbf{u}), \text{ and } d\mathbf{F} = d\theta(\mathbf{u}). \tag{3.7}$$

The Green-Lagrangian strain tensor $\overleftarrow{\mathbf{E}} \in \mathbb{R}^{2\times2}$ becomes:

$$\overleftarrow{\mathbf{E}} = \frac{1}{2}(\overleftarrow{\mathbf{F}}^T \cdot \overleftarrow{\mathbf{F}} - \mathbf{I}), \tag{3.8}$$

whose components are E_{ij} with $i, j = x, z$. Its vector form $\mathbf{E} \in \mathbb{R}^4$ can be written as:

$$\mathbf{E} = \begin{bmatrix} E_{xx} \\ E_{xz} \\ E_{zx} \\ E_{zz} \end{bmatrix} = \begin{bmatrix} u_{x,x} \\ u_{x,z} + u_{z,x} \\ u_{x,z} + u_{z,x} \\ u_{z,z} \end{bmatrix} + \frac{1}{2} \begin{bmatrix} u_{x,x}^2 + u_{z,x}^2 \\ 2u_{x,x}u_{x,z} + 2u_{z,x}u_{z,z} \\ 2u_{x,x}u_{x,z} + 2u_{z,x}u_{z,z} \\ u_{x,z}^2 + u_{z,z}^2 \end{bmatrix} = \mathbf{E}_l + \mathbf{E}_{nl}. \tag{3.9}$$

where $\mathbf{E}_l$ and $\mathbf{E}_{nl}$ represent the linear and non-linear strains, respectively. In compact matrix notation, they read:

$$\mathbf{E}_l = \mathbf{H}\theta(\mathbf{u}), \quad \mathbf{E}_{nl} = \frac{1}{2}\mathbf{A}\left(\theta(\mathbf{u})\right)\theta(\mathbf{u}). \tag{3.10}$$

Matrices $\mathbf{H}$ and $\mathbf{A}\left(\theta(\mathbf{u})\right)$ are defined as:

$$\mathbf{H} = \begin{bmatrix} 1 & 0 & 0 & 0 \\ 0 & 1 & 1 & 0 \\ 0 & 1 & 1 & 0 \\ 0 & 0 & 0 & 1 \end{bmatrix}, \tag{3.11}$$

$$\mathbf{A}\left(\theta(\mathbf{u})\right) = \begin{bmatrix} u_{x,x} & 0 & u_{z,x} & 0 \\ u_{x,z} & u_{x,x} & u_{z,z} & u_{z,x} \\ u_{x,z} & u_{x,x} & u_{z,z} & u_{z,x} \\ 0 & u_{x,z} & 0 & u_{z,z} \end{bmatrix}. \tag{3.12}$$

A virtual variation of the Green-Lagrange strain vector $\mathbf{E}$ is:

$$\delta\mathbf{E} = \delta\left\{\mathbf{H}\theta(\mathbf{u}) + \frac{1}{2}\mathbf{A}\left(\theta(\mathbf{u})\right)\theta(\mathbf{u})\right\} = \mathbf{H}\delta\theta(\mathbf{u}) + \mathbf{A}\left(\theta(\mathbf{u})\right)\delta\theta(\mathbf{u}). \tag{3.13}$$

where δ stands for the virtual variation operator. For a two dimensional problem, the constitutive tensor is C_{ijkl} with $i, j, k, l = 1$ or 3. In the case of an anisotropic material, the reduced material stiffness matrix $\mathbb{C}$ is given by:

$$\mathbb{C} = \begin{bmatrix} \mathbb{C}_{11} & \mathbb{C}_{15} & \mathbb{C}_{15} & \mathbb{C}_{13} \\ \mathbb{C}_{51} & \mathbb{C}_{55} & \mathbb{C}_{55} & \mathbb{C}_{53} \\ \mathbb{C}_{51} & \mathbb{C}_{55} & \mathbb{C}_{55} & \mathbb{C}_{53} \\ \mathbb{C}_{31} & \mathbb{C}_{35} & \mathbb{C}_{35} & \mathbb{C}_{33} \end{bmatrix}. \tag{3.14}$$

According to Voigt notation, the following shorthand notation is assumed: where Voigt notation convention:

$$\begin{aligned} 11 &\to 1 \\ 13 &\to 5 \\ 31 &\to 5 \\ 33 &\to 3 \end{aligned}. \tag{3.15}$$

has been used. The vectorial form of second Piola-Kirchhoff stress tensor $\mathbf{S}$ can be written as:

$$\mathbf{S} = \left\{\begin{array}{cccc} S_{xx} & S_{xz} & S_{zx} & S_{zz} \end{array}\right\}^T. \tag{3.16}$$

Hooke's law is considered:

$$\mathbf{S} = \mathbb{C}\mathbf{E} = \mathbb{C}\mathbf{H}\theta(\mathbf{u}) + \frac{1}{2}\mathbb{C}\mathbf{A}\left(\theta(\mathbf{u})\right)\theta(\mathbf{u}). \tag{3.17}$$

The first Piola-Kirchhoff stress tensor $\overline{\mathbf{P}}$ and the PK2 stress tensor $\overleftarrow{\mathbf{S}}$ are related through:

$$\overline{\mathbf{P}} = \overline{\mathbf{F}} \cdot \overleftarrow{\mathbf{S}}. \tag{3.18}$$

The weak form of the governing equation is obtained using the Principle of Virtual Displacement:

$$\delta\mathscr{L} = \delta\mathscr{L}_{int} - \delta\mathscr{L}_{ext} = 0. \tag{3.19}$$

$\mathscr{L}$ is the total work, and $\mathscr{L}_{ext}$ is the work done by the external forces. $\delta\mathscr{L}_{int}$ is the internal virtual work, and it is defined as:

$$\delta\mathscr{L}_{int} = \int_{\Omega_0} \delta\overline{\mathbf{F}} : \overline{\mathbf{P}}d\Omega = \int_{\Omega_0} \delta\mathbf{E}^T\mathbf{S}d\Omega = \int_{\Omega_0} \delta\theta(\mathbf{u})^T[\mathbf{H} + \mathbf{A}(\theta(\mathbf{u}))]^T\mathbf{S}d\Omega, \tag{3.20}$$

where Ω_0 is the volume of the reference undeformed configuration. An infinitesimal of internal virtual work variation can be written as:

$$d\left(\delta \mathscr{L}_{int}\right) = \int_{\Omega_0} \left[\delta \mathbf{E}^T d\mathbf{S} + d\left(\delta \mathbf{E}^T\right) \mathbf{S}\right] d\Omega. \tag{3.21}$$

After few manipulations (see Crisfield. [37]), Eq. (3.21) can be rewritten in the following form:

$$d\left(\delta \mathscr{L}_{int}\right) = \int_{\Omega_0} \left[\delta \mathbf{E}^T \mathbb{C} d\mathbf{E} + \delta \boldsymbol{\theta}^T \hat{\mathbf{S}} d\boldsymbol{\theta}\right] d\Omega, \tag{3.22}$$

where $\hat{\mathbf{S}} \in \mathbb{R}^{4 \times 4}$ is:

$$\hat{\mathbf{S}} = \begin{bmatrix} S_{xx} & S_{xz} & 0 & 0 \\ S_{xz} & S_{zz} & 0 & 0 \\ 0 & 0 & S_{xx} & S_{xz} \\ 0 & 0 & S_{xz} & S_{zz} \end{bmatrix}. \tag{3.23}$$

When replacing the definition of the strain vector in terms of the deformation gradient vector, the derivative of internal virtual work variation takes the following form:

$$d\left(\delta \mathscr{L}_{int}\right) = \int_{\Omega_0} \delta \boldsymbol{\theta}^T \left\{\left[\mathbf{H}^T + \mathbf{A}^T\left(\boldsymbol{\theta}(\mathbf{u})\right)\right] \mathbb{C} \left[\mathbf{H} + \mathbf{A}\left(\boldsymbol{\theta}(\mathbf{u})\right)\right] + \hat{\mathbf{S}}\right\} d\boldsymbol{\theta} d\Omega. \tag{3.24}$$

For the sake of conciseness, the matrix $\mathbb{H} \in \mathbb{R}^{4 \times 4}$ is defined as follows:

$$\mathbb{H} = \left[\mathbf{H}^T + \mathbf{A}^T\left(\boldsymbol{\theta}(\mathbf{u})\right)\right] \mathbb{C} \left[\mathbf{H} + \mathbf{A}\left(\boldsymbol{\theta}(\mathbf{u})\right)\right] + \hat{\mathbf{S}}. \tag{3.25}$$

Its tensorial form is $\mathscr{H}_{ijkl}$, where $i, j, k, l = 1$ or 2. $\overline{\mathbf{P}}$ can be rewritten as follows

$$\overline{\mathbf{P}} = \mathscr{H} : (\overline{\mathbf{F}} - \mathbf{I}). \tag{3.26}$$

Eq. (3.26) can be transformed into matrix form as:

$$\mathbf{P} = \mathbb{H}\boldsymbol{\theta}. \tag{3.27}$$

By neglecting the body forces and taking the external load by a coefficient λ to a given load $\mathbf{f}$, an infinitesimal variation of the external virtual work can be written as:

$$d(\delta \mathscr{L}_{ext}) = d\lambda \delta \mathbf{u}^T \mathbf{f}, \tag{3.28}$$

Considering Eq. (3.25) and Eq. (3.28), an infinitesimal variation of the total virtual work becomes:

$$d(\delta \mathscr{L}) = \int_{\Omega_0} \delta \boldsymbol{\theta}(\mathbf{u})^T \mathbb{H} d\boldsymbol{\theta}(\mathbf{u}) d\Omega - d\lambda \delta \mathbf{u}^T \mathbf{f}. \tag{3.29}$$

3.2 Hierarchical Beam Elements

3.2.1 Displacement Field Approximation

Within the framework of CUF (see also Subsection 2.1.7), the displacement field in Eq. (3.2) is rewritten as:

$$\mathbf{u}\,(x, z) = F_\tau\,(z)\,u_\tau\,(x)\ \ \tau = 1,\ 2, \dots,\ N_u. \tag{3.30}$$

$F_\tau\,(z)$ is a generic expansion function over the z axis, and N_u denotes the number of accounted terms. By using McLaurin polynomials, a generic N-order displacement field can be expanded as:

$$\begin{aligned}
u_x &= u_{x1} + u_{x2}z + \cdots + u_{x(N+1)}z^N, \\
u_z &= u_{z1} + u_{z2}z + \cdots + u_{z(N+1)}z^N.
\end{aligned} \tag{3.31}$$

By employing the one-dimensional finite element approximation, the displacement $\mathbf{u}(x, z)$ in Eq. (3.30) is further approximated as:

$$\mathbf{u}\,(x, z) = F_\tau\,(z)\,N_i\,(x)\,\mathbf{q}_{\tau i}\ \ \tau = 1,\ 2,\ \dots,\ N_u\ i = 1,\ 2,\ \dots,\ N_n^e \tag{3.32}$$

where N_n^e stands for the number of nodes per element. Linear, quadratic and cubic elements have their corresponding shape functions based on Lagrangian interpolations and are addressed as "B2", "B3" and "B4", respectively. The kinematic and finite element approximation of the displacement gradient vector is formulated as:

$$\boldsymbol{\theta} = \left\{\ \ F_\tau N_{i_{,x}}\mathbf{q}_{\tau i}^u\ \ \ F_{\tau_{,z}}N_i\mathbf{q}_{\tau i}^u\ \ \ F_\tau N_{i_{,x}}\mathbf{q}_{\tau i}^w\ \ \ F_{\tau_{,z}}N_i\mathbf{q}_{\tau i}^w\ \ \right\} = G_{\tau i}\mathbf{q}_{\tau i} \tag{3.33}$$

where $G_{\tau i} \in \mathbb{R}^{4\times 2}$ is:

$$\mathbf{G}_{\tau i} = \begin{bmatrix} F_\tau N_{i_{,x}} & 0 \\ F_{\tau_{,z}}N_i & 0 \\ 0 & F_\tau N_{i_{,x}} \\ 0 & F_{\tau_{,z}}N_i \end{bmatrix} \tag{3.34}$$

and $\mathbf{q}_{\tau i} \in \mathbb{R}^2$ is:

$$\mathbf{q}_{\tau i}^T = \left\{\ q_{\tau i}^u\ \ q_{\tau i}^w\ \right\}. \tag{3.35}$$

3.2.2 Element Tangent Stiffness Matrix

For an element, an infinitesimal variation of internal virtual work variation $\delta\mathscr{L}_{int}^e$ is:

$$d\left(\delta\mathscr{L}_{int}^e\right) = \int_{\Omega_0^e} d\left(\delta\mathbf{E}^T\mathbf{S}\right) d\Omega \tag{3.36}$$

45

where l^e is the element length. Considering the geometrical relations in Eqs. (3.13), the constitutive relations in Eqs. (3.17) and the finite element formulation in Eq. (3.33), Eq. (3.36) becomes:

$$
\begin{aligned}
d\left(\delta\mathscr{L}_{int}^e\right) &= \int_{\Omega_0^e} \delta\theta(\mathbf{u})^T \left\{\left[\mathbf{H}^T + \mathbf{A}^T\right]\mathbb{C}\left[\mathbf{H} + \mathbf{A}\right] + \hat{\mathbf{S}}\right\} d\theta(\mathbf{u})d\Omega \\
&= \delta q_{\tau i}^T \int_{\Omega_0^e} G_{\tau i}^T \left\{\left[\mathbf{H}^T + \mathbf{A}^T\right]\mathbb{C}\left[\mathbf{H} + \mathbf{A}\right] + \hat{\mathbf{S}}\right\} G_{\kappa j}d\Omega dq_{\kappa j} \\
&= \delta q_{\tau i}^T \left(\mathbf{K}_{\tau\kappa ij}^{el} + \mathbf{K}_{\tau\kappa ij}^{et1} + \mathbf{K}_{\tau\kappa ij}^{et2}\right)dq_{\kappa j}.
\end{aligned} \tag{3.37}
$$

The "fundamental nuclei" of the linear $K_{\tau\kappa ij}^{el} \in \mathbb{R}^{2\times2}$, initial-displacement $K_{\tau\kappa ij}^{et1} \in \mathbb{R}^{2\times2}$ and geometric $K_{\tau\kappa ij}^{et2} \in \mathbb{R}^{2\times2}$ tangent stiffness matrices can be written in the following form:

$$
\begin{aligned}
K_{\tau\kappa ij}^{el} &= \int_{\Omega_0^e} G_{\tau i}^T \mathbf{H}^T \mathbb{C}\mathbf{H} G_{\kappa j}d\Omega \\
K_{\tau\kappa ij}^{et1}(q_{\tau i}) &= \int_{\Omega_0^e} G_{\tau i}^T \left[\mathbf{H}^T\mathbb{C}\mathbf{A} + \mathbf{A}^T\mathbb{C}\left(\mathbf{H} + \mathbf{A}\right)\right] G_{\kappa j}d\Omega \\
K_{\tau\kappa ij}^{et2}(q_{\tau i}) &= \int_{\Omega_0^e} G_{\tau i}^T \hat{\mathbf{S}} G_{\kappa j}d\Omega
\end{aligned} \tag{3.38}
$$

The nuclei are not dependent on the approximation order over the thickness (N_u) nor the number of nodes per element along the beam axis (N_n^e), see Carrera et al. [26]. The components of the linear stiffness matrix $\mathbf{K}_{\tau\kappa ij}^{el}$ are:

$$
\begin{aligned}
K_{\tau\kappa ij}^{elxx} &= J_{\tau\kappa}^{11}I_{i,x j,x} + J_{\tau,z\kappa}^{15}I_{ij,x} + J_{\tau\kappa,z}^{15}I_{i,x j} + J_{\tau,z\kappa,z}^{55}I_{ij} \\
K_{\tau\kappa ij}^{elxz} &= J_{\tau\kappa}^{15}I_{i,x j,x} + J_{\tau\kappa,z}^{13}I_{i,x j} + J_{\tau,z\kappa,z}^{35}I_{ij} + J_{\tau,z\kappa}^{55}I_{ij,x} \\
K_{\tau\kappa ij}^{elzx} &= J_{\tau\kappa}^{15}I_{i,x j,x} + J_{\tau,z\kappa}^{13}I_{ij,x} + J_{\tau,z\kappa,z}^{35}I_{ij} + J_{\tau\kappa,z}^{55}I_{i,x j} \\
K_{\tau\kappa ij}^{elzz} &= J_{\tau\kappa,z}^{35}I_{i,x j} + J_{\tau,z\kappa}^{35}I_{ij,x} + J_{\tau\kappa}^{55}I_{i,x j,x} + J_{\tau,z\kappa,z}^{33}I_{ij}
\end{aligned} \tag{3.39}
$$

The generic term $J_{\tau_{(,z)}\kappa_{(,z)}}^{\varphi\varpi}$ is a cross-section moment:

$$
J_{\tau_{(,z)}\kappa_{(,z)}}^{\varphi\varpi} = \int_{\square^e=h^e\times b^e} \mathbb{C}_{\varphi\varpi}F_{\tau_{(,z)}}F_{\kappa_{(,z)}} \, d\square \ . \tag{3.40}
$$

The $I_{i_{(,x)}j_{(,x)}}$ integral can be expressed as follows:

$$
I_{i_{(,x)}j_{(,x)}} = \int_{l^e} N_{i_{(,x)}}N_{j_{(,x)}} \, dx. \tag{3.41}
$$

$\mathbf{K}_{\tau\kappa ij}^{et1}$ components are:

$$
\begin{aligned}
K_{\tau\kappa ij}^{et1xx} = \quad & q_{t\phi_m}^u \left(2J_{\tau\kappa t}^{11} I_{i,x j,x \phi,x} + J_{\tau\kappa,z t,z}^{13} I_{i,x j\phi} + J_{\tau,z\kappa t,z}^{13} I_{ij,x\phi} + 2J_{\tau\kappa t,z}^{15} I_{i,x j,x\phi} + \right.\\
& 2J_{\tau\kappa,z t}^{15} I_{i,x j\phi,x} + 2J_{\tau,z\kappa t}^{15} I_{ij,x\phi,x} + 2J_{\tau,z\kappa,z t,z}^{35} I_{ij\phi} + 2J_{\tau,z\kappa,z t}^{55} I_{ij\phi,x} + \\
& \left. J_{\tau,z\kappa t,z}^{55} I_{ij,x\phi} + J_{\tau\kappa,z t,z}^{55} I_{i,x j\phi} \right) + \\
& q_{t\phi_m}^u q_{s\varrho_m}^u \left(J_{\tau\kappa ts}^{11} I_{i,x j,x \phi,x \varrho,x} + J_{\tau\kappa,z ts,z}^{13} I_{i,x j\phi,x\varrho} + J_{\tau,z\kappa t,z s}^{13} I_{ij,x\phi\varrho,x} + \right.\\
& J_{\tau\kappa ts,z}^{15} I_{i,x j,x\phi,x\varrho} + J_{\tau\kappa,z ts}^{15} I_{i,x j\phi,x\varrho,x} + J_{\tau\kappa t,z s}^{15} I_{i,x j,x\phi\varrho,x} + J_{\tau,z\kappa ts}^{15} I_{ij,x\phi,x\varrho,x} + \\
& J_{\tau\kappa,z t,z s,z}^{35} I_{i,x j\phi\varrho} + J_{\tau,z\kappa t,z s,z}^{35} I_{ij,x\phi\varrho} + J_{\tau,z\kappa,z t,z s}^{35} I_{ij\phi\varrho,x} + J_{\tau,z\kappa,z ts,z}^{35} I_{ij\phi,x\varrho} + \\
& J_{\tau,z\kappa,z t,z s,z}^{33} I_{ij\phi\varrho} + J_{\tau\kappa t,z s,z}^{55} I_{i,x j,x\phi\varrho} + J_{\tau\kappa,z t,z s}^{55} I_{i,x j\phi\varrho,x} + J_{\tau,z\kappa ts,z}^{55} I_{ij,x\phi,x\varrho} + \\
& \left. J_{\tau,z\kappa,z ts}^{55} I_{ij\phi,x\varrho,x} \right)
\end{aligned}
$$

$$
\begin{aligned}
K_{\tau\kappa ij}^{et1xz} = \quad & q_{t\phi_m}^u \left(J_{\tau\kappa,z t}^{13} I_{i,x j\phi,x} + J_{\tau\kappa t}^{15} I_{i,x j,x\phi,x} + J_{\tau\kappa,z t,z}^{35} I_{i,x j\phi} + J_{\tau\kappa t,z}^{55} I_{i,x j,x\phi} + \right.\\
& \left. J_{\tau,z\kappa,z t,z}^{33} I_{ij\phi} + J_{\tau,z\kappa t,z}^{35} I_{ij,x\phi} + J_{\tau,z\kappa,z t}^{35} I_{ij\phi,x} + J_{\tau,z\kappa t}^{55} I_{ij,x\phi,x} \right) + \\
& q_{t\phi_m}^w \left(J_{\tau\kappa t}^{11} I_{i,x j,x\phi,x} + J_{\tau\kappa,z t,z}^{13} I_{i,x j\phi} + J_{\tau\kappa t,z}^{15} I_{i,x j,x\phi} + J_{\tau\kappa,z t}^{15} I_{i,x j\phi,x} + \right.\\
& \left. J_{\tau,z\kappa t}^{15} I_{ij,x\phi,x} + J_{\tau,z\kappa,z t,z}^{35} I_{ij\phi} + J_{\tau,z\kappa t,z}^{55} I_{ij,x\phi} + J_{\tau,z\kappa,z t}^{55} I_{ij\phi,x} \right) + \\
& q_{t\phi_m}^u q_{s\varrho_m}^w \left(J_{\tau\kappa ts}^{11} I_{i,x j,x\phi,x\varrho,x} + J_{\tau\kappa,z ts,z}^{13} I_{i,x j\phi,x\varrho} + J_{\tau\kappa ts,z}^{15} I_{i,x j,x\phi,x\varrho} + \right.\\
& J_{\tau\kappa,z ts}^{15} I_{i,x j\phi,x\varrho,x} + J_{\tau\kappa t,z s}^{15} I_{i,x j,x\phi\varrho,x} + J_{\tau\kappa,z t,z s,z}^{35} I_{i,x j\phi\varrho} + J_{\tau\kappa t,z s,z}^{55} I_{i,x j,x\phi\varrho} + \\
& J_{\tau\kappa,z t,z s}^{55} I_{i,x j\phi\varrho,x} + J_{\tau,z\kappa t,z s}^{13} I_{ij,x\phi\varrho,x} + J_{\tau,z\kappa,z t,z s,z}^{33} I_{ij\phi\varrho} + J_{\tau,z\kappa t,z s,z}^{35} I_{ij,x\phi\varrho} + \\
& J_{\tau,z\kappa,z t,z s}^{35} I_{ij\phi\varrho,x} + J_{\tau,z\kappa ts}^{15} I_{ij,x\phi,x\varrho,x} + J_{\tau,z\kappa,z ts,z}^{35} I_{ij\phi,x\varrho} + J_{\tau,z\kappa ts,z}^{55} I_{ij,x\phi,x\varrho} + \\
& \left. J_{\tau,z\kappa,z ts}^{55} I_{ij\phi,x\varrho,x} \right)
\end{aligned}
$$

$$
\begin{aligned}
K_{\tau\kappa ij}^{et1zx} =\ & q_{t\phi_m}^{u} \Big(J_{\tau\kappa t}^{15} I_{i_{,x}j_{,x}\phi_{,x}} + J_{\tau\kappa_{,z}t_{,z}}^{35} I_{i_{,x}j\phi} + J_{\tau\kappa t_{,z}}^{55} I_{i_{,x}j\phi} + J_{\tau\kappa_{,z}t}^{55} I_{i_{,x}j\phi_{,x}} + \\
& J_{\tau_{,z}\kappa t}^{13} I_{ij_{,x}\phi_{,x}} + J_{\tau_{,z}\kappa_{,z}t_{,z}}^{33} I_{ij\phi} + J_{\tau_{,z}\kappa t_{,z}}^{35} I_{ij_{,x}\phi} + J_{\tau_{,z}\kappa_{,z}t}^{35} I_{ij\phi_{,x}} \Big) + \\
& q_{t\phi_m}^{w} \Big(J_{\tau\kappa t}^{11} I_{i_{,x}j_{,x}\phi_{,x}} + J_{\tau\kappa_{,z}t}^{15} I_{i_{,x}j\phi_{,x}} + J_{\tau\kappa t_{,z}}^{15} I_{i_{,x}j_{,x}\phi} + J_{\tau\kappa_{,z}t_{,z}}^{55} I_{i_{,x}j\phi} + \\
& J_{\tau_{,z}\kappa t_{,z}}^{13} I_{ij_{,x}\phi} + J_{\tau_{,z}\kappa_{,z}t_{,z}}^{35} I_{ij\phi} + J_{\tau_{,z}\kappa t}^{15} I_{ij_{,x}\phi_{,x}} + J_{\tau_{,z}\kappa_{,z}t}^{55} I_{ij\phi_{,x}} \Big) + \\
& q_{t\phi_m}^{w} q_{s\varrho_m}^{u} \Big(J_{\tau\kappa ts}^{11} I_{i_{,x}j_{,x}\phi_{,x}\varrho_{,x}} + J_{\tau\kappa_{,z}ts_{,z}}^{13} I_{i_{,x}j\phi_{,x}\varrho} + J_{\tau\kappa ts_{,z}}^{15} I_{i_{,x}j_{,x}\phi_{,x}\varrho} + \\
& J_{\tau\kappa_{,z}ts}^{15} I_{i_{,x}j\phi_{,x}\varrho_{,x}} + J_{\tau\kappa t_{,z}s}^{15} I_{i_{,x}j_{,x}\phi\varrho_{,x}} + J_{\tau\kappa_{,z}t_{,z}s_{,z}}^{35} I_{i_{,x}j\phi\varrho} + J_{\tau\kappa t_{,z}s_{,z}}^{55} I_{i_{,x}j_{,x}\phi\varrho} + \\
& J_{\tau\kappa_{,z}t_{,z}s}^{55} I_{i_{,x}j\phi\varrho_{,x}} + J_{\tau_{,z}\kappa t_{,z}s}^{13} I_{ij_{,x}\phi\varrho_{,x}} + J_{\tau_{,z}\kappa_{,z}t_{,z}s_{,z}}^{33} I_{ij\phi\varrho} + J_{\tau_{,z}\kappa t_{,z}s_{,z}}^{35} I_{ij_{,x}\phi\varrho} + \\
& J_{\tau_{,z}\kappa_{,z}t_{,z}s}^{35} I_{ij\phi\varrho_{,x}} + J_{\tau_{,z}\kappa ts}^{15} I_{ij_{,x}\phi_{,x}\varrho_{,x}} + J_{\tau_{,z}\kappa_{,z}ts_{,z}}^{35} I_{ij\phi_{,x}\varrho} + J_{\tau_{,z}\kappa ts_{,z}}^{55} I_{ij_{,x}\phi_{,x}\varrho} + \\
& J_{\tau_{,z}\kappa_{,z}ts}^{55} I_{ij\phi_{,x}\varrho_{,x}} \Big)
\end{aligned}
$$

$$(3.42)$$

$$
\begin{aligned}
K_{\tau\kappa ij}^{et1zz} =\ & q_{t\phi_m}^{w} \Big(J_{\tau\kappa_{,z}t}^{13} I_{i_{,x}j\phi_{,x}} + J_{\tau_{,z}\kappa t}^{13} I_{ij_{,x}\phi_{,x}} + 2J_{\tau\kappa t}^{15} I_{i_{,x}j_{,x}\phi_{,x}} + 2J_{\tau\kappa_{,z}t_{,z}}^{35} I_{i_{,x}j\phi} + \\
& 2J_{\tau_{,z}\kappa t_{,z}}^{35} I_{i_{,x}j\phi} + 2J_{\tau_{,z}\kappa_{,z}t}^{35} I_{ij\phi_{,x}} + 2J_{\tau\kappa t_{,z}}^{55} I_{i_{,x}j_{,x}\phi} + J_{\tau\kappa_{,z}t}^{55} I_{i_{,x}j\phi_{,x}} \Big) + \\
& J_{\tau_{,z}\kappa t}^{55} I_{ij_{,x}\phi_{,x}} + 2J_{\tau_{,z}\kappa_{,z}t_{,z}}^{33} I_{ij\phi} \Big) + \\
& q_{t\phi_m}^{w} q_{s\varrho_m}^{w} \Big(J_{\tau\kappa ts}^{11} I_{i_{,x}j_{,x}\phi_{,x}\varrho_{,x}} + J_{\tau_{,z}\kappa_{,z}t_{,z}s_{,z}}^{33} I_{ij\phi\varrho} + J_{\tau\kappa t_{,z}s_{,z}}^{55} I_{i_{,x}j_{,x}\phi\varrho} + \\
& J_{\tau\kappa_{,z}t_{,z}s}^{55} I_{i_{,x}j\phi\varrho_{,x}} + J_{\tau_{,z}\kappa ts_{,z}}^{55} I_{ij_{,x}\phi_{,x}\varrho} + J_{\tau_{,z}\kappa_{,z}ts}^{55} I_{ij\phi_{,x}\varrho_{,x}} + J_{\tau\kappa_{,z}ts_{,z}}^{13} I_{i_{,x}j\phi_{,x}\varrho} + \\
& J_{\tau_{,z}\kappa t_{,z}s}^{13} I_{ij_{,x}\phi\varrho_{,x}} + J_{\tau\kappa ts_{,z}}^{15} I_{i_{,x}j_{,x}\phi_{,x}\varrho} + J_{\tau\kappa_{,z}ts}^{15} I_{i_{,x}j\phi_{,x}\varrho_{,x}} + J_{\tau\kappa t_{,z}s}^{15} I_{i_{,x}j_{,x}\phi\varrho_{,x}} + \\
& J_{\tau_{,z}\kappa ts}^{15} I_{ij_{,x}\phi_{,x}\varrho_{,x}} + J_{\tau\kappa_{,z}t_{,z}s_{,z}}^{35} I_{i_{,x}j\phi\varrho} + J_{\tau_{,z}\kappa t_{,z}s_{,z}}^{35} I_{ij_{,x}\phi\varrho} + J_{\tau_{,z}\kappa_{,z}t_{,z}s}^{35} I_{ij\phi\varrho_{,x}} + \\
& J_{\tau_{,z}\kappa_{,z}ts_{,z}}^{35} I_{ij\phi_{,x}\varrho} \Big)
\end{aligned}
$$

$\mathbf{K}^{et2}_{\tau\kappa ij}$ components are:

$$
\begin{aligned}
K^{et2xx}_{\tau\kappa ij} = \ & q^u_{t\phi_m}\left(J^{11}_{\tau\kappa t}I_{i_{,x}j_{,x}\phi_{,x}} + J^{15}_{\tau\kappa t_{,z}}I_{i_{,x}j_{,x}\phi} + J^{15}_{\tau\kappa_{,z}t}I_{i_{,x}j\phi_{,x}} + J^{55}_{\tau\kappa_{,z}t_{,z}}I_{i_{,x}j\phi} + \right.\\
& \left. J^{15}_{\tau_{,z}\kappa t}I_{ij_{,x}\phi_{,x}} + J^{55}_{\tau_{,z}\kappa t_{,z}}I_{ij_{,x}\phi} + J^{13}_{\tau_{,z}\kappa_{,z}t}I_{ij\phi_{,x}} + J^{35}_{\tau_{,z}\kappa_{,z}t_{,z}}I_{ijl} \right)\\
& q^w_{t\phi_m}\left(J^{13}_{\tau\kappa t_{,z}}I_{i_{,x}j_{,x}\phi} + J^{15}_{\tau\kappa t}I_{i_{,x}j_{,x}\phi_{,x}} + J^{35}_{\tau\kappa_{,z}t_{,z}}I_{i_{,x}j\phi} + J^{55}_{\tau\kappa_{,z}t}I_{i_{,x}j\phi_{,x}} + \right.\\
& \left. J^{35}_{\tau_{,z}\kappa t_{,z}}I_{ij_{,x}\phi} + J^{55}_{\tau_{,z}\kappa t}I_{ij_{,x}\phi_{,x}} + J^{33}_{\tau_{,z}\kappa_{,z}t_{,z}}I_{ij\phi} + J^{35}_{\tau_{,z}\kappa_{,z}t}I_{ij\phi_{,x}} \right)\\
& \frac{1}{2}\left(q^u_{t\phi_m}q^u_{s\varrho_m} + q^w_{t\phi_m}q^w_{s\varrho_m} \right)\left(J^{11}_{\tau\kappa ts}I_{i_{,x}j_{,x}\phi_{,x}\varrho_{,x}} + J^{13}_{\tau\kappa t_{,z}s_{,z}}I_{i_{,x}j_{,x}\phi\varrho} + \right.\\
& J^{15}_{\tau\kappa t_{,z}s}I_{i_{,x}j_{,x}\phi\varrho_{,x}} + J^{15}_{\tau\kappa ts_{,z}}I_{i_{,x}j_{,x}\phi_{,x}\varrho} + J^{15}_{\tau\kappa_{,z}ts}I_{i_{,x}j\phi_{,x}\varrho_{,x}} + J^{35}_{\tau\kappa_{,z}t_{,z}s_{,z}}I_{i_{,x}j\phi\varrho} + \quad\cdot\\
& J^{55}_{\tau\kappa_{,z}t_{,z}s}I_{i_{,x}j\phi\varrho_{,x}} + J^{55}_{\tau\kappa_{,z}ts_{,z}}I_{i_{,x}j\phi_{,x}\varrho} + J^{15}_{\tau_{,z}\kappa ts}I_{ij_{,x}\phi_{,x}\varrho_{,x}} + J^{35}_{\tau_{,z}\kappa t_{,z}s_{,z}}I_{ij_{,x}\phi\varrho} + \\
& J^{55}_{\tau_{,z}\kappa t_{,z}s}I_{ij_{,x}\phi\varrho_{,x}} + J^{55}_{\tau_{,z}\kappa ts_{,z}}I_{ij_{,x}\phi_{,x}\varrho} + J^{13}_{\tau_{,z}\kappa_{,z}ts}I_{ij\phi_{,x}\varrho_{,x}} + J^{33}_{\tau_{,z}\kappa_{,z}t_{,z}s_{,z}}I_{ij\phi\varrho} + \\
& \left. J^{35}_{\tau_{,z}\kappa_{,z}t_{,z}s}I_{ij\phi\varrho_{,x}} + J^{35}_{\tau_{,z}\kappa_{,z}ts_{,z}}I_{ij\phi_{,x}\varrho} \right)
\end{aligned}
$$

$$
K^{et2zz}_{\tau\kappa ij} = K^{et2xx}_{\tau\kappa ij}
$$

$$
K^{et2xz}_{\tau\kappa ij} = K^{et2zx}_{\tau\kappa ij} = 0
$$

$$(3.43)$$

The integrals $J^{\varphi\varpi}_{\tau_{(,z)}\kappa_{(,z)}t_{(,z)}}$, $J^{\varphi\varpi}_{\tau_{(,z)}\kappa_{(,z)}t_{(,z)}s_{(,z)}}$, $I_{i_{(,x)}j_{(,x)}\phi_{(,x)}}$ and $I_{i_{(,x)}j_{(,x)}\phi_{(,x)}m_{(,x)}}$ in Eqs. (3.42) and (3.43) are

$$
J^{\varphi\varpi}_{\tau_{(,z)}\kappa_{(,z)}t_{(,z)}} = \int\limits_{\square^e=h^e\times b^e} \mathbb{C}_{\varphi\varpi}F_{\tau_{(,z)}}F_{\kappa_{(,z)}}F_{t_{(,z)}}\,d\square \tag{3.44}
$$

$$
J^{\varphi\varpi}_{\tau_{(,z)}\kappa_{(,z)}t_{(,z)}s_{(,z)}} = \int\limits_{\square^e=h^e\times b^e} \mathbb{C}_{\varphi\varpi}F_{\tau_{(,z)}}F_{\kappa_{(,z)}}F_{t_{(,z)}}F_{s_{(,z)}}\,d\square \tag{3.45}
$$

$$
I_{i_{(,x)}j_{(,x)}\phi_{(,x)}} = \int\limits_{l^e} N_{i_{(,x)}}N_{j_{(,x)}}N_{\phi_{(,x)}}\,dx \tag{3.46}
$$

$$
I_{i_{(,x)}j_{(,x)}\phi_{(,x)}\varrho_{(,x)}} = \int\limits_{l^e} N_{i_{(,x)}}N_{j_{(,x)}}N_{\phi_{(,x)}}N_{\varrho_{(,x)}}\,dx. \tag{3.47}
$$

the tangent stiffness matrix fundamental nucleus reads:

$$
K^e_{\tau\kappa ij} = K^{el}_{\tau\kappa ij} + K^{et1}_{\tau\kappa ij} + K^{et2}_{\tau\kappa ij}(\theta \tag{3.48}
$$

3.2.3 Resulting Nonlinear Problem

Once the approximation order N and the number of nodes per element N_n^e have been fixed, the elemental tangent stiffness matrix can be directly obtained by assembling the nuclei. The global structural tangent stiffness matrix is then obtained by assembling all the element matrices as classically done in a finite element procedure. An infinitesimal variation of the internal virtual work for the beam $d\left(\delta\mathscr{L}_{int}\right)$ can be written in compact form as:

$$d\left(\delta\mathscr{L}_{int}\right) = \sum_{e=1}^{Ne} d\left(\delta\mathscr{L}_{int}^e\right) = \sum_{e=1}^{Ne} \delta\mathbf{q}_{\tau i}^{e\,T} K_{\tau\kappa ij}^e d\mathbf{q}_{\kappa j}^e. \tag{3.49}$$

By assembling the elemental stiffness matrix $K_{\tau\kappa ij}^e$, the global stiffness matrix can be constructed as shown in Fig 3.1.
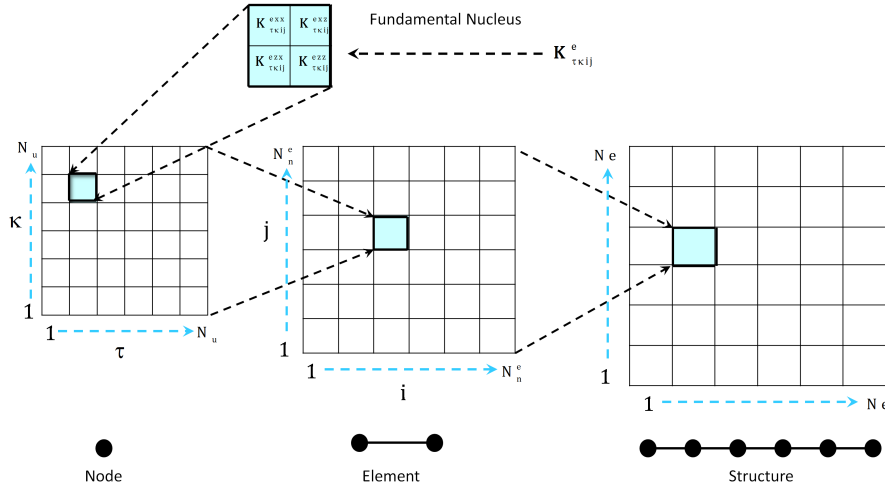
Figure 3.1: Schematic diagram of the assembling of the global stiffness matrix.

Finally, an infinitesimal variation of the external virtual work $\delta\mathscr{L}_{ext}$ can be written as:

$$d\left(\delta\mathscr{L}_{ext}\right) = \sum_{e=1}^{Ne} d\lambda\,\delta\mathbf{u}^{e\,T}\mathbf{f}^e = d\lambda \sum_{e=1}^{Ne} \delta\mathbf{q}_{\tau i}^{e\,T} N_i^T F_\tau^T \mathbf{f}^e. \tag{3.50}$$

3.2.4 Shear and Membrane Locking: MITC Beam Elements

To reduce the effect of the locking effects, the Mixed Interpolation of Tensorial Components (MITC) method is introduced. As well known from literature, membrane and shear locking make the element perform poorly. Locking effects negatively affect the solution accuracy when linear shape functions are used to model slender structures

(see Bucalem and Bathe [17] and Reddy [142] for more details). The MITC technique can be briefly summarised as interpolating displacements and strains separately under the consistency conditions, and then connecting these interpolations at some "tying points". The strain components are written using the following interpolation:

$$\bar{E}_{xx} = \bar{N}_\alpha E_{xx}^\alpha$$
$$\bar{E}_{zz} = \bar{N}_\alpha E_{zz}^\alpha \qquad \alpha = 1, ..., N_n^e - 1.$$
$$\bar{E}_{xz} = \bar{N}_\alpha E_{xz}^\alpha$$

(3.51)

E_{xx}^α, E_{zz}^α and E_{xz}^α are the strain components computed from the geometrical relations in Eq. (3.10) evaluated at the α-th tying point $\chi_{T\alpha}$, which belongs to a set of points along the natural coordinate χ. Besides, $\bar{N}_\alpha$ are the assumed interpolating functions. Their expressions as functions of the natural beam element coordinate $\mathbf{X}$ are provided in Carrera et al. [30]. For B2, B3 and B4 elements, they are:

- B2:

$$\bar{N}_1 = 1$$
$$\chi_{T1} = 0$$

(3.52)

- B3:

$$\bar{N}_1 = -\frac{1}{2}\sqrt{3}\left(\chi - \frac{1}{\sqrt{3}}\right) \quad \bar{N}_2 = \frac{1}{2}\sqrt{3}\left(\chi + \frac{1}{\sqrt{3}}\right)$$
$$\chi_{T1} = -\frac{1}{\sqrt{3}} \quad \chi_{T2} = \frac{1}{\sqrt{3}}$$

(3.53)

- B4:

$$\bar{N}_1 = \frac{5}{6}\chi\left(\chi - \sqrt{\frac{3}{5}}\right) \quad \bar{N}_2 = -\frac{5}{3}\left(\chi - \sqrt{\frac{3}{5}}\right)\left(\chi + \sqrt{\frac{3}{5}}\right) \quad \bar{N}_3 = \frac{5}{6}\chi\left(\chi + \sqrt{\frac{3}{5}}\right)$$
$$\chi_{T1} = -\sqrt{\frac{3}{5}} \quad \chi_{T2} = 0 \quad \chi_{T3} = \sqrt{\frac{3}{5}}$$

(3.54)

In a MITC beam element, the I-integrals in Eqs. (3.41), (3.46), (3.47) are substituted by $\bar{I}$-integrals as:

$$\bar{I}_{i_{(,x)}j_{(,x)}} = \int_{l^e} \bar{N}_\alpha N_{i_{(,x)}}^\alpha \bar{N}_\beta N_{j_{(,x)}}^\beta \, dx$$

(3.55)

$$\bar{I}_{i_{(,x)}j_{(,x)}\phi_{(,x)}} = \int_{l^e} \bar{N}_\alpha N_{i_{(,x)}}^\alpha \bar{N}_\beta N_{j_{(,x)}}^\beta N_{\phi_{(,x)}}^q \, dx$$

(3.56)

$$\overline{I}_{i_{(,x)}j_{(,x)}\phi_{(,x)}m_{(,x)}} = \int_{l^e} \overline{N}_\alpha N^\alpha_{i_{(,x)}} N^\alpha_{j_{(,x)}} \overline{N}_\beta N^\beta_{\phi_{(,x)}} N^\beta_{\varrho_{(,x)}} \, dx. \tag{3.57}$$

3.3   Asymptotic Numerical Method

The Asymptotic numerical method is employed to solve the set of Eq. (3.58) accompanied by the boundary conditions (see Cochelin et al. [35] for more details). At step $m+1$, the solution point $(\mathbf{u}_{m+1}, \boldsymbol{\theta}_{m+1}, \mathbf{E}_{m+1}, \mathbf{S}_{m+1}, \lambda_{m+1})$ is determined from the previous solution point $(\mathbf{u}_m, \boldsymbol{\theta}_m, \mathbf{E}_m, \mathbf{S}_m, \lambda_m)$. Following a perturbation technique, an approached solution path is characterised by a truncated power series of order N_{max}:

$$\begin{aligned}
\mathbf{u}_{m+1} &= \mathbf{u}_m + a^p \mathbf{u}^p, \\
\mathbf{E}_{m+1} &= \mathbf{E}_m + a^p \mathbf{E}^p, \\
\mathbf{S}_{m+1} &= \mathbf{S}_m + a^p \mathbf{S}^p, \quad p = 1, 2, ..., N_{max}. \\
\boldsymbol{\theta}_{m+1} &= \boldsymbol{\theta}_m + a^p \boldsymbol{\theta}^p, \\
\lambda_{m+1} &= \lambda_m + a^p \lambda^p.
\end{aligned} \tag{3.58}$$

where a is a path parameter. Superscript p represents the expansion order. There are $5N_{max}+1$ unknowns $(\mathbf{u}^p, \boldsymbol{\theta}^p, \mathbf{E}^p, \mathbf{S}^p, \lambda^p, a)$ in the $5N_{max}$ equations above. Therefore, the following complimentary equation should be introduced to solve the system: the path parameter a is defined by imposing it to be parallel to the projection of the increment on the tangent direction $(\mathbf{u}^1, \lambda^1)$:

$$a = \mathbf{u}^1(\mathbf{u} - \mathbf{u}_m) + \lambda^1(\lambda - \lambda_m). \tag{3.59}$$

The validity range of the truncated series is determined by the maximum value of the path parameter a_{max}:

$$a_{max} = \left(\varepsilon \frac{||\mathbf{u}^1||}{||\mathbf{u}^{N_{max}}||}\right)^{\frac{1}{N_{max}-1}}. \tag{3.60}$$

where ε is a tolerance whose value is chosen by the user and $|| \cdot ||$ is the vector norm. By substituting the approached solution in Eq. (3.58) into the following equation:

$$\int_{\Omega_0} \delta\boldsymbol{\theta}(\mathbf{u})^T \mathbb{H}\boldsymbol{\theta}(\mathbf{u}) d\Omega = \lambda \delta\mathbf{u}^T \mathbf{f} \tag{3.61}$$

It results in a linear system of equations. For the sake of clearness, control equations recalled Table 3.1 can be expanded as:

$$\begin{aligned}
&\int_{\Omega_0} \delta\boldsymbol{\theta}^T \left[\mathbf{H} + \mathbf{A}\left(\boldsymbol{\theta}_m + a^r\boldsymbol{\theta}^r\right)\right]^T \left(\mathbf{S}_m + a^g\mathbf{S}^g\right) d\Omega = \left(\lambda_m + a^p\lambda^p\right)\delta\mathbf{u}^T\mathbf{f} \\
&\mathbf{S}_m + a^p\mathbf{S}^p = \mathbb{C}\left(\mathbf{E}_m + a^p\mathbf{E}^p\right) \\
&\mathbf{E}_m + a^p\mathbf{E}^p = \left(\mathbf{H} + \frac{1}{2}\mathbf{A}\left(\boldsymbol{\theta}_m + a^i\boldsymbol{\theta}^i\right)\right)\left(\boldsymbol{\theta}_m + a^j\boldsymbol{\theta}^j\right) \\
&\boldsymbol{\theta}_m + a^p\boldsymbol{\theta}^p = \nabla\left(\mathbf{u}_m + a^p\mathbf{u}^p\right) \\
&a = \mathbf{u}^1\left[\left(\mathbf{u}_m + a^p\mathbf{u}^p\right) - \mathbf{u}_m\right] + \lambda^1\left(\left(\lambda_m + a^p\lambda^p\right) - \lambda_m\right)
\end{aligned} \tag{3.62}$$

Table 3.1: Problem control equations.

Virtual work equation	$\int_{\Omega_0} \delta\boldsymbol{\theta}^T \left([\mathbf{H} + \mathbf{A}(\theta(\mathbf{u}))]^T \mathbf{S}\right) d\Omega = \lambda \delta\mathbf{u}^T \mathbf{f}$
Hook's Law	$\mathbf{S} = \mathbb{C}\mathbf{E}$
Kinematic relations	$\mathbf{E} = (\mathbf{H} + \dfrac{1}{2}\mathbf{A}\,(\theta))\theta$
	$\theta = \nabla\mathbf{u}$
Path parameter	$a = \mathbf{u}^1(\mathbf{u} - \mathbf{u}_m) + \lambda^1(\lambda - \lambda_m)$

For the sake of completeness, the formulation in terms of PK1 and the deformation gradient is also presented:

$$
\begin{aligned}
&\int_{\Omega_0} \delta\overline{\mathbf{F}}^T : \overline{\mathbf{P}}d\Omega = \lambda\delta\mathbf{u}^T : \mathbf{f} \\
&\overline{\mathbf{P}} = \overline{\mathbf{F}} \cdot \overline{\mathbf{S}} \\
&\overline{\mathbf{E}} = \frac{1}{2}(\overline{\mathbf{F}}^T \cdot \overline{\mathbf{F}} - \mathbf{I}) \\
&\overline{\mathbf{F}}(\mathbf{X}) = \overline{\theta}(\mathbf{u}(\mathbf{X})) + \mathbf{I}
\end{aligned}
\tag{3.63}
$$

For more details, refer to Nezamabadi [129]. These two forms are equivalent. The expanded form of PK1 stress $\overline{\mathbf{P}}$ is:

$$
\overline{\mathbf{P}}_m + a^p\overline{\mathbf{P}}^p = (\overline{\mathbf{F}}_m + a^r\overline{\mathbf{F}}^r) \cdot (\overline{\mathbf{S}}_m + a^g\overline{\mathbf{S}}^g).
\tag{3.64}
$$

The deformation gradient is expanded as:

$$
\overline{\mathbf{F}}_m + a^p\overline{\mathbf{F}}^p = \overline{\theta}_m + \mathbf{I} + a^p\overline{\theta}^p.
\tag{3.65}
$$

It should be noted that $\overleftarrow{\mathbf{F}^p}$ equals to $\overleftarrow{\theta}^p$. By collecting the terms with the same power of a, the algebraic equations for first order up to order N_{max} is derived.

3.3.1 First-order Perturbation Term

The control equations for the first order perturbation term can be written in the following form:

$$
\begin{aligned}
&\int_{\Omega_0} \delta\boldsymbol{\theta}^T\left[\mathbf{H} + \mathbf{A}\left(\theta_m\right)\right]^T\mathbf{S}^1 + \mathbf{A}\left(\theta^1\right)^T\mathbf{S}_m d\Omega = \lambda^1\delta\mathbf{u}^T\mathbf{f} \\
&\mathbf{S}^1 = \mathbb{C}\left[\mathbf{H} + \mathbf{A}\left(\theta_m\right)\right]\theta^1 \\
&\mathbf{u}^{1T}\mathbf{u}^1 + \lambda^{1^2} = 1
\end{aligned}
\tag{3.66}
$$

The term $\mathbf{A}\left(\theta^1\right)^T\mathbf{S}_m$ can be rewritten as follows (see Crisfield. [37]):

$$
\mathbf{A}\left(\theta^1\right)^T\mathbf{S}_m = \hat{\mathbf{S}}_m\theta^1.
\tag{3.67}
$$

By substituting terms in the first equation in Eq. (3.66) with Eq. (3.67), the following equation can be derived as:

$$\int_{\Omega_0} \delta\boldsymbol{\theta}^T \left[\mathbf{H} + \mathbf{A}\left(\boldsymbol{\theta}_m\right)\right]^T \mathbb{C}\left[\mathbf{H} + \mathbf{A}\left(\boldsymbol{\theta}_m\right)\right]\boldsymbol{\theta}^1 + \hat{\mathbf{S}}_m \boldsymbol{\theta}^1 d\Omega = \lambda^1 \delta\mathbf{u}^T \mathbf{f}. \tag{3.68}$$

Using Eq. (3.25), the previous equation reads:

$$\int_{\Omega_0} \delta\boldsymbol{\theta}^T \mathbb{H}_m \boldsymbol{\theta}^1 d\Omega = \lambda^1 \delta\mathbf{u}^T \mathbf{f} \tag{3.69}$$

Based on Eq. (3.27), 1$^{\text{st}}$ order PK1 stress $\overline{\mathbf{P}}^1$ can be rewritten as:

$$\mathbf{P}^1 = \mathbb{H}_m \boldsymbol{\theta}^1, \tag{3.70}$$

and its tensor form is

$$\overline{\mathbf{P}}^1 = \mathscr{H}_m : \overleftarrow{\boldsymbol{\theta}}^1. \tag{3.71}$$

3.3.2   Second to p^{th}-order Perturbation Terms

The equivalence of Eqs. (3.66) at p^{th} order are given by:

$$\int_{\Omega_0} \delta\boldsymbol{\theta}^T \left[\mathbf{H} + \mathbf{A}\left(\boldsymbol{\theta}_m\right)\right]^T \mathbf{S}^p + \mathbf{A}\left(\boldsymbol{\theta}^p\right)^T \mathbf{S}_m + \mathbf{P}_{nl}^{p\,I} d\Omega = \lambda^p \delta\mathbf{u}^T \mathbf{f}$$
$$\mathbf{S}^p = \mathbb{C}\left[\mathbf{H} + \mathbf{A}\left(\boldsymbol{\theta}_m\right)\right]\boldsymbol{\theta}^p + \mathbf{S}_{nl}^p \tag{3.72}$$
$$\mathbf{u}^{1\,T}\mathbf{u}^p + \lambda^{p2} = 0$$

λ_p represents the p$^{\text{th}}$ load proportional parameter. In contrast to the 1$^{\text{st}}$ order PK2 stress, there are two extra terms at each order p: $\mathbf{S}_{nl}^p$ and $\mathbf{P}_{nl}^{p\,I}$. Nonlinear part of p$^{\text{th}}$ order PK2 stress $\mathbf{S}_{nl}^p$ is composed of the displacements and stresses at orders anterior to the order p:

$$\mathbf{S}_{nl}^p = \frac{1}{2}\mathbb{C} \sum_{r=1}^{p-1} \mathbf{A}(\boldsymbol{\theta}^{p-r})\boldsymbol{\theta}^r. \tag{3.73}$$

The other extra term is $\mathbf{P}_{nl}^{p\,II}$ as follows

$$\mathbf{P}_{nl}^{p\,II} = \sum_{r=1}^{p-1} \mathbf{A}^T(\boldsymbol{\theta}^{p-r})\mathbf{S}^r. \tag{3.74}$$

Taking into account Eq. (3.73), the left side of the first equation in Eq. (3.72) can be rewritten as:

$$
\begin{aligned}
&\int_{\Omega_0} \delta\boldsymbol{\theta}^T \left[\mathbf{H} + \mathbf{A}\left(\boldsymbol{\theta}_m\right)\right]^T \left[\mathbb{C}\left[\mathbf{H} + \mathbf{A}\left(\boldsymbol{\theta}_m\right)\right]\boldsymbol{\theta}^p + \mathbf{S}_{nl}^p\right] + \mathbf{A}\left(\boldsymbol{\theta}^p\right)^T \mathbf{S}_m \, d\Omega \\
=\ &\int_{\Omega_0} \delta\boldsymbol{\theta}^T \left[\mathbf{H} + \mathbf{A}\left(\boldsymbol{\theta}_m\right)\right]^T \mathbb{C}\left[\mathbf{H} + \mathbf{A}\left(\boldsymbol{\theta}_m\right)\right]\boldsymbol{\theta}^p + \hat{\mathbf{S}}_m \boldsymbol{\theta}^p + \left[\mathbf{H} + \mathbf{A}\left(\boldsymbol{\theta}_m\right)\right]^T \mathbf{S}_{nl}^p \, d\Omega \\
=\ &\int_{\Omega_0} \delta\boldsymbol{\theta}^T \mathbb{H}\boldsymbol{\theta}^p + \left[\mathbf{H} + \mathbf{A}\left(\boldsymbol{\theta}_m\right)\right]^T \mathbf{S}_{nl}^p \, d\Omega
\end{aligned}
$$

$$\tag{3.75}$$

Define $\mathbf{P}_{nl}^{p\ I}$ as follows:

$$\mathbf{P}_{nl}^{p\ I} = \left[\mathbf{H} + \mathbf{A}\left(\boldsymbol{\theta}_m\right)\right]^T \mathbf{S}_{nl}^p. \tag{3.76}$$

The nonlinear part of the PK1 stress $\mathbf{P}_{nl}^p$ is the combination of $\mathbf{P}_{nl}^{p\ I}$ and $\mathbf{P}_{nl}^{p\ II}$.

$$\mathbf{P}_{nl}^p = \mathbf{P}_{nl}^{p\ I} + \mathbf{P}_{nl}^{p\ II} \tag{3.77}$$

The first equation in Eq. (3.72) can be rewritten as below:

$$\int_{\Omega_0} \delta\boldsymbol{\theta}^T \mathbb{H}_m \boldsymbol{\theta}^p d\Omega = \lambda^p \delta\mathbf{u}^T \mathbf{f} - \delta\boldsymbol{\theta}^T \int_{\Omega_0} \mathbf{P}_{nl}^p d\Omega \tag{3.78}$$

p$^{\text{th}}$ order PK1 stress $\overleftarrow{\mathbf{P}}^p$ can be rewritten as:

$$\mathbf{P}^p = \mathbb{H}_m \boldsymbol{\theta}^p + \mathbf{P}_{nl}^p, \tag{3.79}$$

and its tensor form can be written as:

$$\overleftarrow{\mathbf{P}}^p = \mathscr{H}_m : \overline{\boldsymbol{\theta}}^p + \overleftarrow{\mathbf{P}}_{nl}^p. \tag{3.80}$$

Based on Eq. (3.64), a more clean form can be rewritten for $\overleftarrow{\mathbf{P}}_{nl}^p$:

$$\overleftarrow{\mathbf{P}}_{nl}^p = \overleftarrow{\mathbf{F}}_m \cdot \overleftarrow{\mathbf{S}}_{nl}^p + \sum_{r=1}^{p-1} \mathbf{F}^{p-r} \cdot \mathbf{S}^r \tag{3.81}$$

The first and second term in Eq. (3.81) is the tensor form for $\mathbf{P}_{nl}^{p\ I}$ and $\mathbf{P}_{nl}^{p\ II}$, respectively. In Eq. (3.81), $\overleftarrow{\mathbf{S}}_{nl}^p$ is

$$\overleftarrow{\mathbf{S}}_{nl}^p = \frac{1}{2} \sum_{r=1}^{p-1} \mathbb{C} : \left(\overline{\mathbf{F}}^{p-r\ T} \cdot \overline{\mathbf{F}}^r\right) \tag{3.82}$$

Eq. (3.82) is the tensor form of Eq. (3.73).

3.3.3 CUF-ANM Coupling

As mentioned in Subsection 3.2.1, the following relationship is derived within the CUF framework:

$$\begin{matrix} \mathbf{u}^p = F_\tau N_i \mathbf{q}_{\tau i}^p & \delta\mathbf{u}^p = F_\tau N_i \delta\mathbf{q}_{\tau i}^p, \\ \boldsymbol{\theta}^p = G_{\tau i} \mathbf{q}_{\tau i}^p & \delta\boldsymbol{\theta}^p = G_{\tau i} \delta\mathbf{q}_{\tau i}^p \end{matrix} . \tag{3.83}$$

For the 1$^{\text{st}}$ order, by using Eq. (3.49) and Eq. (3.50), the equilibrium equation can be rewritten as follows:

$$\sum_{e=1}^{Ne} \delta\mathbf{q}_{\tau i}^{e\ T} \left[\left(K_{\tau\kappa ij}^e\right) \mathbf{q}_{\kappa j}^{1e} - \lambda^1 N_i^T F_\tau^T \mathbf{f}^e\right] = 0. \tag{3.84}$$

Eq. (3.78) can be discretised in the same manner:

$$\sum_{e=1}^{Ne} \delta \mathbf{q}_{\tau i}^{e\ T} \left[\left(K_{\tau \kappa i j}^{e} \right) \mathbf{q}_{\kappa j}^{p\ e} - \lambda^{p} N_{i}^{T} F_{\tau}^{T} \mathbf{f}^{e} - \mathbf{f}_{nl\,\tau i}^{p\ e} \right] = 0. \tag{3.85}$$

The p$^{\text{th}}$ order nonlinear force $\mathbf{f}_{nl\tau i}^{pe}$ is:

$$\mathbf{f}_{nl\,\tau i}^{p\ e} = -G_{\tau i} \int_{\Omega_{0}^{e}} \mathbf{P}_{nl}^{p} d\Omega. \tag{3.86}$$

Chapter 4

Multi-scale Nonlinear Models for Beam Structures

The first part of this chapter is about the macro-scale problem, the mesoscale problem, and the coupling of these two scales. The second part deals with the solution process under the ANM solver framework. The proposed approach is separated into four steps: perturbation, localisation, homogenisation, and discretisation.

4.1 Multi-scale Problem

4.1.1 Macroscale Problem

Preliminaries. A beam structure is considered at the macroscale. To distinguish the macroscopic model from the microscopic one, the quantities belonging to the macroscale are all addressed by an overlined symbol. For the sake of clarity, some equations presented in the previous chapter are here recalled. Macroscopic Green-Lagrange strain tensor is defined as:

$$\overline{\mathbf{E}} = \overline{\mathbf{E}}^l + \overline{\mathbf{E}}^{nl} = \mathbf{H}\overline{\theta}(\overline{\mathbf{u}}) + \frac{1}{2}\overline{\mathbf{A}}\left(\overline{\theta}(\overline{\mathbf{u}})\right)\overline{\theta}(\overline{\mathbf{u}}). \tag{4.1}$$

The weak form of the governing equation is derived as:

$$\delta\overline{\mathscr{L}} = \delta\overline{\mathscr{L}}_{int} - \delta\overline{\mathscr{L}}_{ext} = 0. \tag{4.2}$$

where $\overline{\mathscr{L}}$ is the total work, and $\overline{\mathscr{L}}_{int}$ the internal one:

$$\delta\overline{\mathscr{L}}_{int} = \int_{\Omega_0} \delta\overline{\mathbf{F}}^T\overline{\mathbf{P}}d\Omega = \int_{\Omega_0} \delta\overline{\mathbf{E}}^T\overline{\mathbf{S}}d\Omega \tag{4.3}$$

Ω_0 is the volume of the reference undeformed configuration since a total Lagrangian formulation is considered. $\overline{\mathscr{L}}_{ext}$ is the work done by external forces.

$$\delta\overline{\mathscr{L}}_{ext} = \lambda\delta\overline{\mathbf{u}}^T\overline{\mathbf{f}} \tag{4.4}$$

where $\lambda \overline{\mathbf{f}}$ is the applied external force. It should be noted (as it will appear clear later). λ is not overlined because the load proportional parameter is shared by the macroscopic and microscopic problems. The governing equation becomes:

$$\delta \overline{\mathscr{L}} = \int_{\Omega_0} \delta \overline{\mathbf{E}}^T \overline{\mathbf{S}} d\Omega - \lambda \delta \overline{\mathbf{u}}^T \overline{\mathbf{f}} \tag{4.5}$$

Hierarchical Beam Elements. According to CUF, the macroscopic displacement field is a-priori assumed over the thickness as follows:

$$\overline{\mathbf{u}}\left(\overline{x}, \overline{z}\right) = \overline{F}_\tau\left(\overline{z}\right) \overline{\mathbf{u}}_\tau\left(\overline{x}\right) \ \tau = 1,\, 2,\, \ldots,\, \overline{N}_u. \tag{4.6}$$

In the case of MacLaurin's polynomials (as used in this work), the explicit form of a generic N-order displacement field reads:

$$\begin{aligned}
\overline{u}_{\overline{x}} &= \overline{u}_{\overline{x}1} + \overline{u}_{\overline{x}2}\overline{z} + \cdots + \overline{u}_{\overline{x}(N+1)}\overline{z}^N, \\
\overline{u}_{\overline{z}} &= \overline{u}_{\overline{z}1} + \overline{u}_{\overline{z}2}\overline{z} + \cdots + \overline{u}_{\overline{z}(N+1)}\overline{z}^N.
\end{aligned} \tag{4.7}$$

Concerning the displacements variation along the axial direction, a one-dimensional finite element approximation is applied as:

$$\overline{\mathbf{u}}\left(\overline{x}, \overline{z}\right) = \overline{F}_\tau\left(\overline{z}\right) \overline{N}_i\left(\overline{x}\right) \overline{\mathbf{q}}_{\tau i}\ \tau = 1,\, 2,\, \ldots,\, \overline{N}_u\ i = 1,\, 2,\, \ldots,\, \overline{N}_n^e. \tag{4.8}$$

The displacements gradient vector in the framework of CUF reads:

$$\overline{\theta} = \left\{ \begin{array}{cccc} \overline{F}_\tau \overline{N}_{i,\overline{x}} \overline{\mathbf{q}}_{\tau i}^u & \overline{F}_{\tau,\overline{z}} \overline{N}_i \overline{\mathbf{q}}_{\tau i}^u & \overline{F}_\tau \overline{N}_{i,\overline{x}} \overline{\mathbf{q}}_{\tau i}^w & \overline{F}_{\tau,\overline{z}} \overline{N}_i \overline{\mathbf{q}}_{\tau i}^w \end{array} \right\} = \overline{\mathbf{G}}_{\tau i} \overline{\mathbf{q}}_{\tau i} \tag{4.9}$$

where $\overline{\mathbf{G}}_{\tau i} \in \mathbb{R}^{4 \times 2}$ is:

$$\overline{\mathbf{G}}_{\tau i} = \begin{bmatrix} \overline{F}_\tau \overline{N}_{i,\overline{x}} & 0 \\ \overline{F}_{\tau,\overline{z}} \overline{N}_i & 0 \\ 0 & \overline{F}_\tau \overline{N}_{i,\overline{x}} \\ 0 & \overline{F}_{\tau,\overline{z}} \overline{N}_i \end{bmatrix}. \tag{4.10}$$

and $\overline{\mathbf{q}}_{\tau i} \in \mathbb{R}^{2 \times 1}$ is:

$$\overline{\mathbf{q}}_{\tau i}^T = \left\{ \begin{array}{cc} \overline{q}_{\tau i}^u & \overline{q}_{\tau i}^w \end{array} \right\}. \tag{4.11}$$

4.1.2 Microscale Problem

Without loss of generality, the considered heterogeneous material is supposed to have a periodic microstructure. A RVE occupies a domain ω_0 with frontier $\partial\omega_0$ in its reference configuration. No external forces are present on the frontier:

$$\mathbf{f} = \mathbf{0}, \text{ on } \partial\omega_0. \tag{4.12}$$

Periodic displacement boundary conditions are applied to the RVE frontier (see Barbero [9]).

The equilibrium governing equation can be written as:

$$\delta\mathscr{L} = \int_{\omega_0} \delta\mathbf{F}^T\mathbf{P}d\omega = \int_{\omega_0} \delta\mathbf{E}^T\mathbf{S}\,d\omega = 0. \tag{4.13}$$

It is assumed that the law of behaviour is known at every stage of the RVE. Hooke's law reads:

$$\mathbf{S} = \mathbb{C}^{(r)}\mathbf{E}, \tag{4.14}$$

where $\mathbb{C}^{(r)}$ is the constitutive material stiffness matrix for the material phase r. The problem at the microscopic level can be written as:

$$\begin{aligned} &\int_{\omega_0} \delta\theta^T[\mathbf{H} + \mathbf{A}\,(\theta)]^T\mathbf{S}d\omega = 0 \\ &\mathbf{S} = \mathbb{C}^{(r)}\mathbf{E} \\ &\mathbf{E} = \left(\mathbf{H} + \frac{1}{2}\mathbf{A}\theta\right)\theta \qquad \text{in } \omega_0. \\ &\theta = \nabla\mathbf{u} \end{aligned} \tag{4.15}$$

In the RVE, Hook's law is known for each phase.

4.1.3 Coupling between Scales

The first coupling relationship is based on the fact that the macroscopic deformation gradient $\bar{\bar{\mathbf{F}}}$ is equal to the volume average of the microscopic deformation gradient $\bar{\mathbf{F}}$:

$$\bar{\bar{\mathbf{F}}} = \frac{1}{|\omega_0|}\int_{\omega_0}\bar{\mathbf{F}}d\omega. \tag{4.16}$$

$|\omega_0|$ is the volume of the RVE. Eq. (4.16) can be written in a vector form:

$$\bar{\mathbf{F}} = \frac{1}{|\omega_0|}\int_{\omega_0}\mathbf{F}d\omega. \tag{4.17}$$

The current microscopic position vector $\mathbf{x} \in \mathbb{R}^2$ is considered to be the sum of a slowly varying mean field and a perturbation field $\mathbf{w}(\mathbf{X}) \in \mathbb{R}^2$ caused by heterogeneity as below, where $\mathbf{X} \in \mathbb{R}^2$ is the coordinate in the reference configuration.

$$\mathbf{x} = \bar{\bar{\mathbf{F}}}\cdot\mathbf{X} + \mathbf{w}(\mathbf{X}) \tag{4.18}$$

The previous equation when differentiated by $\mathbf{X}$ reads:

$$\overleftarrow{\mathbf{F}} = \bar{\bar{\mathbf{F}}} + \mathbf{w}_{,\mathbf{X}}(\mathbf{X}). \tag{4.19}$$

The microscopic displacement field is obtained by subtracting $\mathbf{X}$ from the previous equation:

$$\mathbf{u} = (\overline{\overline{\mathbf{F}}} - \mathbf{I})\mathbf{X} + \mathbf{w}(\mathbf{X}) = \overline{\overline{\theta}}\mathbf{X} + \mathbf{w}(\mathbf{X}). \tag{4.20}$$

The same displacement conditions are applied to two pairs of opposite edges ($\partial w_0^{i-} \cup \partial w_0^{i+}$, $i = x, z$). Based on Eq. (4.20), the microscopic displacement field yields:

$$\begin{aligned}
\mathbf{u}(\mathbf{X}^+) &= \overline{\overline{\theta}}\mathbf{X}^+ + \mathbf{w}(\mathbf{X}^+), \\
\mathbf{u}(\mathbf{X}^-) &= \overline{\overline{\theta}}\mathbf{X}^- + \mathbf{w}(\mathbf{X}^-).
\end{aligned} \tag{4.21}$$

Consequently, the following equation can be obtained:

$$\mathbf{u}(\mathbf{X}^+) - \mathbf{u}(\mathbf{X}^-) = \overline{\overline{\theta}}(\mathbf{X}^+ - \mathbf{X}^-) + (\mathbf{w}(\mathbf{X}^+) - \mathbf{w}(\mathbf{X}^-)). \tag{4.22}$$

Then, the boundary condition for the RVE can be derived as:

$$\mathbf{u}(\mathbf{X}^+) - \mathbf{u}(\mathbf{X}^-) = \overline{\overline{\theta}}(\mathbf{X}^+ - \mathbf{X}^-), \text{ for } [(\mathbf{X}^- \in \partial w_0^{i-}) \cup (\mathbf{X}^+ \in \partial w_0^{i+})], \ i = x, z. \tag{4.23}$$

By introducing Eq. (4.19), Eq. (4.16) :

$$\overline{\overline{\mathbf{F}}} = \frac{1}{|\omega_0|} \int_{\omega_0} \overleftarrow{\mathbf{F}} d\omega + \frac{1}{|\omega_0|} \int_{\omega_0} \mathbf{w}_{,\mathbf{X}}(\mathbf{X}) d\omega = \overline{\overline{\mathbf{F}}} + \frac{1}{|\omega_0|} \int_{\omega_0} \mathbf{w}_{,\mathbf{X}}(\mathbf{X}) d\omega, \tag{4.24}$$

which leads to the following relation:

$$\frac{1}{|\omega_0|} \int_{\omega_0} \mathbf{w}_{,\mathbf{X}}(\mathbf{X}) d\omega = 0. \tag{4.25}$$

Using Green's theorem, the previous equation becomes:

$$\frac{1}{|\omega_0|} \int_{\omega_0} \mathbf{w}_{,\mathbf{X}}(\mathbf{X}) d\omega = \frac{1}{|\omega_0|} \int_{\Gamma} \mathbf{w}(\mathbf{X})\mathbf{n} d\Gamma = 0. \tag{4.26}$$

where Γ is the RVE boundary on two opposite sides. Here $\mathbf{n}$ is used to represent the unit normal vector perpendicular to the RVE boundary, see Fig 4.1. The microscale boundary condition, then, is:

$$\mathbf{w}(\mathbf{X}) = 0, \text{ for } \mathbf{X} \in (\partial w_0^{i-} \cup \partial w_0^{i+}), \ i = x, z \tag{4.27}$$

or

$$\mathbf{w}(\mathbf{X}^+) = \mathbf{w}(\mathbf{X}^-), \text{ for } [(\mathbf{X}^- \in \partial w_0^{i-}) \cup (\mathbf{X}^+ \in \partial w_0^{i+})], \ i = x, z. \tag{4.28}$$

Eq. (4.28) indicates that the perturbation needs to have periodicity on the boundary, and the boundary can be considered as the union of the subsets $\partial\omega_0^+$ and $\partial\omega_0^-$ ($\partial\omega_0 = \partial\omega_0^+ \cup \partial\omega_0^-$). As shown in Fig 4.1, the corresponding normal vectors are $\mathbf{n}^+$ and $\mathbf{n}^-$ ($\mathbf{n}^+ = -\mathbf{n}^-$), and a corresponding set of two generic points are $\mathbf{X}^+ \in \partial\omega_0^+$ and $\mathbf{X}^- \in$
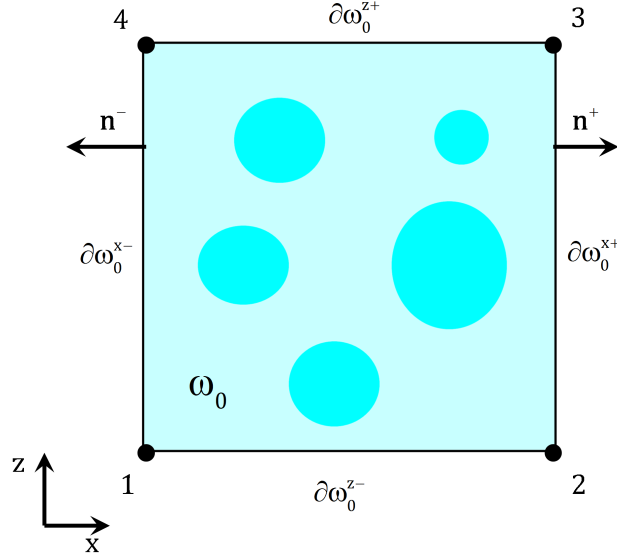
$\partial\omega_0^-$.

Figure 4.1: RVE configuration.

The second coupling relationship concerns the first Piola-Kirkhhoff stress at macro and micro scales:

$$\overline{\mathbf{P}} = \frac{1}{|\omega_0|} \int_{\omega_0} \mathbf{P}d\omega. \tag{4.29}$$

The third coupling equation is the Hill-Mandel condition. The average of the variation of the work done in the RVE is equal to an inifitesimal virtual variation of the work at the macroscale:

$$\delta\overline{\mathbf{F}}^T\overline{\mathbf{P}} = \delta\overline{\mathbf{E}}^T\overline{\mathbf{S}} = \int_{\omega_0} \delta\mathbf{F}^T\mathbf{P}d\omega = \int_{\omega_0} \delta\mathbf{E}^T\mathbf{S}\,d\omega. \tag{4.30}$$

4.2 Multi-Scale problem in the ANM framework

4.2.1 Perturbation Technique

For macroscopic and microscopic scales, all the variables $\left[(\overline{\mathbf{u}}, \overline{\boldsymbol{\theta}}, \overline{\mathbf{E}}, \overline{\mathbf{S}}), (\mathbf{u}, \boldsymbol{\theta}, \mathbf{E}, \mathbf{S}), \lambda\right]$ are expanded into power series:

$$
\begin{aligned}
\overline{\mathbf{u}} &: \overline{\mathbf{u}}_{m+1} = \overline{\mathbf{u}}_m + a^p \overline{\mathbf{u}}^p & \mathbf{u} &: \mathbf{u}_{m+1} = \mathbf{u}_m + a^p \mathbf{u}^p \\
\overline{\mathbf{E}} &: \overline{\mathbf{E}}_{m+1} = \overline{\mathbf{E}}_m + a^p \overline{\mathbf{E}}^p & \mathbf{E} &: \mathbf{E}_{m+1} = \mathbf{E}_m + a^p \mathbf{E}^p \quad p = 1, 2, ..., N_{max}. \\
\overline{\mathbf{S}} &: \overline{\mathbf{S}}_{m+1} = \overline{\mathbf{S}}_m + a^p \overline{\mathbf{S}}^p & \mathbf{S} &: \mathbf{S}_{m+1} = \mathbf{S}_m + a^p \mathbf{S}^p \\
& & \lambda &: \lambda_{m+1} = \lambda_m + a^p \lambda^p
\end{aligned}
\tag{4.31}
$$

Perturbation at the Macroscale. Macroscopic problems are defined by Eq. (4.5), whose variables are $(\overline{\mathbf{u}}, \overline{\theta}, \overline{\mathbf{E}}, \overline{\mathbf{S}}, \lambda)$. Similarly to what done in Chapter 3, a system of equation for the first-order an the generic p^{th}-order are derived:

- 1st order:

$$
\int_{\Omega_0} \delta \overline{\theta}^T \overline{\mathbb{H}}_m \overline{\theta}^1 d\Omega = \lambda^1 \delta \overline{\mathbf{u}}^T \mathbf{f}
\tag{4.32}
$$

- p^{th} order:

$$
\int_{\Omega_0} \delta \overline{\theta}^T \overline{\mathbb{H}}_m \overline{\theta}^p d\Omega = \lambda^p \delta \overline{\mathbf{u}}^T \mathbf{f} - \delta \overline{\theta}^T \int_{\Omega_0} \overline{\mathbf{P}}_{nl}^p d\Omega
\tag{4.33}
$$

To be noticed, $\overline{\mathbb{H}}_m$ is not yet known.

Perturbation at the Microscale. The microscopic problem is defined by Eq. (4.15) and Eq. (4.23), whose variables are $(\mathbf{u}, \theta, \mathbf{E}, \mathbf{S})$. The following linear problems can be derived for each order:

- 1st order:

$$
\begin{aligned}
& \int_{\omega_0} \delta \theta^T \mathbb{H}_m \theta^1 d\omega = 0 \\
& \mathbf{S}^1 = \mathbb{C}^{(r)} \left[\mathbf{H} + \mathbf{A} \left(\theta_m \right) \right] \theta^1 \quad \text{in } \omega_0, \\
& \theta^1 = \nabla \mathbf{u}^1
\end{aligned}
\tag{4.34}
$$

$$
\mathbf{u}^{1(+)} - \mathbf{u}^{1(-)} = \overset{\leftharpoonup 1}{\theta} (\mathbf{X}^+ - \mathbf{X}^-) \text{ for } [(\mathbf{X}^- \in \partial w_0^{i-}) \cup (\mathbf{X}^+ \in \partial w_0^{i+})], \ i = x, z.
\tag{4.35}
$$

- p^{th} order:

$$
\begin{aligned}
& \int_{\omega_0} \delta \theta^T \mathbb{H}_m \theta^p d\omega = -\delta \theta^T \int_{\Omega_0} \mathbf{P}_{nl}^p d\omega \\
& \mathbf{S}^p = \mathbb{C}^{(r)} \left[\mathbf{H} + \mathbf{A} \left(\theta_m \right) \right] \theta^p \quad \text{in } \omega_0, \\
& \theta^p = \nabla \mathbf{u}^p
\end{aligned}
\tag{4.36}
$$

$$
\mathbf{u}^{p(+)} - \mathbf{u}^{p(-)} = \overset{\leftharpoonup p}{\theta} (\mathbf{X}^+ - \mathbf{X}^-) \text{ for } [(\mathbf{X}^- \in \partial w_0^{i-}) \cup (\mathbf{X}^+ \in \partial w_0^{i+})], \ i = x, z.
\tag{4.37}
$$

The nonlinear part of PK1 stress $\mathbf{P}_{nl}^p$ is calculated from the solutions obtained with the previous orders.

4.2.2   Localisation

For coupling the macroscopic and the microscopic problems, the starting point is the solution of the RVE's linear problems at each order. The superposition principle is applied to Eq. (4.34) and Eq. (4.36).
Consider the problem at the 1st order in Eq. (4.34). The 1st order solution $\mathbf{u}^1$ can be written as a linear combination of the axial and shear deformations. These displacements are derived by independently imposing the homogeneous deformation fields via the boundary conditions in Eq. (4.35):

$$\mathbf{u}^1 = \overline{\theta}^{1(11)}\widetilde{\mathbf{u}}^{(11)} + \overline{\theta}^{1(12)}\widetilde{\mathbf{u}}^{(12)} + \overline{\theta}^{1(21)}\widetilde{\mathbf{u}}^{(21)} + \overline{\theta}^{1(22)}\widetilde{\mathbf{u}}^{(22)}. \tag{4.38}$$

where $\widetilde{\mathbf{u}}^{(ij)}$ $(i, j = 1,2)$ are obtained by solving the following problem:

$$\begin{aligned}&\int_{\omega_0} \delta\theta^T \mathbb{H}_m \theta(\widetilde{\mathbf{u}}^{(ij)})d\omega = 0 \\ &\widetilde{\mathbf{u}}^{(ij)+} - \widetilde{\mathbf{u}}^{(ij)-} = \mathbf{X}^{(ij)+} - \mathbf{X}^{(ij)-}, on\ \partial\omega_0\end{aligned} \tag{4.39}$$

with:

$$\begin{aligned}\mathbf{X}^{(11)+} - \mathbf{X}^{(11)-} &= \begin{bmatrix} 1 & 0 \\ 0 & 0 \end{bmatrix}(\mathbf{X}^+ - \mathbf{X}^-),\ \mathbf{X}^{(12)+} - \mathbf{X}^{(12)-} = \begin{bmatrix} 0 & 1 \\ 0 & 0 \end{bmatrix}(\mathbf{X}^+ - \mathbf{X}^-) \\ \mathbf{X}^{(21)+} - \mathbf{X}^{(21)-} &= \begin{bmatrix} 0 & 0 \\ 1 & 0 \end{bmatrix}(\mathbf{X}^+ - \mathbf{X}^-),\ \mathbf{X}^{(22)+} - \mathbf{X}^{(22)-} = \begin{bmatrix} 0 & 0 \\ 0 & 1 \end{bmatrix}(\mathbf{X}^+ - \mathbf{X}^-)\end{aligned}. \tag{4.40}$$

The problem in Eq. (4.38) is written in a compact form by introducing the third-order tensor $\mathscr{A}$:

$$\mathbf{u}^1(\mathbf{X}) = \mathscr{A}(\mathbf{X}) : \overset{\Leftarrow 1}{\theta}. \tag{4.41}$$

By differentiating Eq. (4.41) by $\mathbf{X}$, the following relation is obtained:

$$\overline{\theta}^1 = \mathscr{A}_{,\mathbf{X}}(\mathbf{X}) : \overset{\Leftarrow 1}{\theta}. \tag{4.42}$$

Tensor $\mathscr{A}$ in a matrix form reads:

$$\mathbb{A} = \begin{bmatrix} \mathbb{A}^{(11)} & \mathbb{A}^{(12)} & \mathbb{A}^{(21)} & \mathbb{A}^{(22)} \end{bmatrix} = \begin{bmatrix} \widetilde{\mathbf{u}}^{(11)} & \widetilde{\mathbf{u}}^{(12)} & \widetilde{\mathbf{u}}^{(21)} & \widetilde{\mathbf{u}}^{(22)} \end{bmatrix}. \tag{4.43}$$

As for the $\mathbb{A}_{,\mathbf{X}} \in \mathbb{R}^{4 \times 4}$, it can be written as follows:

$$
\begin{aligned}
\mathbb{A}_{,\mathbf{X}} &= \left[\begin{array}{cccc}
\mathbb{A}_{,\mathbf{X}_{11}} & \mathbb{A}_{,\mathbf{X}_{12}} & \mathbb{A}_{,\mathbf{X}_{13}} & \mathbb{A}_{,\mathbf{X}_{14}} \\
\mathbb{A}_{,\mathbf{X}_{21}} & \mathbb{A}_{,\mathbf{X}_{22}} & \mathbb{A}_{,\mathbf{X}_{23}} & \mathbb{A}_{,\mathbf{X}_{24}} \\
\mathbb{A}_{,\mathbf{X}_{31}} & \mathbb{A}_{,\mathbf{X}_{32}} & \mathbb{A}_{,\mathbf{X}_{33}} & \mathbb{A}_{,\mathbf{X}_{34}} \\
\mathbb{A}_{,\mathbf{X}_{41}} & \mathbb{A}_{,\mathbf{X}_{42}} & \mathbb{A}_{,\mathbf{X}_{43}} & \mathbb{A}_{,\mathbf{X}_{44}}
\end{array} \right] \\
&= \left[\begin{array}{cccc}
\tilde{u}_{x,x}^{(11)} & \tilde{u}_{x,x}^{(12)} & \tilde{u}_{x,x}^{(21)} & \tilde{u}_{x,x}^{(22)} \\
\tilde{u}_{x,z}^{(11)} & \tilde{u}_{x,z}^{(12)} & \tilde{u}_{x,z}^{(21)} & \tilde{u}_{x,z}^{(22)} \\
\tilde{u}_{z,x}^{(11)} & \tilde{u}_{z,x}^{(12)} & \tilde{u}_{z,x}^{(21)} & \tilde{u}_{z,x}^{(22)} \\
\tilde{u}_{z,z}^{(11)} & \tilde{u}_{z,z}^{(12)} & \tilde{u}_{z,z}^{(21)} & \tilde{u}_{z,z}^{(22)}
\end{array} \right].
\end{aligned}
\tag{4.44}
$$

Then, Eq. (4.42) can be rewritten as:

$$
\boldsymbol{\theta}^1 = \mathbb{A}_{,\mathbf{X}}(\mathbf{X}) \overline{\boldsymbol{\theta}}^1,
\tag{4.45}
$$

which is the final form of the first-order localisation equation. For a pth order, $\mathbf{u}^p$ can be decomposed as:

$$
\mathbf{u}^p = \mathbf{u}_l^p + \mathbf{u}_{nl}^p.
\tag{4.46}
$$

The first term can be rewritten as:

$$
\mathbf{u}_l^p = \overline{\theta}^{p(11)} \widetilde{\mathbf{u}}^{(11)} + \overline{\theta}^{p(12)} \widetilde{\mathbf{u}}^{(12)} + \overline{\theta}^{p(21)} \widetilde{\mathbf{u}}^{(21)} + \overline{\theta}^{p(22)} \widetilde{\mathbf{u}}^{(22)},
\tag{4.47}
$$

where $\widetilde{\mathbf{u}}^{(ij)}$ are obtained by the solution of the first-order problem in Eq. (4.39). The nonlinear displacement part $\mathbf{u}_{nl}^p$ results from the following problem:

$$
\int_{\omega_0} \delta \boldsymbol{\theta}^T \mathbb{H}_m \boldsymbol{\theta}^p d\omega = - \int_{\omega_0} \delta \boldsymbol{\theta}^T \mathbf{P}_{nl}^p d\omega \text{ in } \omega_0.
\tag{4.48}
$$

Considering Eq. (4.41) and Eq. (4.46), the pth order displacement becomes:

$$
\mathbf{u}^p(\mathbf{X}) = \mathscr{A}(\mathbf{X}) : \overleftarrow{\boldsymbol{\theta}}^p + \mathbf{u}_{nl}^p.
\tag{4.49}
$$

When differentiating versus $\mathbf{X}$, the previous equation reads:

$$
\overline{\boldsymbol{\theta}}^p = \mathscr{A}_{,\mathbf{X}}(\mathbf{X}) : \overleftarrow{\boldsymbol{\theta}}^p + \overline{\mathbf{u}}_{nl,\mathbf{X}}^p
\tag{4.50}
$$

where $\overline{\mathbf{u}}_{nl,\mathbf{X}}^p \in \mathbb{R}^{2 \times 2}$ is a second-order tensor. It has a corresponding vector form $\mathbf{u}_{nl,\mathbf{X}}^p \in \mathbb{R}^4$. Eq. (4.50) in a vector form can be rewritten as:

$$
\boldsymbol{\theta}^p = \mathbb{A}_{,\mathbf{X}}(\mathbf{X}) \overline{\boldsymbol{\theta}}^p + \mathbf{u}_{nl,\mathbf{X}}^p.
\tag{4.51}
$$

4.2.3 Homogenisation

Eq. (3.70) and Eq. (3.79) are written also at the microscale::

$$\mathbf{P}^p = \mathbb{H}_m^{(r)}\theta^p + \mathbf{P}_{nl}^p. \tag{4.52}$$

where it is here assumed that p is also equal to one (in this case P_{nl}^p is equal to zero). By introducing Eq. (4.51), Eq. (4.52) can be rewritten as:

$$\mathbf{P}^p = \mathbb{H}_m^{(r)}\left(\mathbb{A}_{,\mathbf{X}}(\mathbf{X})\overline{\theta}^p + \mathbf{u}_{nl,\mathbf{X}}^p\right) + \mathbf{P}_{nl}^p = \mathbb{H}_m^{(r)}\mathbb{A}_{,\mathbf{X}}(\mathbf{X})\overline{\theta}^p + \mathbb{H}_m^{(r)}\mathbf{u}_{nl,\mathbf{X}}^p + \mathbf{P}_{nl}^p. \tag{4.53}$$

Tensor $\mathbb{L}_m$ is defined as:

$$\mathbb{L}_m = \mathbb{H}_m^{(r)}\mathbb{A}_{,x}. \tag{4.54}$$

and $\mathbf{P}_{*nl}^p$ as:

$$\mathbf{P}_{*nl}^p = \mathbb{H}_m^{(r)}\mathbf{u}_{nl,\mathbf{X}}^p + \mathbf{P}_{nl}^p. \tag{4.55}$$

Eq. (4.53) can be rewritten as:

$$\mathbf{P}^p = \mathbb{L}_m\overline{\theta}^p + \mathbf{P}_{*nl}^p. \tag{4.56}$$

Based on the first and second coupling relationships in Eq. (4.17) and Eq. (4.29), the following equations can be derived:

$$\overline{\theta}^p = \frac{1}{|\omega_0|}\int_{\omega_0}\theta^p d\omega \tag{4.57}$$

$$\overline{\mathbf{P}}^p = \frac{1}{|\omega_0|}\int_{\omega_0}\left(\mathbb{L}_m\theta^p + \mathbf{P}_{nl}^p\right)d\omega. \tag{4.58}$$

Two additional macroscopic terms are defined by:

$$\overline{\mathbb{L}}_m = \frac{1}{|\omega_0|}\int_{\omega_0}\mathbb{L}_m d\omega \tag{4.59}$$

and

$$\overline{\mathbf{P}}_{nl}^p = \frac{1}{|\omega_0|}\int_{\omega_0}\mathbf{P}_{*nl}^p d\omega. \tag{4.60}$$

Consequently, the macroscopic PK1 stress is obtained as:

$$\overline{\mathbf{P}}^p = \overline{\mathbb{L}}_m\overline{\theta}^p + \overline{\mathbf{P}}_{nl}^p, \tag{4.61}$$

which is an analogous form as shown in Eq. (4.56).
By replacing the unknown $\overline{\mathbb{H}}_m$ in Eq. (4.32) and Eq. (4.33), the following macroscopic equations can be derived:

- 1st order:

$$\int_{\Omega_0} \delta\overline{\boldsymbol{\theta}}^T \overline{\mathbb{L}}_m \overline{\boldsymbol{\theta}}^1 d\Omega = \lambda^1 \delta\overline{\mathbf{u}}^T \mathbf{f} \tag{4.62}$$

- pth order:

$$\int_{\Omega_0} \delta\overline{\boldsymbol{\theta}}^T \overline{\mathbb{L}}_m \overline{\boldsymbol{\theta}}^p d\Omega = \lambda^p \delta\overline{\mathbf{u}}^T \mathbf{f} - \delta\overline{\boldsymbol{\theta}}^T \int_{\Omega_0} \overline{\mathbf{P}}_{nl}^p d\Omega. \tag{4.63}$$

4.2.4 CUF-ANM Multiscale Solution

Macroscale problem. The whole macroscopic domain is discretised using CUF hierarchical beam elements. Besides, substituting $\overline{\boldsymbol{\theta}}(\overline{\mathbf{u}})$ in Eq. (4.9), Eq. (4.62) can be rewritten as:

$$\sum_{e=1}^{Ne} \int_{\Omega_0^e} \delta\overline{\boldsymbol{\theta}}^{eT} \overline{\mathbb{L}}_m^e \overline{\boldsymbol{\theta}}^{1e} d\Omega = \sum_{e=1}^{Ne} \lambda^1 \delta\overline{\mathbf{u}}^{eT} \overline{\mathbf{f}}^e. \tag{4.64}$$

For one element, Eq (4.64) becomes:

$$
\begin{aligned}
\int_{\Omega_0^e} \delta\overline{\boldsymbol{\theta}}^{eT} \overline{\mathbb{L}}_m^e \overline{\boldsymbol{\theta}}^{1e} d\Omega &= \delta\overline{\mathbf{q}}_{\tau i}^{eT} \int_{\Omega_0^e} \overline{\mathbf{G}}_{\tau i}^{eT} \overline{\mathbb{L}}^e \overline{\mathbf{G}}_{\kappa j}^e d\Omega \overline{\mathbf{q}}_{\kappa j}^e \\
&= \delta\overline{\mathbf{q}}_{\tau i}^{e\,T} \left(\overline{\mathbf{K}}_{\tau\kappa ij}^e(\overline{\boldsymbol{\theta}}_m^e) \right) \overline{\mathbf{q}}_{\kappa j}^{1e}.
\end{aligned} \tag{4.65}
$$

where $\overline{\mathbf{K}}_{\tau\kappa ij}^e$ is the multiscale fundamental nucleus of the elemental stiffness matrix. It is worth noting that the macroscopic geometric nonlinearity is accounted for within the stiffness matrix in Eq. (4.65). The nuclei are not dependent on the approximation order over the thickness ($\overline{N}_u$) nor the number of nodes per element along the beam axis ($\overline{N}_n^e$). The components of the stiffness matrix nucleus $\overline{\mathbf{K}}_{\tau\kappa ij}^e$ are:

$$
\begin{aligned}
\overline{K}_{\tau\kappa ij}^{e\overline{xx}} &= \overline{J}_{\tau\kappa i,\overline{x}j,\overline{x}}^{11} + \overline{J}_{\tau,\overline{z}\kappa,\overline{z}ij}^{22} + \overline{J}_{\tau,\overline{z}\kappa ij,\overline{x}}^{21} + \overline{J}_{\tau\kappa,\overline{z}i,\overline{x}j}^{12} \\
\overline{K}_{\tau\kappa ij}^{e\overline{xz}} &= \overline{J}_{\tau\kappa,\overline{z}i,\overline{x}j}^{14} + \overline{J}_{\tau\kappa i,x j,\overline{x}}^{13} + \overline{J}_{\tau,\overline{z}\kappa,\overline{z}ij}^{24} + \overline{J}_{\tau,\overline{z}\kappa ij,\overline{x}}^{23} \\
\overline{K}_{\tau\kappa ij}^{e\overline{zx}} &= \overline{J}_{\tau,\overline{z}\kappa ij,\overline{x}}^{41} + \overline{J}_{\tau\kappa i,\overline{x}j,\overline{x}}^{31} + \overline{J}_{\tau,\overline{z}\kappa,\overline{z}ij}^{42} + \overline{J}_{\tau\kappa,\overline{z}i,\overline{x}j}^{32} \\
\overline{K}_{\tau\kappa ij}^{e\overline{zz}} &= \overline{J}_{\tau,\overline{z}\kappa,\overline{z}ij}^{44} + \overline{J}_{\tau\kappa i,\overline{x}j,\overline{x}}^{33} + \overline{J}_{\tau\kappa,\overline{z}i,\overline{x}j}^{34} + \overline{J}_{\tau,\overline{z}\kappa ij,\overline{x}}^{43}
\end{aligned} \tag{4.66}
$$

The generic term $\overline{J}_{\tau(,\overline{z})\kappa(,\overline{z})i(,\overline{x})j(,\overline{x})}^{gh}$ is the following volume integral:

$$\overline{J}_{\tau(,\overline{z})\kappa(,\overline{z})i(,\overline{x})j(,\overline{x})}^{gh} = \int_{\overline{\square}^e = \overline{h}^e \times \overline{b}^e} \int_{\overline{l}^e} \overline{\mathbb{L}}_{gh} \overline{F}_{\tau(,\overline{z})} \overline{F}_{\kappa(,\overline{z})} \overline{N}_{i(,\overline{x})} \overline{N}_{j(,\overline{x})} \, d\overline{\square} \, d\overline{x} \,. \tag{4.67}$$

Similarly, for one element, the right side of Eq (4.64) can be written in the following form:

$$\overline{\lambda}^1 \delta \overline{\mathbf{u}}^{eT} \overline{\mathbf{f}}^e = \delta \overline{q}_{\tau i}^e{}^T \overline{\lambda}^1 \overline{N}_i{}^T \overline{F}_\tau^T \overline{\mathbf{f}}^e, \tag{4.68}$$

being $\overline{\mathbf{f}}^e$ an external force. For the p$^{\text{th}}$ order, Eq. (4.63) can be rewritten as:

$$\sum_{e=1}^{Ne} \left(\delta \overline{\mathbf{q}}_{\tau i}^e{}^T \left(\overline{\mathbf{K}}_{\tau \kappa i j}^e (\overline{\boldsymbol{\theta}}_m^e) \right) \overline{\mathbf{q}}_{\kappa j}^{p \ e} - \delta \overline{\mathbf{q}}_{\tau i}^e{}^T \lambda^p \overline{N}_i{}^T F_\tau^T \overline{\mathbf{f}}^e - \delta q_{\tau i}^e{}^T N_i{}^T F_\tau^T \overline{\mathbf{f}}_{nl\,\tau i}^{p \ e} \right) = 0. \tag{4.69}$$

where $\overline{\mathbf{f}}_{nl\,\tau i}^{p \ e}$ is:

$$\overline{\mathbf{f}}_{nl\,\tau i}^{p \ e} = -\overline{\mathbf{G}}_{\tau i} \int_{\Omega_0^e} \overline{\mathbf{P}}_{nl}^p d\Omega. \tag{4.70}$$

Microscale problem. For one element, the displacement field $\mathbf{u}$ in the domain can be discretised as classically done as:

$$\mathbf{u}^e = \mathbf{N}\mathbf{q}^e. \tag{4.71}$$

where $\mathbf{q}^e$ is the nodal displacement vector of the element, and $\mathbf{N}$ is a matrix whose components are the considered shape functions [170]. Coherently, the following equations hold:

$$\begin{aligned} \delta \mathbf{u}^e &= \mathbf{N}\delta \mathbf{q}^e, \\ \boldsymbol{\theta}^e &= \mathbf{G}\mathbf{q}^e, \\ \delta \boldsymbol{\theta}^e &= \mathbf{G}\delta \mathbf{q}^e. \end{aligned} \tag{4.72}$$

in which $\mathbf{G}$ is the shape function derivatives matrix. According to Eq. (4.72), Eq. (4.34) for a single element can be derived as follows:

$$\delta \mathbf{q}^{eT} \mathbf{G}^T \int_{\omega_0^e} \mathbb{H}_m^e \boldsymbol{\theta}^{1e} d\omega_0 = 0. \tag{4.73}$$

Substituting $\mathbb{H}_m^e$ in Eq. (3.25), it can be rewritten as:

$$\delta \mathbf{q}^{eT} \int_{\omega_0^e} \mathbf{G}^T \left[\left[\mathbf{H}^T + \mathbf{A}^T \left(\boldsymbol{\theta}_m^e \right) \right] \mathbb{C}^{(r)} \left[\mathbf{H} + \mathbf{A} \left(\boldsymbol{\theta}_m^e \right) \right] + \hat{\mathbf{S}}_m^e \right] \mathbf{G} d\omega \mathbf{q}^{1e} = 0. \tag{4.74}$$

The right-hand side of the previous equation is zero since no external force is considered at the microscale. For the sake of brevity, the following notation is introduced:

$$\begin{aligned} \mathbf{B}^l &= \mathbf{H}\mathbf{G}, \\ \mathbf{B}^{nl}(\mathbf{q}^e) &= \mathbf{A}(\boldsymbol{\theta}(\mathbf{q}^e))\mathbf{G}, \\ \mathbf{B} &= \mathbf{B}^l + \mathbf{B}^{nl}(\mathbf{q}^e). \end{aligned} \tag{4.75}$$

The elemental stiffness matrix $\mathbf{K}_m^e$ is defined as follows:

$$\mathbf{K}_m^e = \int_{\omega_0^e} \mathbf{B}^T(\mathbf{q}_m^e) \mathbb{C}^{(r)} \mathbf{B}_m(\mathbf{q}_m^e) + \mathbf{G}^T \hat{\mathbf{S}}_m^e \mathbf{G} d\omega. \tag{4.76}$$

The global tangent stiffness matrix $\mathbf{K}_m$ can be obtained by assembling the elemental stiffness matrix $\mathbf{K}_m^e$. Then, the 1st order microscopic control equation Eq. (4.34) can be rewritten as:

$$\mathbf{K}_m\mathbf{q}^1 = 0. \tag{4.77}$$

Then, the periodic boundary condition in Eq. (4.37) can be discretised for two pairs of opposite edges as:

$$\mathbf{q}^{p(+)} - \mathbf{q}^{p(-)} = \mathbb{X}\overline{\mathbf{F}}^p. \quad p = 1, ..., N_{max} \tag{4.78}$$

where

$$\mathbb{X} = \left[\begin{array}{cccc} \mathbf{X}^{(11)+} - \mathbf{X}^{(11)-} & \mathbf{X}^{(12)+} - \mathbf{X}^{(12)-} & \mathbf{X}^{(21)+} - \mathbf{X}^{(21)-} & \mathbf{X}^{(22)+} - \mathbf{X}^{(22)-} \end{array} \right]. \tag{4.79}$$

For the four vertices, the following displacement loading are applied:

$$\mathbf{q}_{(vert)}^p = \left[\begin{array}{cccc} \mathbf{X}_{(vert)}^{(11)} & \mathbf{X}_{(vert)}^{(12)} & \mathbf{X}_{(vert)}^{(21)} & \mathbf{X}_{(vert)}^{(22)} \end{array} \right]\overline{\mathbf{F}}^p \quad vert = 1, 2, 3, 4. \tag{4.80}$$

The pth order control equation Eq. (4.33) becomes:

$$\mathbf{K}_m\mathbf{q}^p = \mathbf{f}_{nl}^p.s \tag{4.81}$$

$\mathbf{f}_{nl}^p$ is assembled from $\mathbf{f}_{nl}^{pe}$, which is defined as:

$$\mathbf{f}_{nl}^{pe} = -\mathbf{G}\int_{\omega_0^e} \mathbf{P}_{nl}^p d\omega. \tag{4.82}$$

where $\mathbf{P}_{nl}^p$ is given in Eq. (3.77). The 1st order problem yields $\mathbb{A}$, and the pth order problem gives as solution $\overline{\mathbf{P}}_{nl}^p$. The control equations, therefore, are finally written as:

- 1st order:

$$\mathbf{K}_m\widetilde{\mathbf{q}}^{(ij)} = 0 \tag{4.83}$$

$$\widetilde{\mathbf{q}}^{(ij)+} - \widetilde{\mathbf{q}}^{(ij)-} = \mathbf{X}^{(ij)+} - \mathbf{X}^{(ij)-} \tag{4.84}$$

$$\widetilde{\mathbf{q}}_{(vert)}^{(ij)} = \mathbf{X}_{(vert)}^{(ij)} \quad vert = 1,2,3,4 \tag{4.85}$$

- pth order:

$$\mathbf{K}_m\mathbf{q}_{nl}^p = \mathbf{f}_{nl}^p \tag{4.86}$$

$$\mathbf{q}_{nl}^p = 0. \tag{4.87}$$

The localisation equations are discretised in a similar manner. θ^{pe} in Eq. (4.51) for each element inside the RVE can be written as:

$$\theta^{pe} = \mathbb{A}_{,\mathbf{X}}\overline{\theta}^{pe} + \mathbf{G}\mathbf{q}_{nl}^{pe}. \tag{4.88}$$

In addition, for the homogenisation equations, the nonlinear part of pth order PK1 stress in Eq (4.60) can be discretised as:

$$\mathbf{P}_{*nl}^{pe} = \mathbb{H}_m^{(r)}\mathbf{G}\mathbf{q}_{nl}^{pe} + \mathbf{P}_{nl}^{pe}. \tag{4.89}$$

Chapter 5

Geometrically Nonlinear Analysis of Beam Structures

In this chapter, numerical investigations are conducted by using the beam model proposed in Chapter 3. In particular, the following four cases are presented. First, computational efficiencies are compared by the following two aspects: the number of DOFs of the structural model and the time cost required of the nonlinear solver to converge. Secondly, nonlinear static analyses are carried out with a convergence analysis in the beginning. This analysis focuses on the convergence speed of the displacement results. The displacement results come from two models, one using the MITC element and the other using the standard finite element. Then, two static nonlinear analyses for long and short clamped-hinged beams are presented. The length-to-thickness ratio (l/h) of long and short beams is 100 and 10, respectively. Finally, post- analyses concerning a clamped-hinged beam and a simply-supported beam are shown, where the length-to-fine ratio are both 20. Finally, a snap-through analysis of a simply-supported beam with a slenderness ratio of 20 is demonstrated.

5.1   Computational Time and Cost Assessment

In this section, the following two assessments are presented: 1. the DOF reduction of the proposed CUF models versus reference two-dimensional FEM solution and 2. the CPU time cost reduction when using ANM in place of NRM (the same CUF model is employed in both cases). All the presented cases have the same gemetrical and material properties. The cross-section thickness h and width b are equal to 1 m. Material properties are: $E = 75$ GPa, and $\nu = 0.33$ (aluminium). The following dimensionless force $\lambda = fl^2/EI$ is employed, being I the moment of inertia of the beam cross-section and f the applied force.. Both displacement and stress values are given in the initial fixed coordinate system.

DOFs Comparison. Results are compared with two-dimensional finite element solutions computed through the commercial code ANSYS. ANSYS finite elements "Plane183" is utilised to verify the convergence of the reference solution. This element is a two-dimensional eight-node element with nonlinear strain based on an Updated Lagrangian formulation. An accuracy up to four significant digits is sought for all the considered results. For slender beams, a refined mesh is 240×24 and a coarse one 160×16 are used. Regarding short beams, the refined mesh 80×8, whereas the coarse one is 32×8. Ne_x and Ne_z represent the number of elements along the beam axis and the thickness, respectively.

As concerns the computational cost, the degrees of freedom (DOF) for the two-dimensional finite element model as a function of Ne_x, Ne_z are:

$$DOF_{FEM} = 2(3Ne_x Ne_z + 2Ne_x + 2Ne_z + 1). \tag{5.1}$$

For a fixed approximation order N, the total DOFs of the proposed solutions are:

$$DOF_{CUF} = 2(N+1)N_n \tag{5.2}$$

N_n stands for the nodes number along the beam axis. For slender beams, the most refined model is given by a mesh of 121 nodes and beam theory $N = 5$, and the DOFs of the proposed one-dimensional formulation are $1'452$, whereas a 240×24 elements used for the reference 2D FEM simulations, they are $35'618$.

Time Cost Comparison In this paragraph, the computation time need when using ANM or NRM are compared. In the analyses, a quadratic ($N = 2$) CUF model is used. The CPU time (t_{CPU}) is taken for the comparison between the two non-linear solvers. The displacement component u_z in a slender beam is considered. Tables. 5.1, 5.2, and 5.3 present the transverse displacement and the CPU times for different load steps using B2, B3 and B4 elements, respectively. Calculation accuracy takes into account two significant digits. CPU time of these two solvers can differ in the worst case by about 50%. Results show the efficiency of the ANM solver.

Step	λ	$u_z[m]$	$t_{CPU}^{ANM}[s]$	$t_{CPU}^{NRM}[s]$	$t_{CPU}^{ANM}/t_{CPU}^{NRM}$
2	1.37	2.41	17.98	80.98	0.22
3	3.67	4.95	33.09	135.42	0.24
4	8.14	8.50	47.13	195.21	0.24
5	17.44	14.14	60.69	239.00	0.25

Table 5.1: Transverse displacement and CPU time using ANM and NRM, B4 elements.

$Step$	λ	$u_z[m]$	$t_{CPU}^{ANM}[s]$	$t_{CPU}^{NRM}[s]$	$t_{CPU}^{ANM}/t_{CPU}^{NRM}$
2	1.24	2.18	17.47	55.02	0.32
3	3.30	4.49	32.68	100.98	0.32
4	7.31	7.70	46.14	142.84	0.32
5	15.56	12.86	59.72	185.43	0.32

Table 5.2: Transverse displacement and CPU time using ANM and NRM, B3 elements.

$Step$	λ	$u_z[m]$	$t_{CPU}^{ANM}[s]$	$t_{CPU}^{NRM}[s]$	$t_{CPU}^{ANM}/t_{CPU}^{NRM}$
2	1.57	2.19	17.91	44.89	0.40
3	4.17	4.50	36.08	82.25	0.44
4	9.21	7.72	53.11	110.25	0.48
5	19.52	12.86	67.90	141.10	0.48

Table 5.3: Transverse displacement and CPU time using ANM and NRM, B2 elements.

5.2   Static Analysis

Clamped-hinged beams are considered. A length-to-thickness ratio l/h as high as 100 (slender beams) and as low as 10 (short beams) is considered. MITC method was adopted for locking correction. Fig. 5.1 shows the difference between using and not using the MITC method for a B2 element. A concentrated force $f = 5EI/l^2$ applied at mid-span is considered. Displacement $\hat{u}_z = u_z/u_{Cubic}$ is evaluated at $(l/2, -h/2)$, where u_{Cubic} is the reference solution obtained by B4 elements (121 nodes). B4 element solution is used as reference since locking is negligible in this case. It can be noticed that the MITC beam elements are free of locking regardless the beam theory order N.

A convergence analysis versus the number of nodes is now presented. A slender beam ($l/h = 100$) under a concentrated force $f = EI/l^2$ along the z-direction is investigated. The previously considered normalised displacement $\hat{u}_z$ evaluated at $(l/2, -h/2)$ and calculated via B4 elements is presented Fig. 5.2. The node number N_n changes from 7 to 481. With the adoption of MITC, the convergence is obtained with 25 nodes, whereas without MITC correction is achieved with 301 nodes. A similar behaviour can be observed with B2 and B3 elements. MITC correction is applied to all the remaining analyses. According to the convergence analysis outcome, 241 and 121 nodes are used for slender and short beams, respectively.

Results are now compared with the ANSYS solutions. Besides displacements, the PK2 axial and shear stresses in the global system are presented. The evaluation point for u_x is $(l, h/2)$, whereas u_z is evaluated at $(l/2, -h/2)$. For slender cases, the load-displacement curves can be found in Fig 5.3. The beam is under a concentrated z-direction dimensionless force $\lambda = 120$ at the centre point $(l/2,0)$.
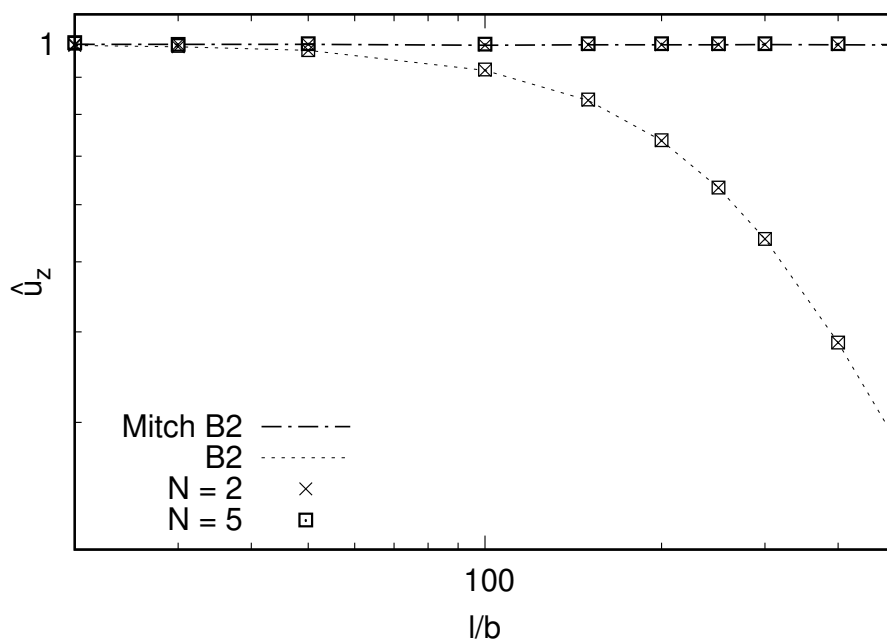
Figure 5.1: Locking correction via MITC method for B2 elements with different beam theories $N = 2$ and $N = 5$, clamped-hinged beam.

Table 5.4 presents the displacement components u_x and u_z. Results show an excellent agreement between 1D CUF models, 2D FEM models and the solutions from ANSYS. For a third-order model, the relative error between beams theories and reference solution is 0.94%, at worst. The stress components are given in Table 5.5. The difference is about 0.52% for $N \geq 3$, at worst, in the case of the stress components. To be noticed, the computational time for FEM 2D with 400×40 is more than 2 hours (where a sparse matrix storage scheme has been used to optimize the code), yet the computational time for the highest order theory $N = 5$ is no more than 10 minutes.

	$u_x \times -1[m]$			$u_z \times -10^{-1}[m]$		
2D FEM ($400 * 40$)	3.7476			1.7478		
	B2	B3	B4	B2	B3	B4
1D CUF $N = 5$	3.7538	3.7495	3.7478	1.7493	1.7483	1.7479
1D CUF $N = 4$	3.7490	3.7418	3.7419	1.7482	1.7465	1.7465
1D CUF $N = 3$	3.7269	3.7290	3.7218	1.7430	1.7435	1.7418
1D CUF $N = 2$	3.7069	3.7094	3.7056	1.7383	1.7388	1.7379

Table 5.4: u_x and u_z in a slender clamped-hinged beam.
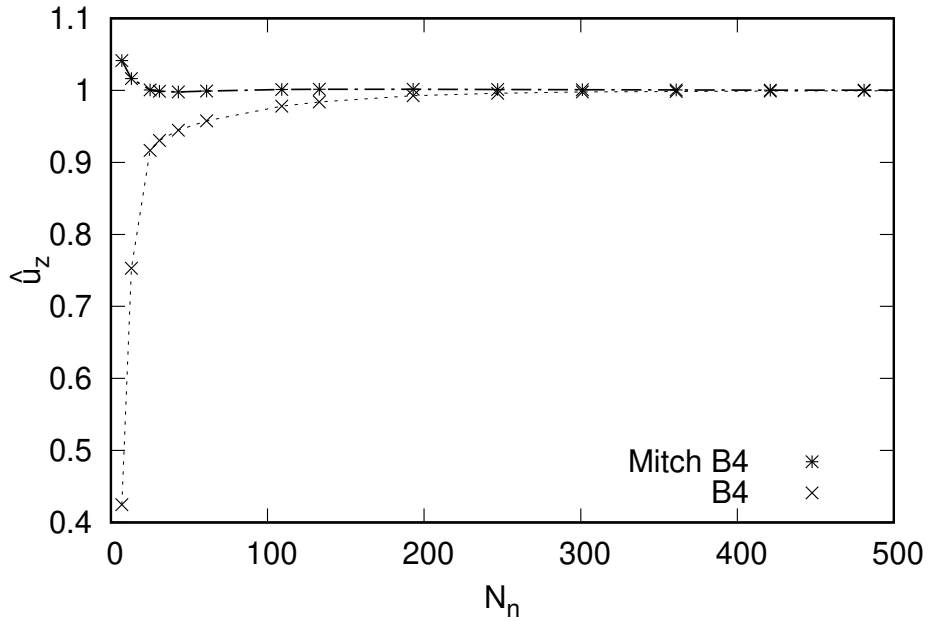
Figure 5.2: Convergence analysis via MITC method for B4 elements, $N = 2$, clamped hinged slender ($l/h = 100$) beam.
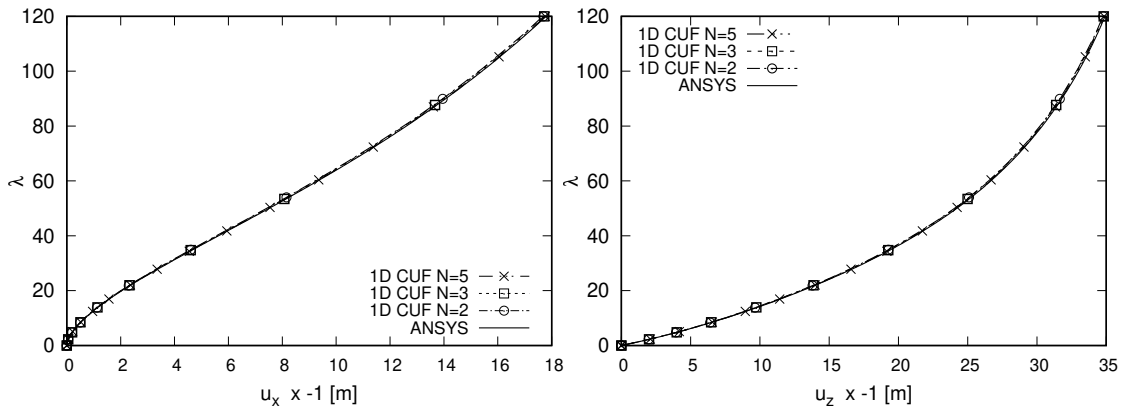
Figure 5.3: Load-displacement curves u_x and u_z for slender clamped-hinged beams.

For short beams, the load-displacement curves are presented in Fig. 5.4. Fig. 5.5 shows the load-stresses curves for S_{xx} at ($l/10$, $h/2$) and S_{xz} at ($l/4$,0), respectively. According to these plots, it can be concluded that higher-order beam theories are needed for shear stress S_{xz}. Comparing the other solutions, although the 1D CUF $N = 2$ model can only obtain relatively accurate displacements and the normal stress S_{xx} but not
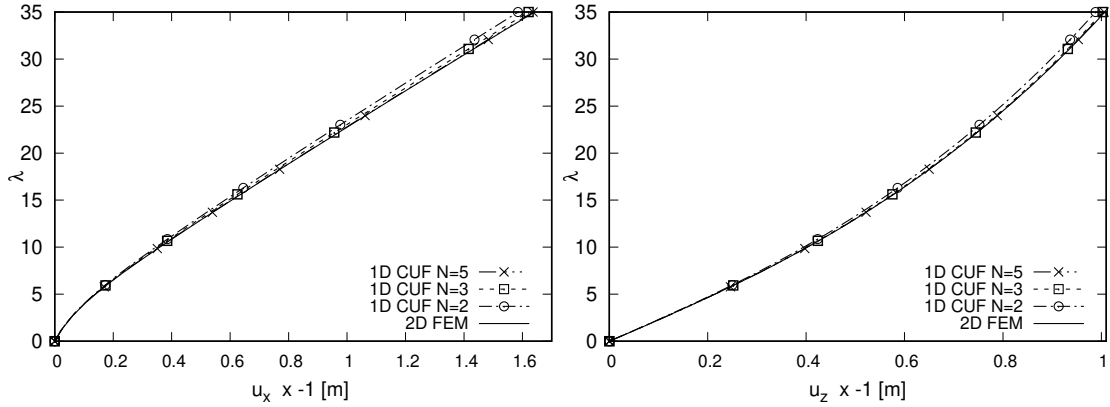
Figure 5.4: Load-displacement curves u_x and u_z, short clamped-hinged beams.
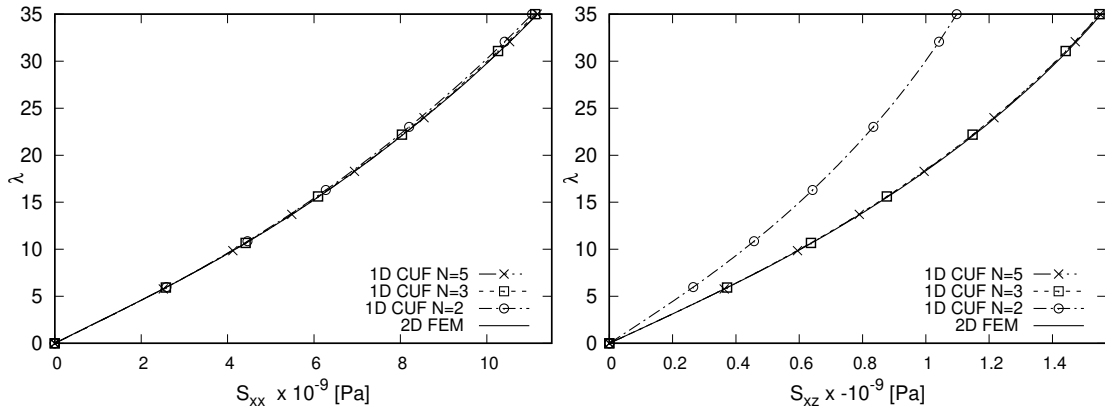
Figure 5.5: Load-stress curves S_{xx} and S_{xz}, short clamped-hinged beams.

shear stress S_{xz}. At $\lambda = 5$, the error is 16.7%. Additionally, at $\lambda = 35$, the error is as high as 30%. Table 5.6 presents the displacement components u_x and u_z in short beams. Results show an excellent agreement between advanced 1D CUF models and 2D FEM solution. For a fourth-order model, the relative difference between beams theories and reference solution is 0.13%, at worst. The stress components are addressed in Table 5.7. The difference is about 1.33%, at worst, in the case of the stress components. The difference in the B2 solution for $\overline{S}_{xz}$ is because results did not converge yet for $N_n = 121$. Short beams results are presented from Table 5.6 to 5.7.

The contour plots for u_x, u_z, S_{xx}, S_{xz}, and S_{zz} are presented in Figs. 5.6, 5.7, 5.8, 5.9, respectively. Slight difference at the beam centre point can be found for S_{zz} and S_{xz}. It is due to the stress concentration coming from the application the external force.

	$S_{xx} \times 10^{-8}[Pa]$			$S_{xz} \times -10^{-7}[Pa]$		
2D FEM (400 * 40)	9.2049			1.4142		
	*B*2	*B*3	*B*4	*B*2	*B*3	*B*4
1D CUF $N = 5$	9.3532	9.2171	9.2027	0.3778	1.6365	1.3919
1D CUF $N = 4$	9.3518	9.2267	9.2101	0.3802	1.6319	1.3914
1D CUF $N = 3$	9.3276	9.2148	9.1749	0.3917	1.6324	1.3897
1D CUF $N = 2$	9.3009	9.1887	9.1525	0.3894	1.2251	0.9830

Table 5.5: S_{xx} and S_{xz} in a slender clamped-hinged beam.

	$u_x \times -[m]$			$u_z \times -10^{-1}[m]$		
2D FEM (160 * 16)	1.3723			9.1386		
	*B*2	*B*3	*B*4	*B*2	*B*3	*B*4
1D CUF $N = 5$	1.3740	1.3745	1.3739	9.1382	9.1400	9.1397
1D CUF $N = 4$	1.3706	1.3708	1.3703	9.1312	9.1323	9.1318
1D CUF $N = 3$	1.3601	1.3602	1.3599	9.1113	9.1129	9.1128
1D CUF $N = 2$	1.3303	1.3303	1.3302	8.9782	8.9800	8.9799

Table 5.6: u_x and u_z in a short clamped-hinged beam.

5.3 Post-buckling Analysis

A buckling analysis is presented, Clamped-hinged and cantilever boundary conditions are presented. Beams are loaded by a compressive force applied at a beam end and buckling is trigged by applying a perturbation force $10^{-4}f$ along the z-direction. For structural level geometrical nonlinear analyses, Hutchinson [95], Hutchinson and Koiter [96] gave the conclusion that the smaller disturbance will cause the bifurcation curve to be sharper.

5.3.1 Clamped-hinged Beams

For clamped-hinged beams (slenderness ratio $l/h = 20$), 1D CUF models are compared to the 2D FEM model using eight-nodes elements. The mesh of the 2D FEM model is 80×8, and 1D CUF model uses 121 nodes and B4 elements. The ANM expansion order is 20, and the tolerance is 10^{-8}. The results are given in Figs. 5.10 and 5.11. The buckling phenomenon is well captured, and bifurcation point is detected at $\lambda = 20$. The displacement curve is in good agreement with the one corresponding to the reference

	$S_{xx} \times 10^{-10}[Pa]$			$S_{xz} \times -10^{-9}[Pa]$		
2D FEM (160 * 16)	1.0062			1.4299		
	B2	B3	B4	B2	B3	B4
1D CUF $N = 5$	1.0346	1.0071	1.0048	1.3832	1.4214	1.4118
1D CUF $N = 4$	1.0352	1.0079	1.0055	1.3823	1.4204	1.4109
1D CUF $N = 3$	1.0305	1.0033	1.0010	1.3818	1.4198	1.4103
1D CUF $N = 2$	1.0237	0.9963	0.9941	0.9699	1.0083	0.9988

Table 5.7: S_{xx} and S_{xz} in a short clamped-hinged beam.

1D CUF $N = 5$

u_x u_z

2D FEM
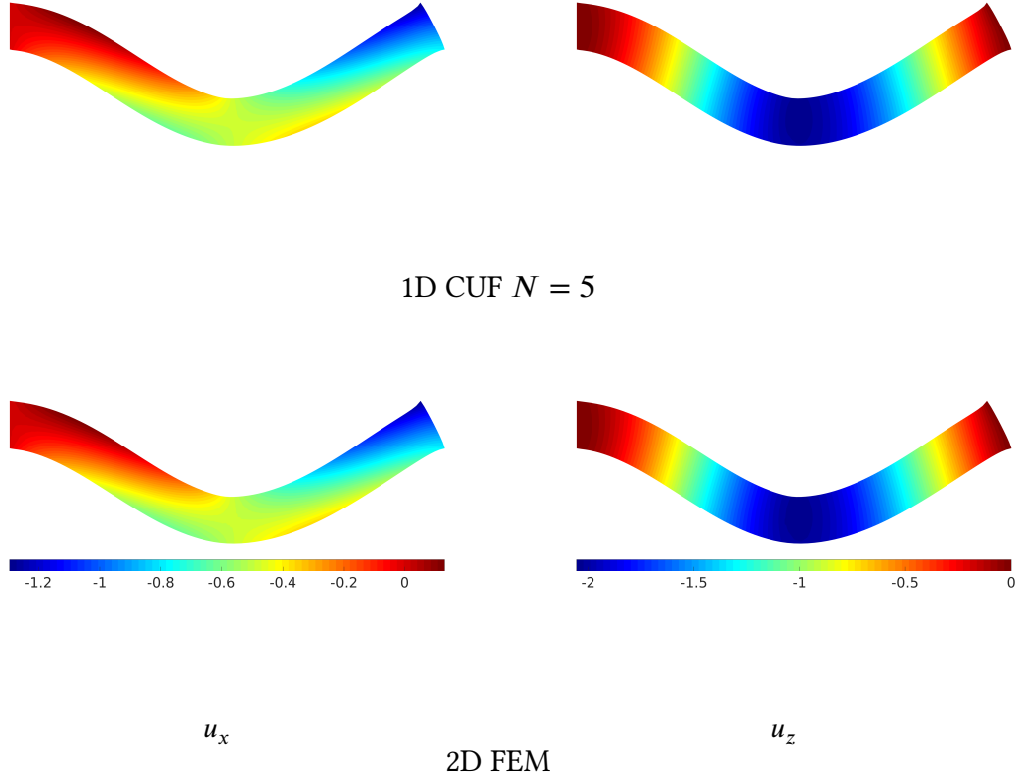
Figure 5.6: Contours for u_x and u_z [m] in short clamped-hinged beams.

ANSYS solution. As for the normal stress, the 1D CUF $N = 2$ model capture the S_{xx} well, but it is not accurate for the shear stress S_{xz}. The difference between S_{xz} from 1D CUF $N = 2$ and other results starts from the bifurcation point, and increases as the load parameter λ gets larger. At the point $\lambda = 41.67$, the error reaches approximately 30%. Although the 1D CUF $N = 2$ model is not accurate for shear stress S_{xz}, the critical

1D CUF $N = 5$

2D FEM
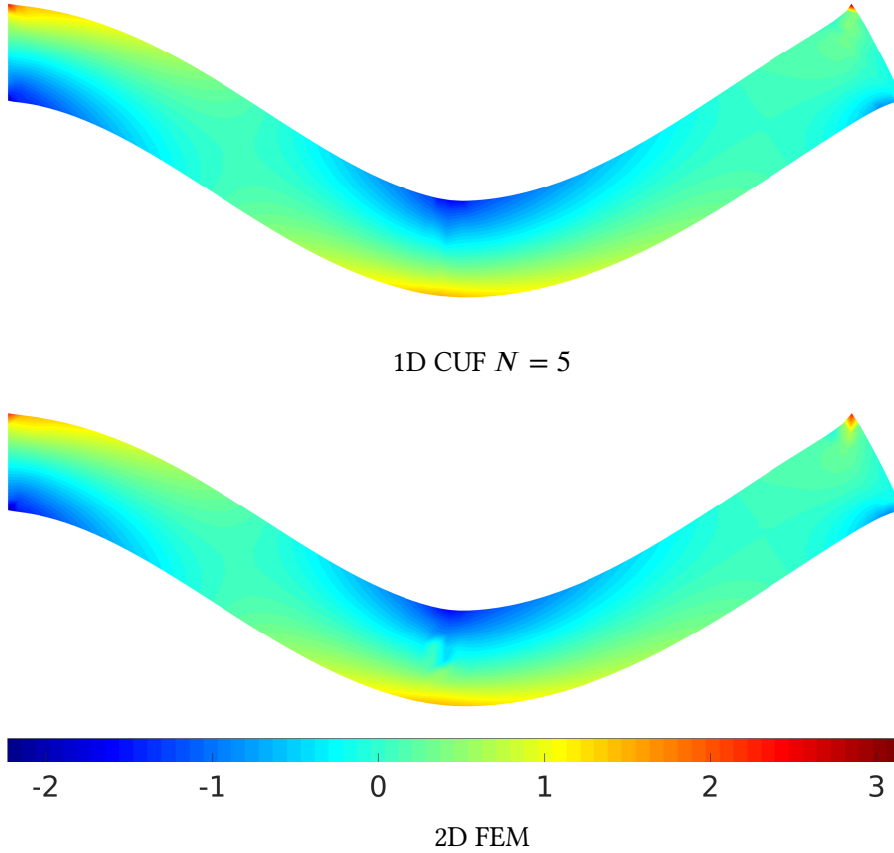
Figure 5.7: Contours plot of S_{xx} [Pa] in short clamped-hinged beams.

load is detected accurately. The 1D CUF $N = 3$ model is reliable for all the considered stress components. Contour plots of displacement and stress components (u_x, u_z, S_{xx} and S_{xz}) for the last load step are shown in Figs. 5.12, 5.13, 5.14, and 5.15.

5.3.2 Cantilever Beams

A cantilever beam with a concentrated x-direction force $f = EI/l^2$ at the right end $(l,0)$ is analysed. Besides, a z-direction perturbation of value $10^{-4}f$ at the centre point $(l/2, 0)$ have been introduced to trigger buckling. Geometrical and material data are the same as the previous case. Fig. 5.16 and 5.17 illustrate the load-displacement and load-stress bifurcation curves of 1D CUF model and 2D FEM model.
 The two solutions agree well, and a critical buckling load parameter $\lambda_{critical}$ equal to 2.46 is obtained by both of them. Higher-order theories with $N \geq 3$ are necessary for the stress component S_{xz}. Fig. 5.18 presents the axial and shear stress components S_{xx} and S_{xx} for the last step. Results are accurate over the whole beam with the exclusion of points where stress concentration occurs $(l,0)$. Coherently to what is observed in

1D CUF $N = 5$

2D FEM
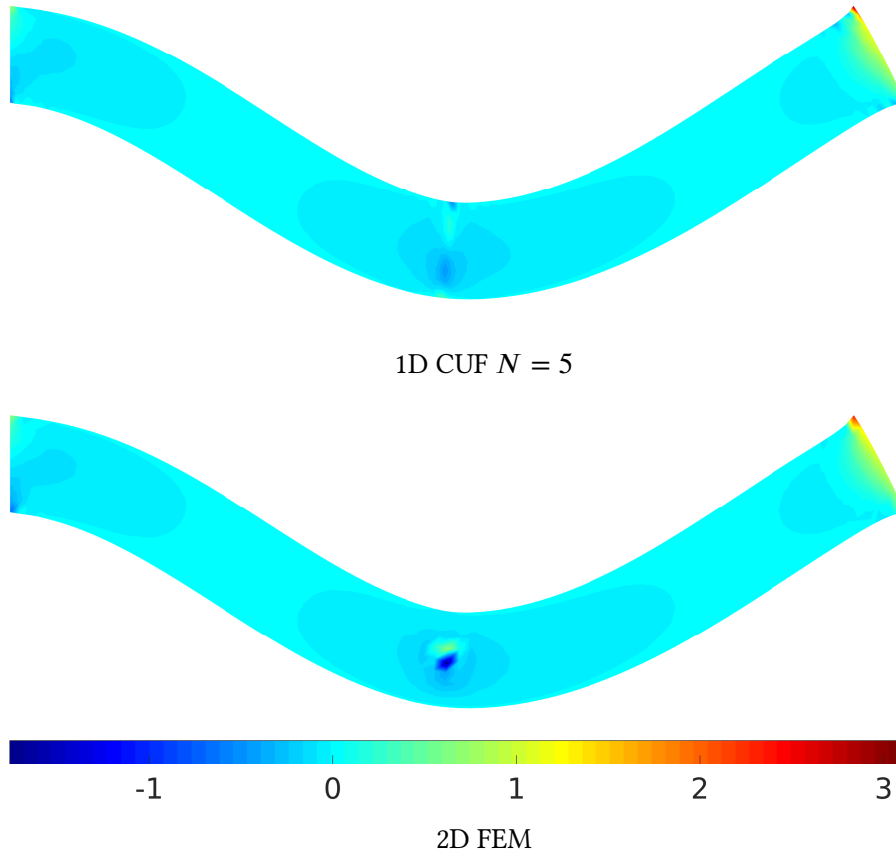
Figure 5.8: Contours for S_{zz} [Pa] in short clamped-hinged beams.

displacement-load curves, the last-step deformations from these two model match well.

5.4 Snap-through Analysis

With the same geometrical and material data, a snap-through case is analysed for a simply supported beam ($l/h = 20$). The snap-through analysis can be separated into two parts.

Firstly, a buckling analysis is carried out by applying a x-direction concentrated force $f = EI/l^2$ at $(l, 0)$. Fig. 5.19 shows that the results of the 1D CUF model with higher-order theory $N = 5$ compares well with the 2D FEM model. To be noticed, higher-order theory $N = 5$ is necessary for an accurate comparison.

Secondly, the initial geometrical and stress condition of the second part of the analysis are those at the end of the previous one. In other words, the beam is now curved and pre-stressed. Now, load $f = 10^5 N$ is applied in z direction is at the centre ($l/2$,0). Fig. 5.20

1D CUF $N = 5$

2D FEM
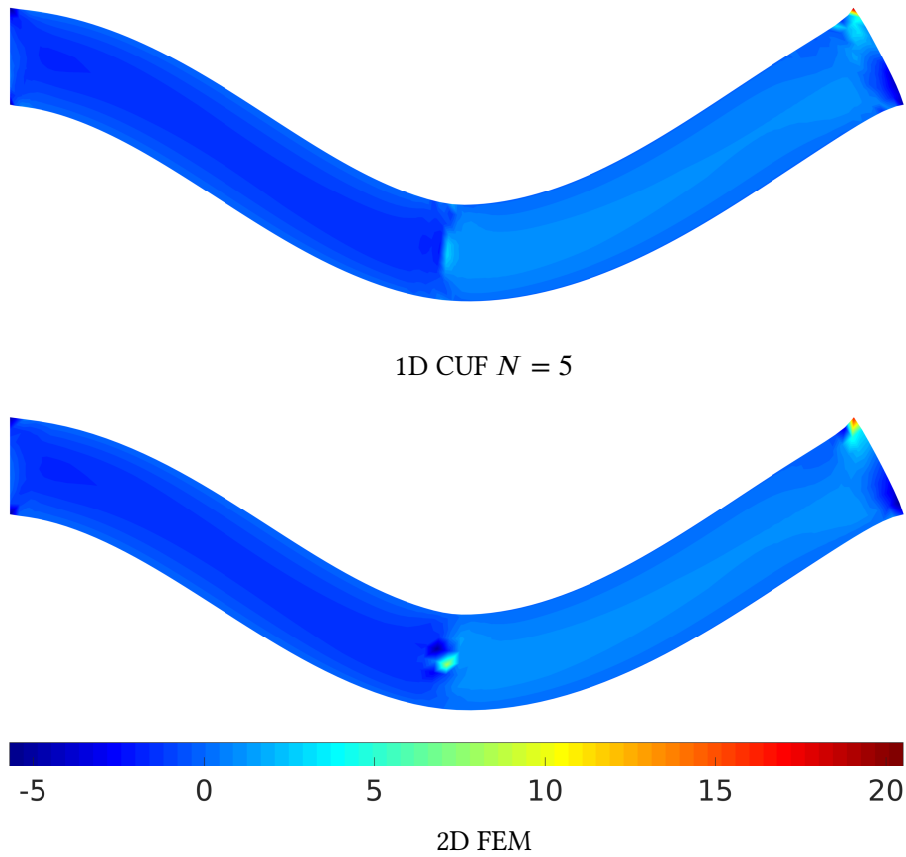
Figure 5.9: Contours plot of S_{xz} [Pa] in short clamped-hinged beams.
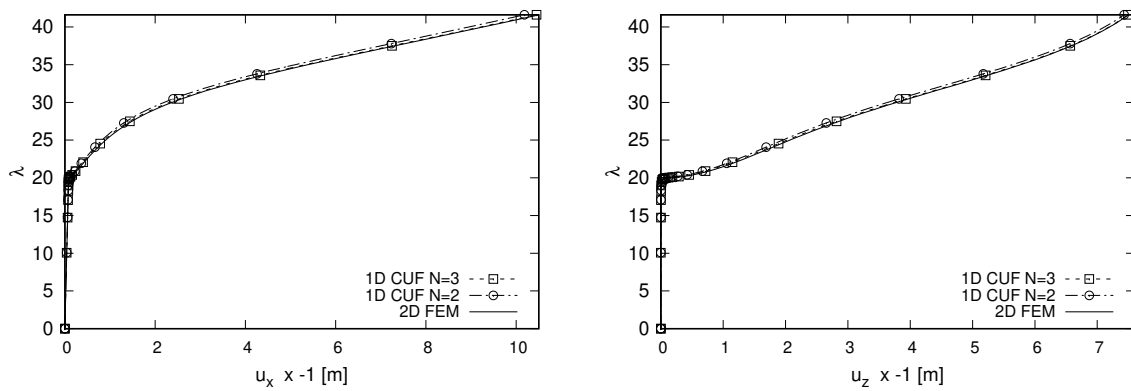
Figure 5.10: Load-displacement curves for u_x at $(l, h/2)$ and u_z at $(l/2, -h/2)$, clamped-hinged beam ($l/h = 20$).

79
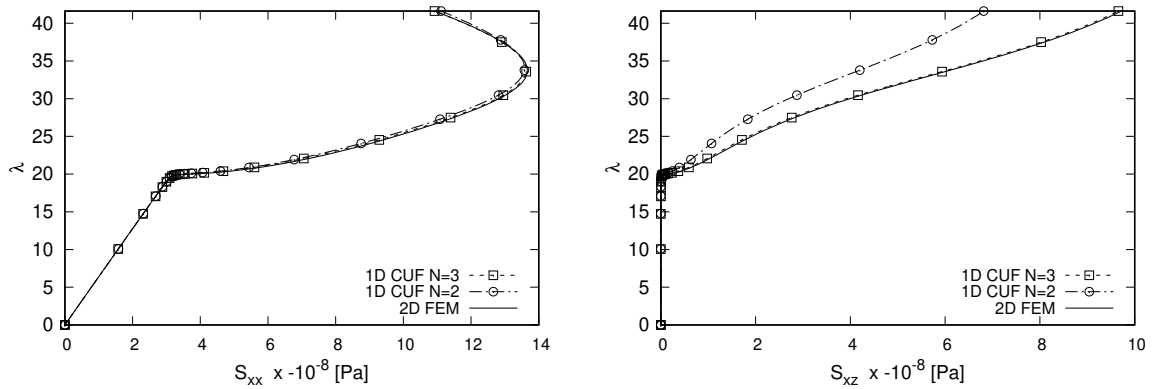
Figure 5.11: Load-stress curves for S_{xx} at $(l/4, -h/2)$ and S_{xz} at $(l/4,0)$ of a clamped-hinged beam ($l/h = 20$).

1D CUF $N = 5$

u_x u_z

2D FEM
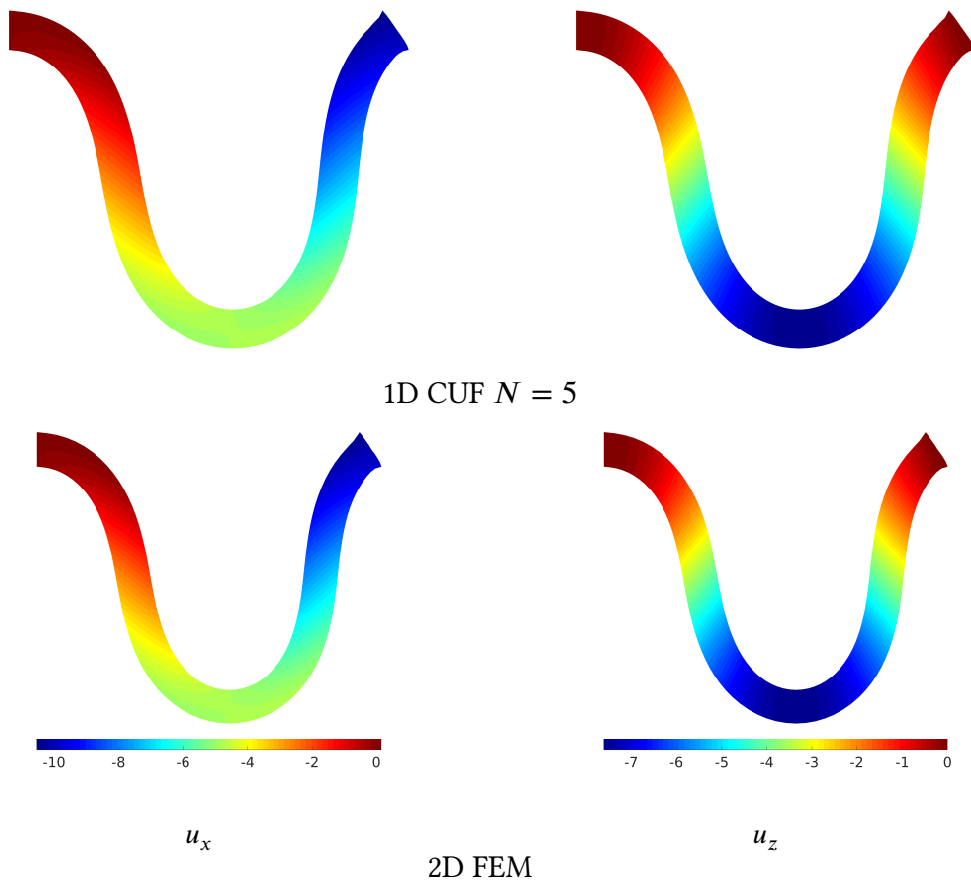
Figure 5.12: Contours plot of u_x and u_z [m] in short clamped-hinged beams.

1D CUF $N = 5$

2D FEM
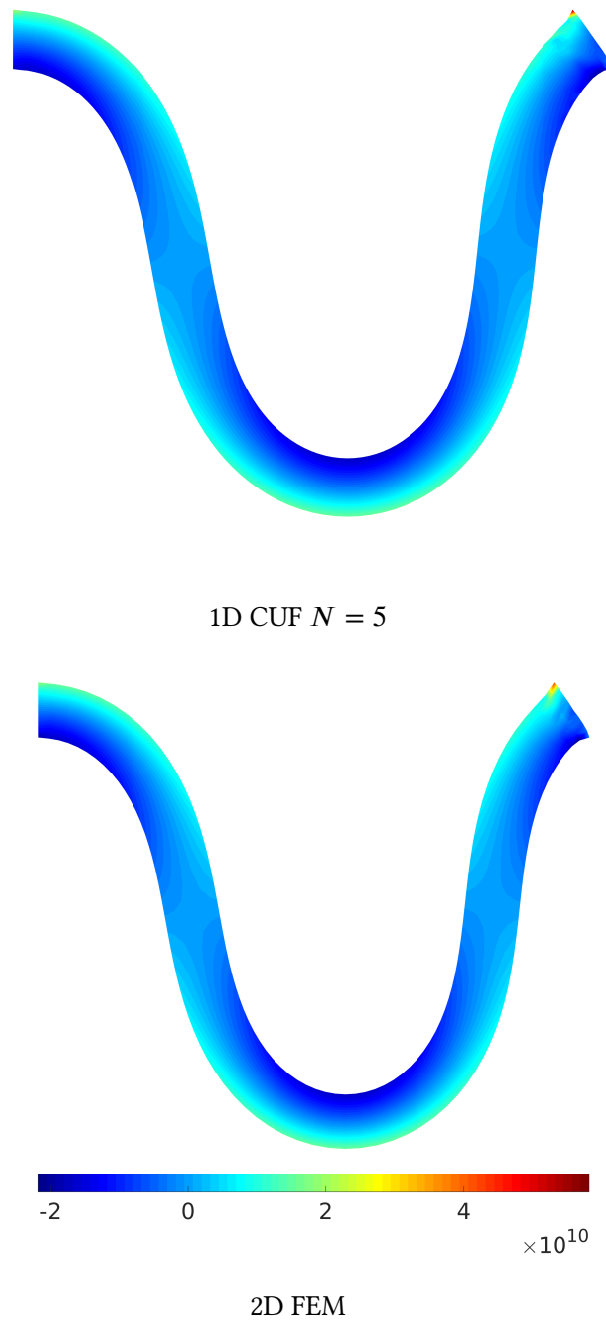
Figure 5.13: Contours for S_{xx} of clamped-hinged beams.

shows the excellent performance of the 1D CUF model with $N = 5$, which matches the reference solution.

The displacement resultant $\sqrt{u_x^2 + u_z^2}$ for several steps is presented in Fig. 5.21. As for
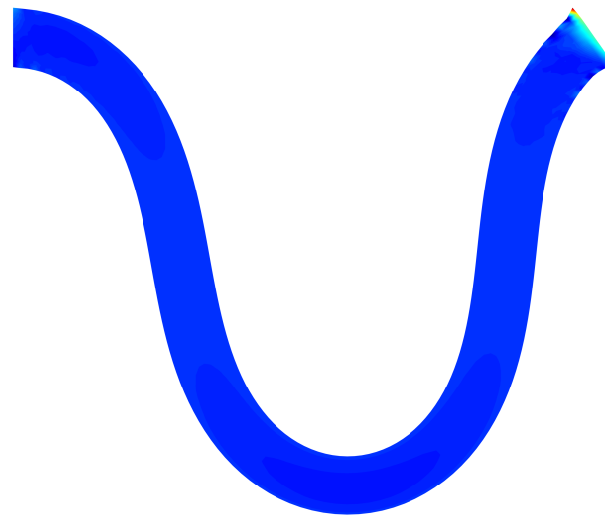
1D CUF $N = 5$
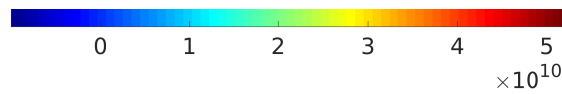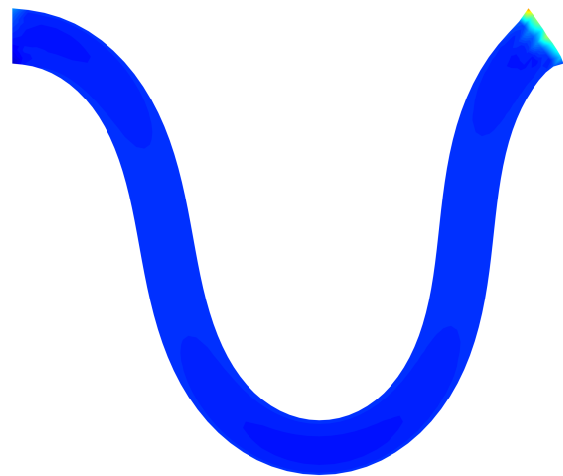
2D FEM

Figure 5.14: Contours for S_{zz} of clamped-hinged beams.

more details, the qualitative variation of the displacement and stress components for the last step ($\lambda = 200$) is presented in Figs. 5.22 and 5.23.

Compared with the 2D FEM model, the 1D CUF model proposed in this thesis requires

1D CUF $N = 5$

2D FEM
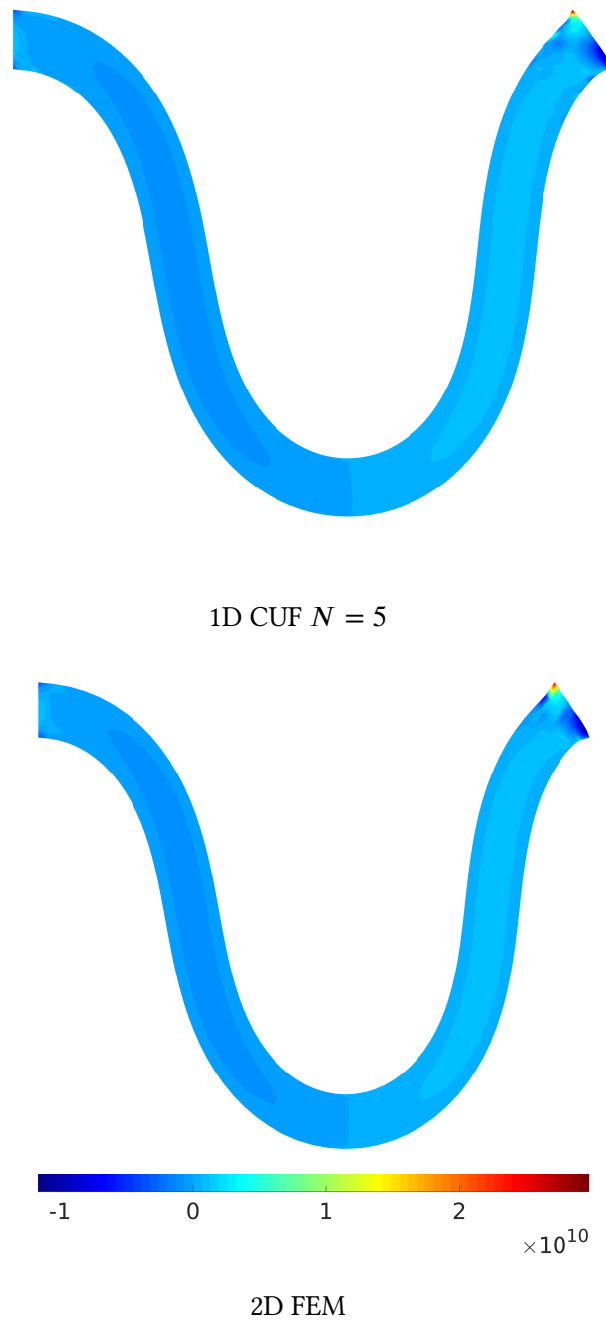
Figure 5.15: Contours for S_{xz} of clamped-hinged beams.

a smaller number of unknown variables to be solved. A two-dimensional solution with 80×8 Q8 elements is taken as a reference, corresponding to the number of 4194 DOFs. The most refined 1D CUF model is a fifth-order ($N = 5$) model with 121 nodes along the
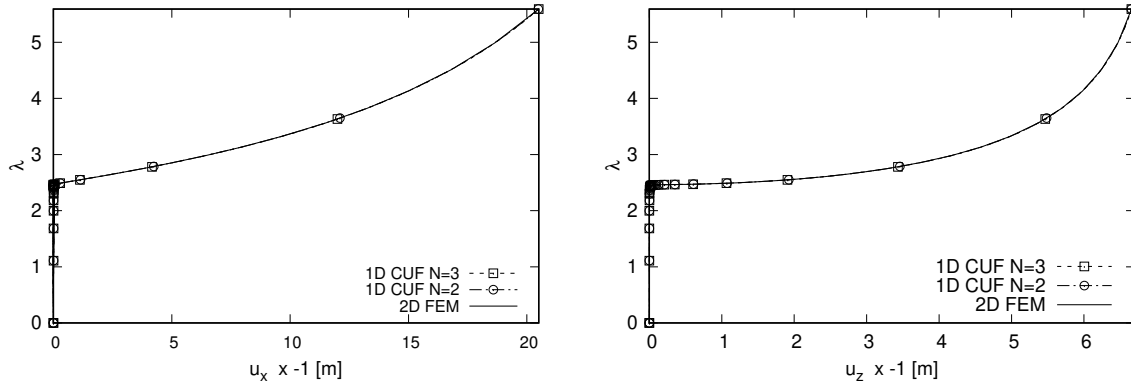
Figure 5.16: Load-displacement curves u_x at $(l, h/2)$ and u_z at $(l/2, -h/2)$ in a cantilever beam ($l/h = 20$).
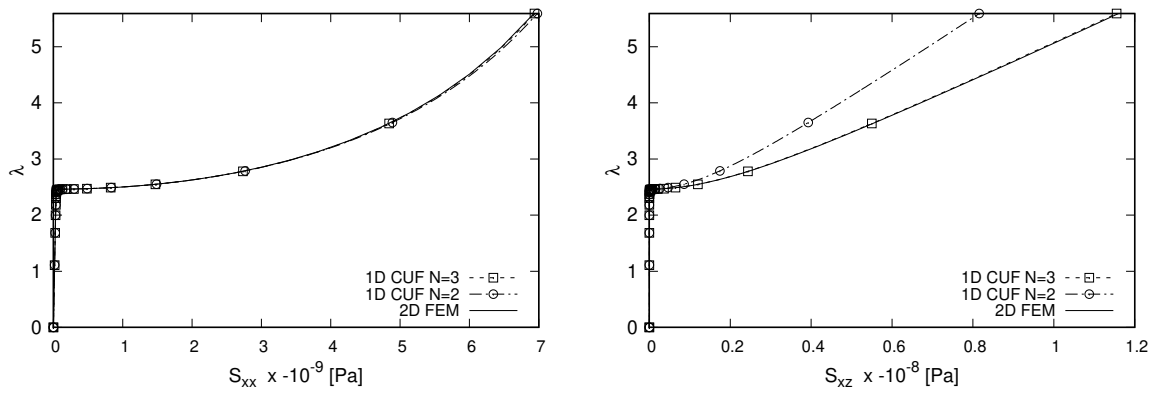
Figure 5.17: Load-stress curves for S_{xx} at $(l/4, -h/2)$, S_{zz} at $(l/4,0)$ and S_{zz} at $(l/4,0)$ in a cantilever beam ($l/h = 20$).

axis, corresponding to 1452 degrees of freedom (-65.4%). Therefore, the proposed CUF-based geometric nonlinear beam model represents an efficient modelling for analysing the snap-through problem.

1D CUF $N = 5$ 2D FEM   1D CUF $N = 5$ 2D FEM
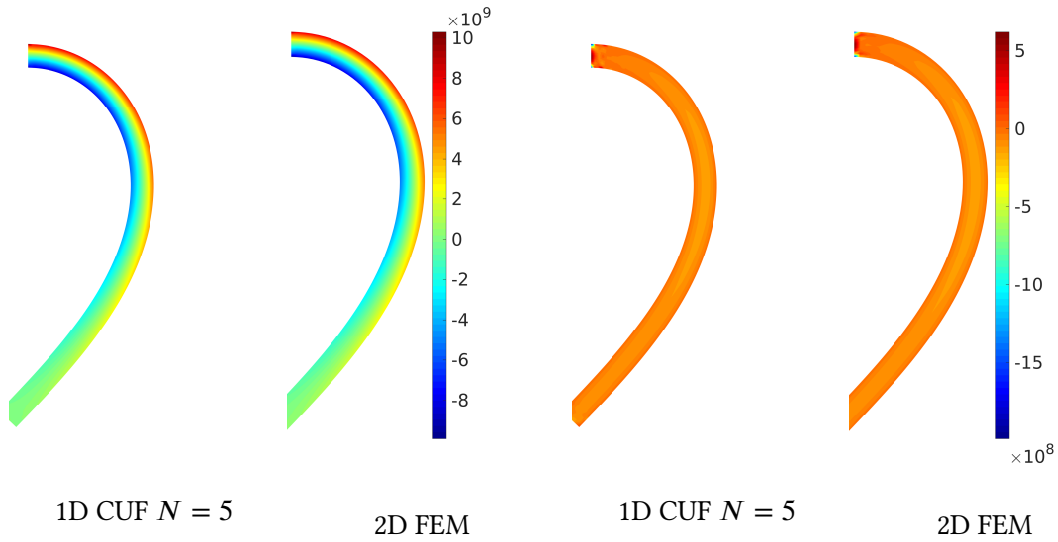
Figure 5.18: Contours plot S_{xx} (left side) and S_{xz} (right side) [Pa] in cantilever beams.
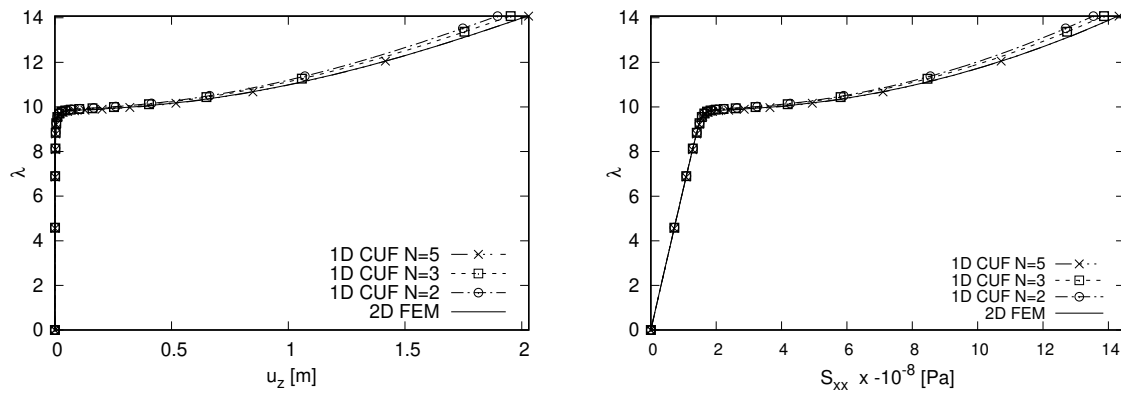
Figure 5.19: Load-displacement curve u_z at $(l/2, h/2)$ and load-stress curve S_{xx} at $(l/4, -h/2)$ in a simply-supported beam ($l/h = 20$).
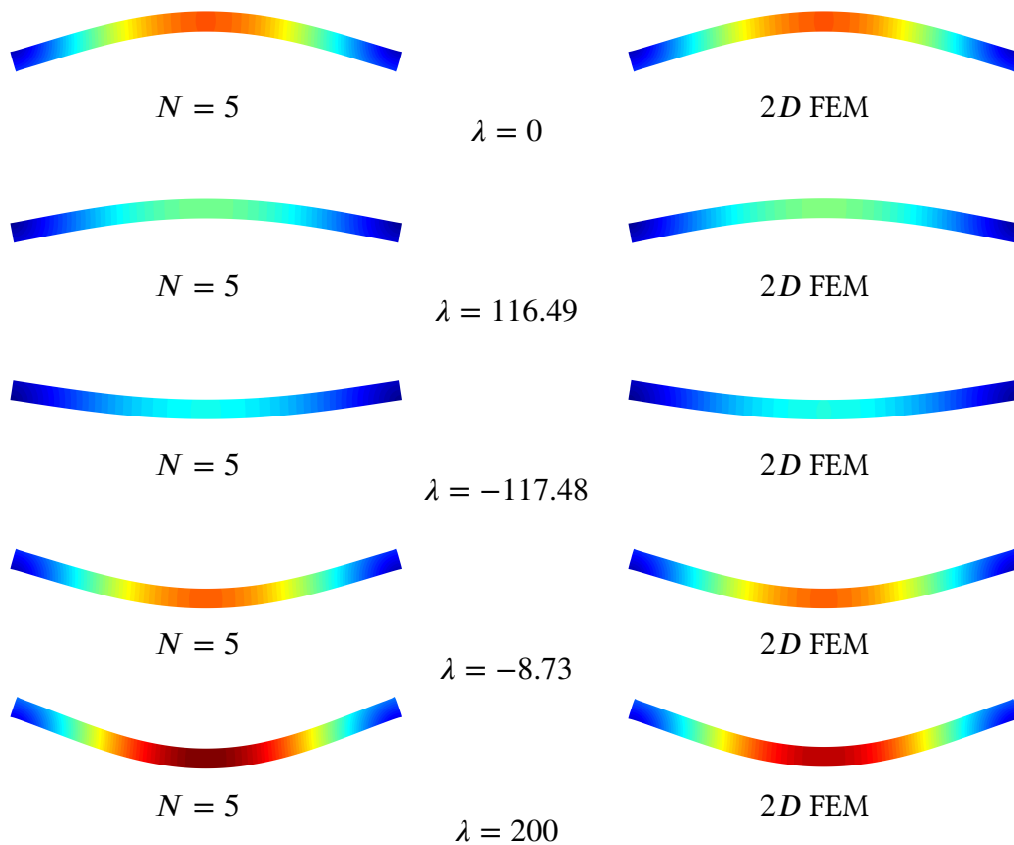
85
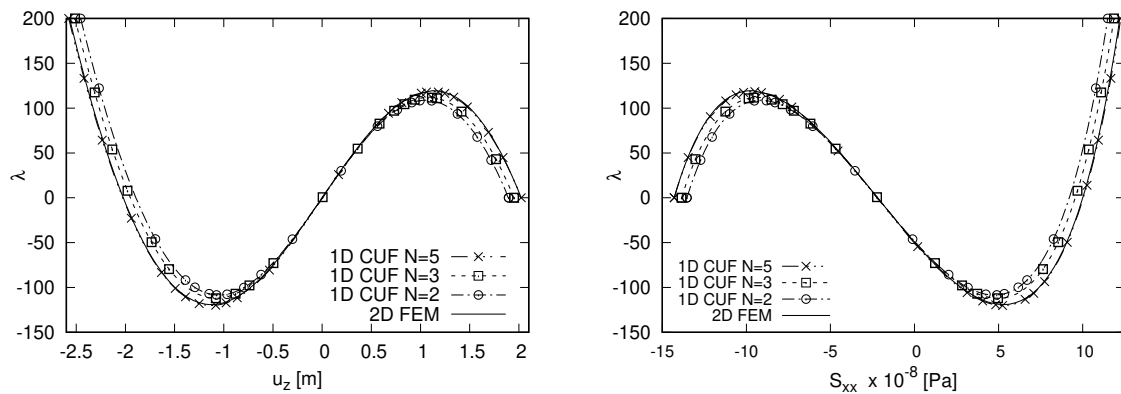
Figure 5.20: Load-displacement curve u_z at $(l/2, h/2)$ and load-stress curve S_{xx} at $(l/4, -h/2)$ in a simply-supported beam $(l/h = 20)$.

Figure 5.21: Contours plot for the displacement resultant $\sqrt{u_x^2 + u_z^2}$ [m] in a simply-supported beams.
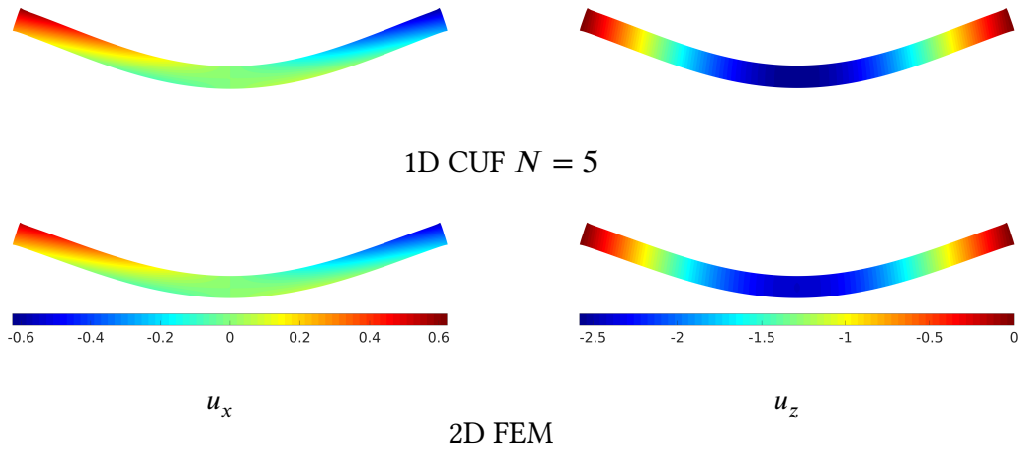
1D CUF $N = 5$

u_x u_z

2D FEM

Figure 5.22: Contours u_x and u_z [m] in simply-supported beams.
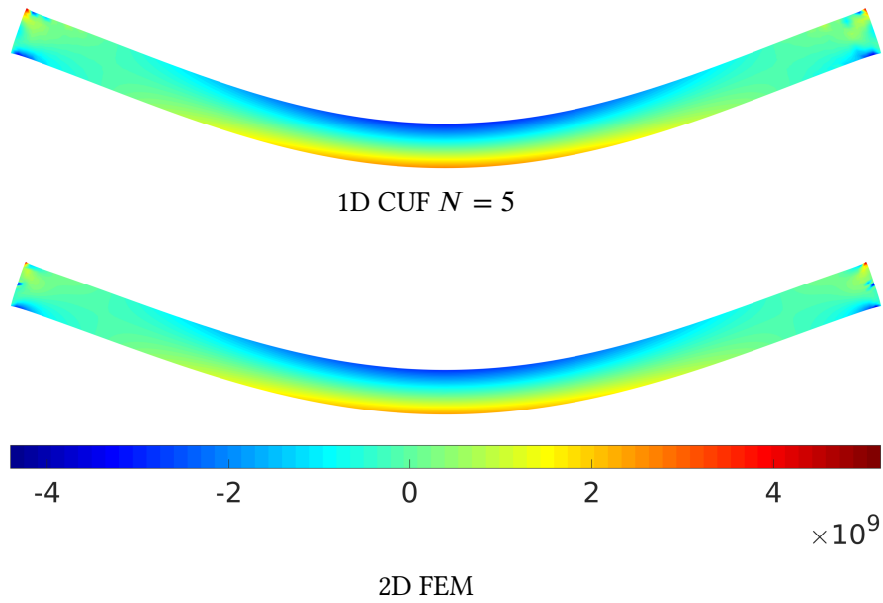
1D CUF $N = 5$

2D FEM

Figure 5.23: Contours plot S_{xx} [Pa] in simply-supported beams.
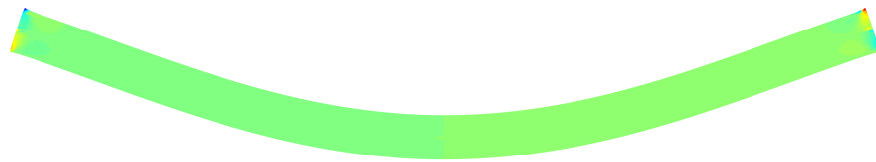
1D CUF $N = 5$

2D FEM

Figure 5.24: Contours plot S_{zz} [Pa] in simply-supported beams.

1D CUF $N = 5$

2D FEM

Figure 5.25: Contours plot S_{xz} [Pa] of simply-supported beams.

Chapter 6

Multi-scale Analysis of Beam Structures

Analyses are carried out by the multi-scale model proposed in Chapter 4. First, the proposed framework is validated towards a case study presented in the literature, see Nezamabadi et al. [130]. Then, an example of the instability of a simply-supported fibre-reinforced beam is proposed.

6.1   Validation: Bending of a Rectangular Beam

This first case study consists in a heterogeneous cantilever rectangular beam under a concentrated unit vertical force applied as shown in Fig. 6.1. The length of the beam is 100 mm, and the thickness is 10 mm. At the microscale, the material consists of a matrix with a circular inclusion (the volume fraction of the inclusion is equal to 28%). Constituents material properties are shown in Table 6.1. Results from Nezamabadi et al. [130] and a FE^2 solution where two-dimensional finite elements are used at macroscale (this last solution is called 2D FE^2).

A preliminary convergence analysis to assess the mesh size used at RVE level for de-

	Matrix	Inclusion
Young Modulus [MPa]	10000	100000
Poisson's Ratio	0.3	0.3
Volume Fraction	0.72	0.28

Table 6.1: Material property of the constituents, first case.

termining the effective properties is presented in Table 6.2. The solution proposed here
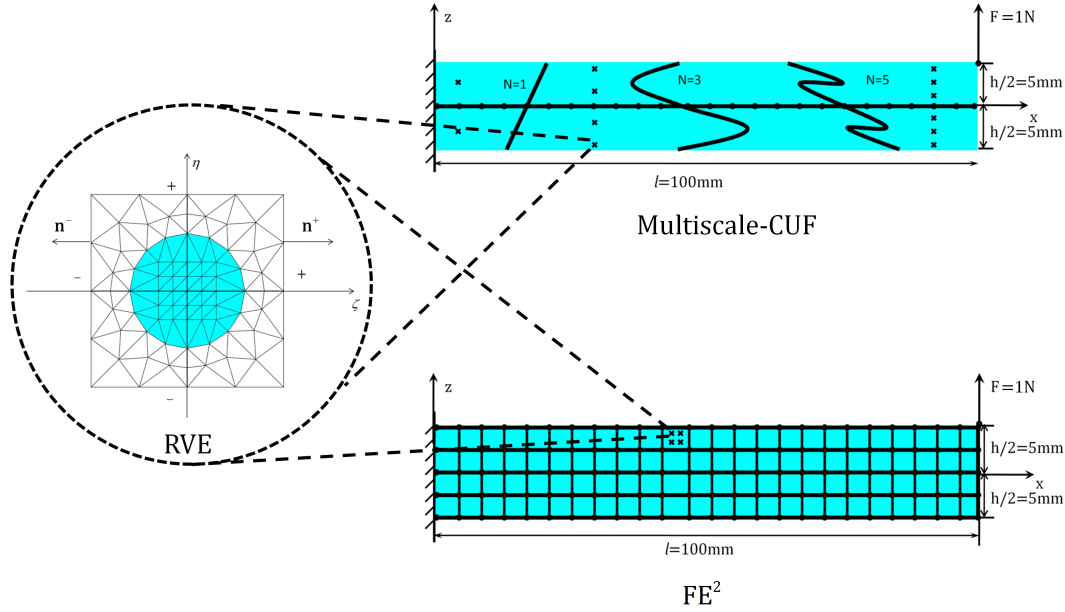
Figure 6.1: Geometry of a cantilever beam under static load with round inclusion RVE.

	$E[GPa]$	$G[GPa]$	v
Present study[a]	151.70	53.63	0.28
Reference[b] [6]	153.27	54.01	0.28
ANSYS[c]	153.36	54.03	0.28

[a] 144 triangular 6 nodes elements

[b] 4132 triangular 6 nodes elements

[c] 4044 PLANE 183 elements

Table 6.2: Effective properties estimations.

uses a mesh with 144 elements which proofs to be a good compromise between accuracy and computational costs.

The comparison of degrees of freedoms between the proposed Multiscale-CUF model with different beam theories ($N = 2,3,4,5$) and the 2D FE^2 method from the reference paper is shown in Table 6.3 where reduction of the DOFs number can be remarked. Compared to the 2D FE^2 model, the DOFs have been reduced by two ($N = 5$) to four ($N = 2$) times by the 1D Multiscale-CUF model.

It is well-known that the FE^2 method is much less computationally expensive compared with a fully meshed model. Thanks to the proposed approach where a one-dimensional beam model is used at macro-scale, even the model with the highest expansion order
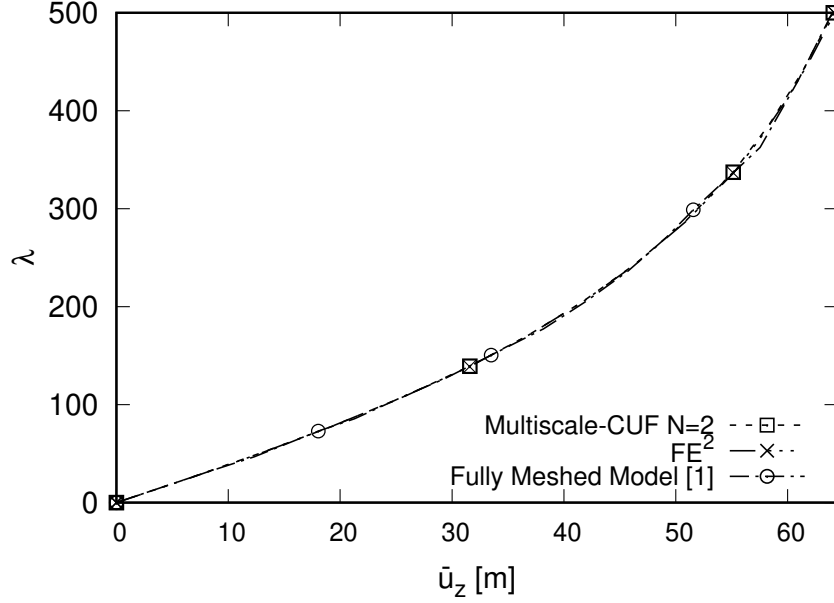
Figure 6.2: Load-displacement curve for $\overline{u}_z$ at $(l, h/2)$.

	RVE number	DOFs (Microscale[a])	DOFs (Macroscale)
Multiscale-CUF $N5$	720	$439'200$	972
Multiscale-CUF $N4$	600	$366'000$	810
Multiscale-CUF $N3$	480	$292'800$	648
Multiscale-CUF $N2$	360	$219'600$	486
FE^2	1440	$878'400$	$1'138$

[a] DOFs (Microscale) is the number of RVEs multiplied by the DOFs of each RVE.

Table 6.3: DOFs comparison between Multiscale-CUF and FE^2 models, where at macroscale Multiscale-CUF model uses 40 quadratic elements whereas a mesh 40×4 (length×thickness) is used for the FE^2 solution.

$(N = 5)$ presents half of the DOFs of the 2D FE^2 model. Furthermore, the results with $N = 2$ are already accurate as shown in Fig. 6.2, where the macroscale transverse displacement variation versus the load parameter is presented.

As a second problem, at the structural level, a concentrated load is applied at the point $(l,0)$. The length and the width of the beam are 10 m and 1 m, respectively. At the microscopic scale, the same matrix-circular inclusion configuration as for the previous case is considered where the constituent material properties are presented in Table 6.4. For this case, the load-displacement curves for $\overline{u}_x$ and $\overline{u}_z$ are presented in Fig. 6.3. $N = 2$ yields accurate results.

	Matrix	Inclusion
Young Modulus [MPa]	100	1000
Poisson's Ratio	0.3	0.3
Volume Fraction	0.72	0.28

Table 6.4: Material Properties of RVE constituents, second case.
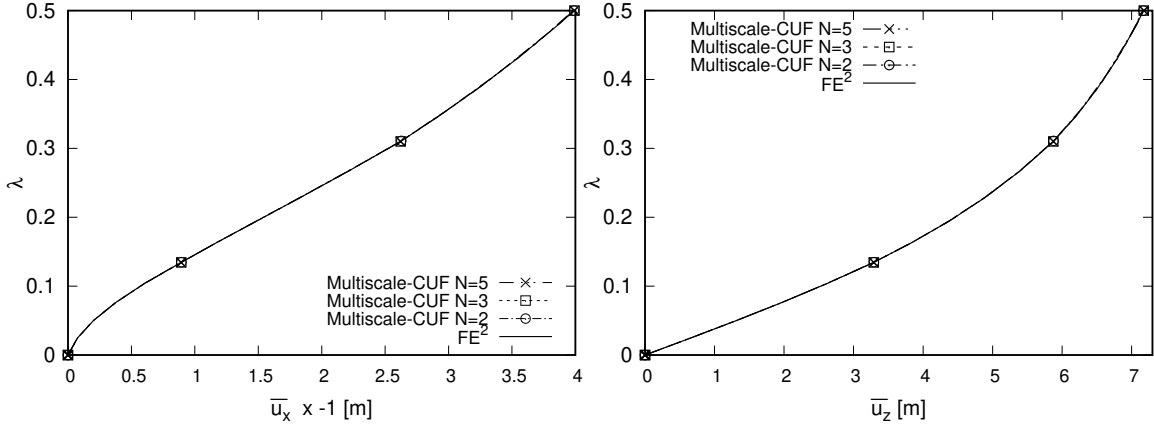
Figure 6.3: Displacement $\overline{u}_x$ (left) at $(l, h/2)$ and $\overline{u}_z$ (right) at $(l, -h/2)$) versus the load parameter in a short cantilever beam.

Moreover, Fig. 6.4 shows an excellent agreement at the microstructural level between the proposed model and the FE^2 model.

From Fig. 6.5, it can be concluded that the stress components require a higher-order theory ($N = 5$) to get an accurate result. From Fig. 6.5, between the result from the FE^2 model and the one from $N = 2,3$ models, the maximum difference is less than 2%. Furthermore, the curve obtained by $N = 5$ is entirely coincident with the reference curve. In Fig. 6.6, the shear stress at the middle line ($z/l = 0$) of the beam versus the axial coordinated is plotted. The results with $N = 3$ and $N = 5$ compare well with the 2D FE^2 model.

6.2 Fibre Reinforced Material Microbuckling

In this second example, sinusoidal geometrical imperfections are introduced for the fibres in RVE. This analysis aims at investigating the effect of microscale imperfection on the macroscopic behaviour when considering compressed beams.
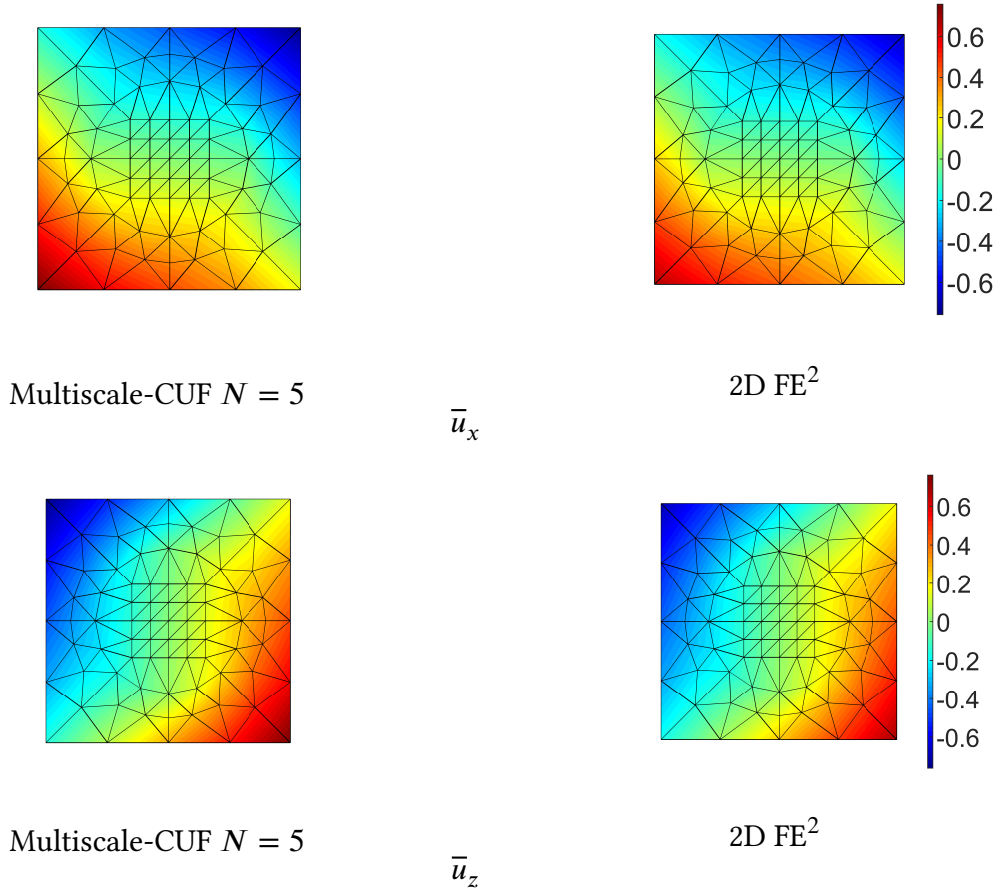
Multiscale-CUF $N = 5$ 2D FE^2

$\overline{u}_x$

Multiscale-CUF $N = 5$ 2D FE^2

$\overline{u}_z$

Figure 6.4: Displacement u_x at $(l, h/2)$ and u_z at $(l, -h/2)$ contour plots in a short can-tilever beam at the last load step.

6.2.1 Post-buckling Analysis

The post-buckling analysis is conducted on fibre-reinforced material to study the instability phenomena triggered by the imperfection in micro-structural level. Both geometrical and material information is known at RVE level. Matrix and fibre material properties are presented in Table 6.5. A square RVE is adopted, where the length L_R is $1\mu m$. Along the middle line ($\eta = 0$) of the RVE, there is a fibre whose height h_f equals to $1/20 L_R$. The geometrical imperfection is introduced as a sinusoidal wave for the fibre, which is shown in a scale-up picture Fig 6.7. Λ represents the wavelength, and A_{max} stands for the amplitude of the imperfection. The amplitude is $1/10 h_f$. Macroscopic geometrical information and boundary condition are presented in Fig 6.8, A very thick beam ($l/h = 5$) is considered along with simply supported boundary conditions. A displacement $\overline{u}_z^*$ is at both ends. Multiscale-CUF and 2D FE^2 models are compared. At the RVE level, Multiscale-CUF and 2D FE^2 models share the same meshes as shown in
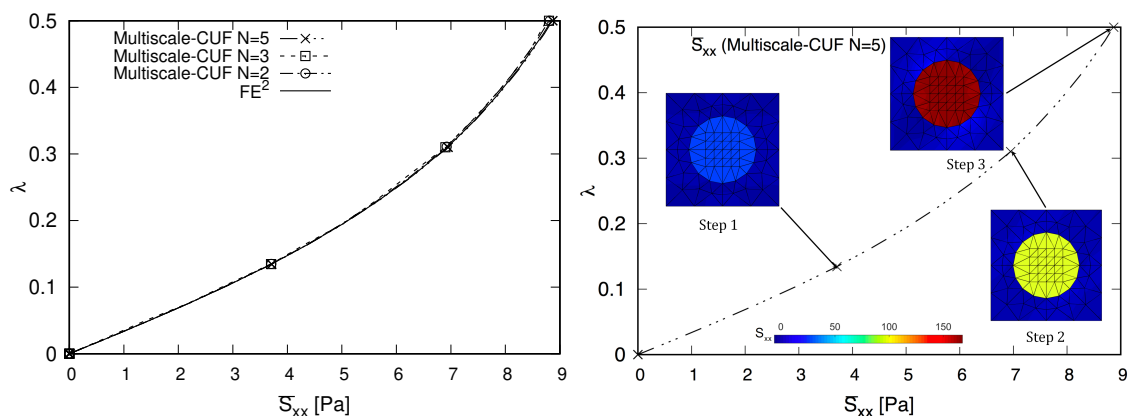
Figure 6.5: Stress $\overline{S}_{xx}$ at $(l/4, -h/2)$ in a short cantilever beam versus load parameter (left). Micro-scale stress contour plots at different load steps for $N = 5$ solution (right).
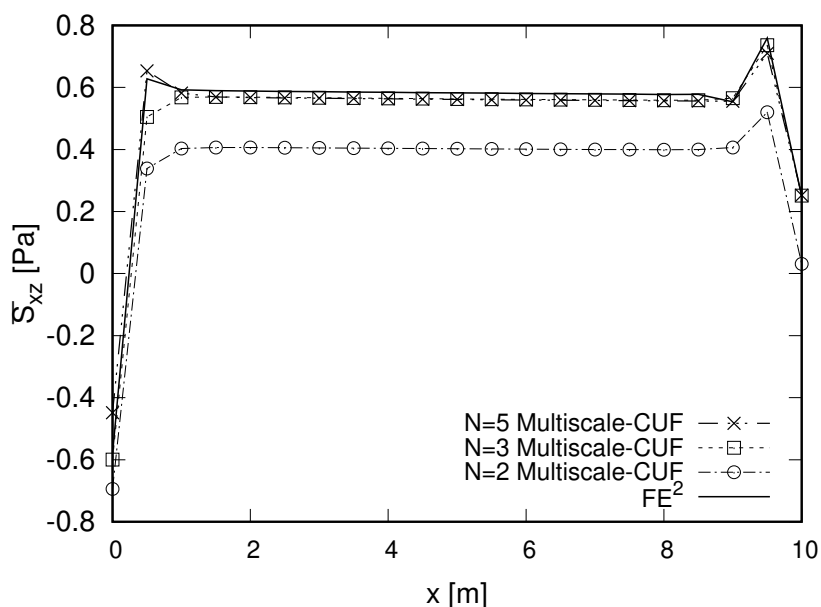

Figure 6.6: Stress $\overline{S}_{xz}$ at $(z/l = 0)$ along the beam axis in a short cantilever beam at last load step.

Fig 6.8. At the structural level, for the FE^2 model, the mesh 20×4 with $Q8$ elements are used. The Multiscale-CUF model has 20 $B3$ beam elements along the axis. Different beam theories are used by changing the expansion order of N.

It is observed that the sinusoidal imperfection in the fibres triggers a macroscopic buckling with two half waves. In Fig 6.9, the displacement field u_z of both the Multiscale-CUF
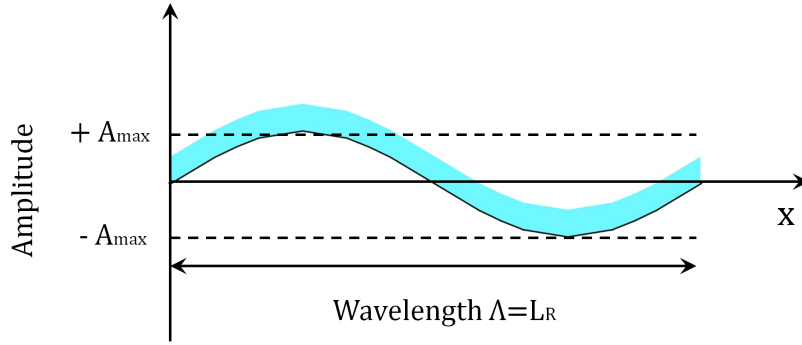
94

Figure 6.7: The schema of the imperfection.

	Matrix	Inclusion
Young Modulus (GPa)	100	100000
Poisson's Ratio	0.3	0.3
Volume Fraction	0.95	0.05

Table 6.5: Material properties of the RVE.

method with $N = 5$ and the 2D FE^2 method are presented for the last step. The displacement fields from those two models compare well with each other. In Fig 6.10, the macroscopic contours for displacement component u_z of the initial state and step 5, 8 and 12 is presented from the Multiscale-CUF model. The results from 2D FE^2 model is the same as the Multiscale-CUF.

Load-displacement curves u_z at ($l/4, -h/2$) and ($3l/4, h/2$) are shown in Fig 6.11. The results for $N \geq 3$ compare well with the reference FE^2 solution. The buckling critical loads predicted from these models are all equal to 0.18. An enlarged picture is illustrated around this point for the sake of clarity. The $N = 5$ result is the closest to the curve from the 2D FE^2 solution. Furthermore, load-stress curves of axial stress $\overline{S}_{xx}$ at ($l/4, h/2$) and ($l/4, -h/2$) are depicted in Figs 6.12. The error between critical buckling load via Multiscale-CUF with $N \geq 4$ and FE^2 is 2.94%.

By plotting out the microscopic displacement and stress fields, buckling phenomena are also found out in the microscale. Thanks to the multi-scale framework, the microscopic response can also be obtained for each step. For points ($l/4, -h/2$) and ($3l/4, h/2$) at last step, two local displacement fields u_z and the global displacement field $\overline{u}_z$ are depicted in Fig 6.13. The maximum value displacement u_z is located near the points ($1/4L_R$, $-1/2h_f$) and ($3/4L_R$, $1/2h_f$). The local stress field S_{xx} at ($l/4, h/2$) and ($l/4, -h/2$) and
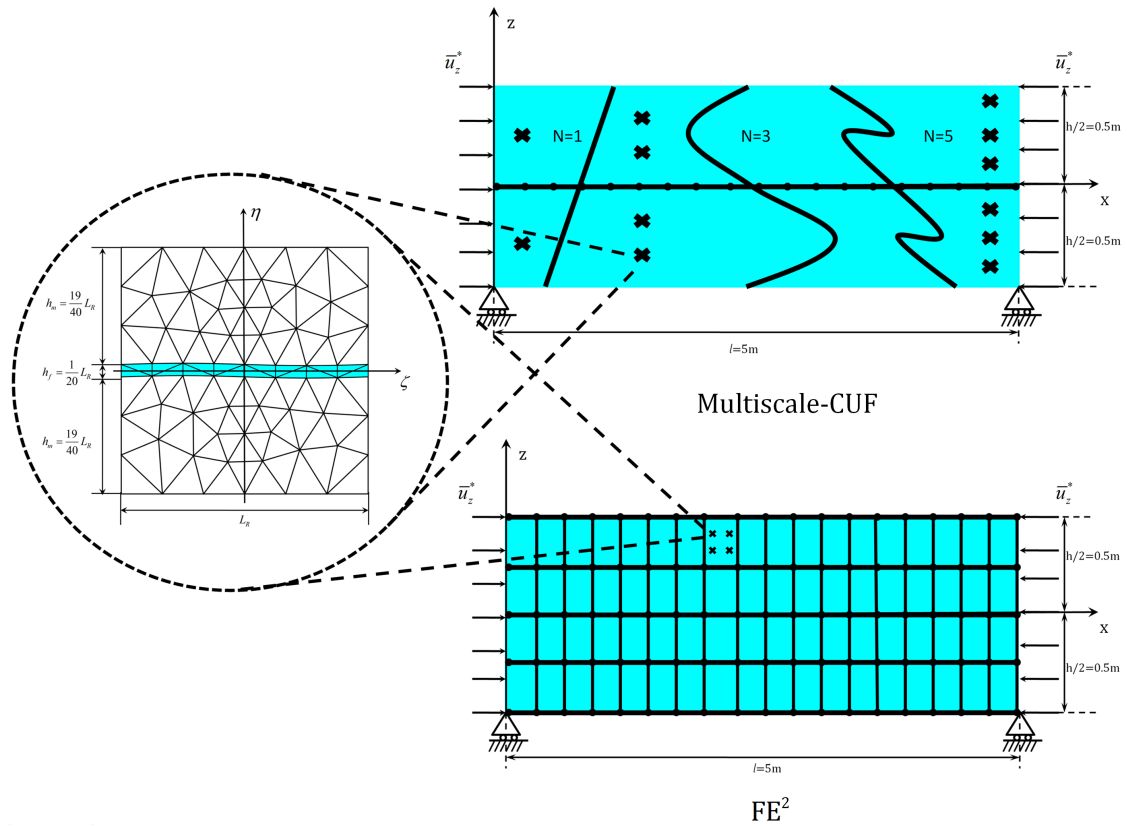
Figure 6.8: Simply-supported beam at the structural level and RVE with fibre inclusion at the microstructural level.

Figure 6.9: Contour of displacement $\bar{u}_z$ for the last step.

global stress field $\overline{S}_{xx}$ at the last step are presented in Fig 6.14. The macroscopic load-stress curve and the contour of microscopic stress fields are displayed in the Figs 6.15 and 6.16 for each step. Fig 6.15 shows that the maximum stress is at $(1/4L_R, 1/2h_f)$. Additionally, Fig 6.16 illustrates that the maximum stress is also at $(1/4L_R, 1/2h_f)$.

A comparison of the results at macroscopic and microscopic scale shows a significant correlation between the scales as illustrated in Fig 6.17, where load-displacement
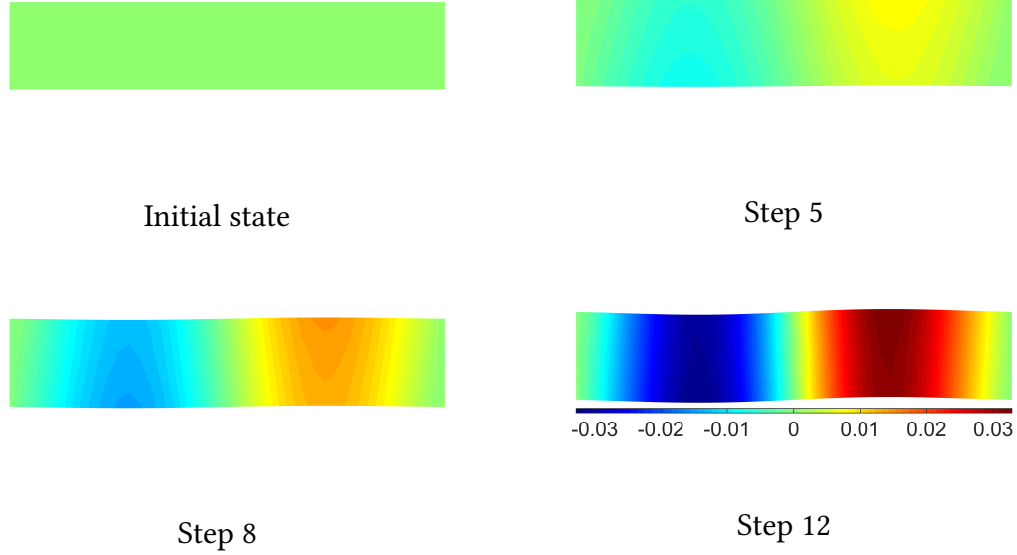
Figure 6.10: Macroscopic displacement field $\overline{u}_z$ for initial state and step 5, 8 and 12.
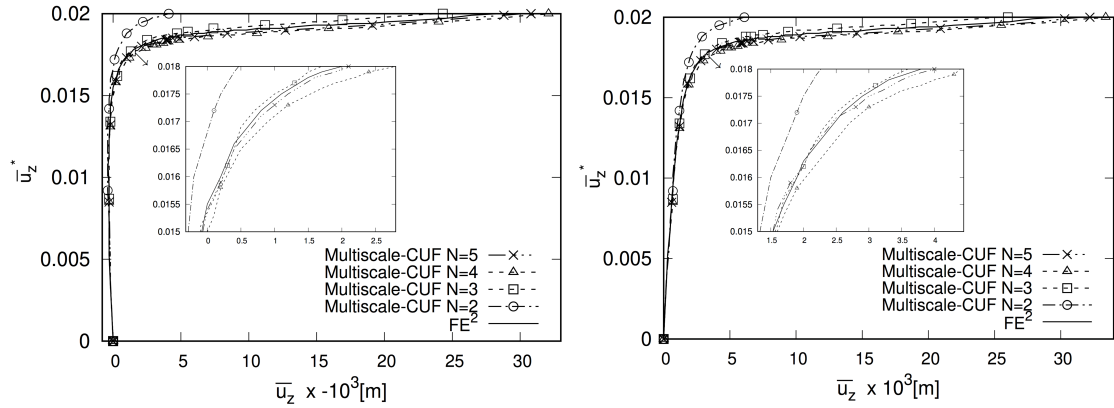

Figure 6.11: Load-displacement curves for $\overline{u}_z$ at $(l/4, -h/2)$ (left) and $(3l/4, h/2)$ (right) in a simply-supported beam ($l/h = 5$).

curves for the macroscopic displacement $\overline{u}_z$ at $(l/4, -h/2)$ and the microscopic displacement u_z at $(L_R/4, h_f/2)$ are depicted on the same picture. The macroscopic load-displacement curve for $\overline{u}_z$ at $(3l/4, h/2)$ and the microscopic load-displacement curve for u_z at $(3L_R/4, -h_f/2)$ are also plotted out on the same picture. Additionally, as shown in Fig 6.18, also load-stress curves for macroscopic stress $\overline{S}_{xx}$ and the microscopic stress S_{xx} are illustrated on the same picture. According to these curves, both the microscopic and macroscopic scale present the same critical buckling load value. This result reveals a synergistic response at both macro and micro scales.
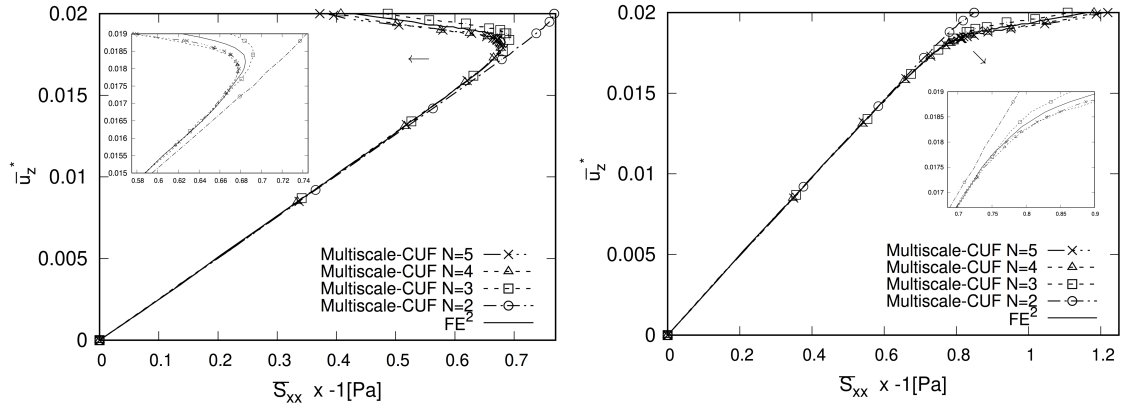
97

Figure 6.12: Load-stress curves for $\overline{S}_{xx}$ at $(l/4, h/2)$ (left) and $(l/4, -h/2)$ (right) in a simply-supported beam $(l/h = 5)$.
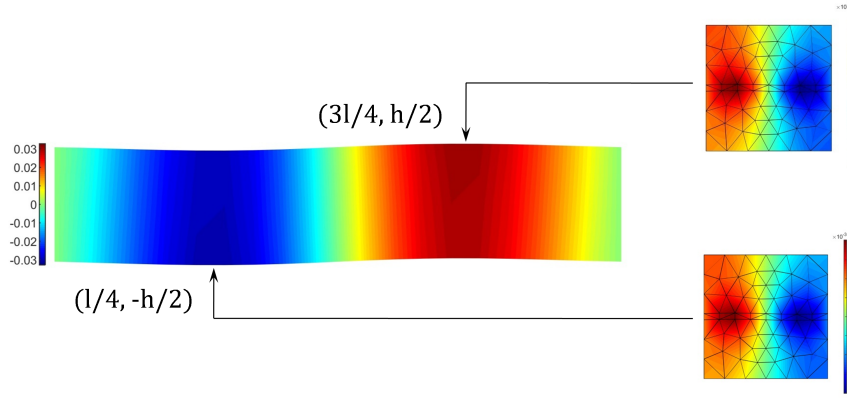

Figure 6.13: Contour plots of the displacement field $\overline{u}_z$ and u_z at $(l/4, -h/2)$ and $(3l/4, h/2)$. Dimension in [m].

6.2.2   Imperfection Sensitivity Analysis

In this section, three factors are studied for the imperfection sensitivity: the wavelength, the amplitude and the size of the RVE. The definitions of wavelength and amplitude are shown in Fig. 6.7.

Wavelength effect A post-buckling analysis is performed for three different values of the wavelength: $\Lambda_1 = \Lambda_0$, $\Lambda_2 = 2\Lambda_0$, and $\Lambda_3 = 3\Lambda_0$, see Fig 6.19. It should be noted that the geometric imperfections are all sinusoidal.

In the region where the bifurcation begins, the longer the wavelength, the sharper the macroscopic load-displacement and load stress curves, see Fig. 6.20. This phenomenon can be explained by the fact that a larger wavelength of the geometric imperfection
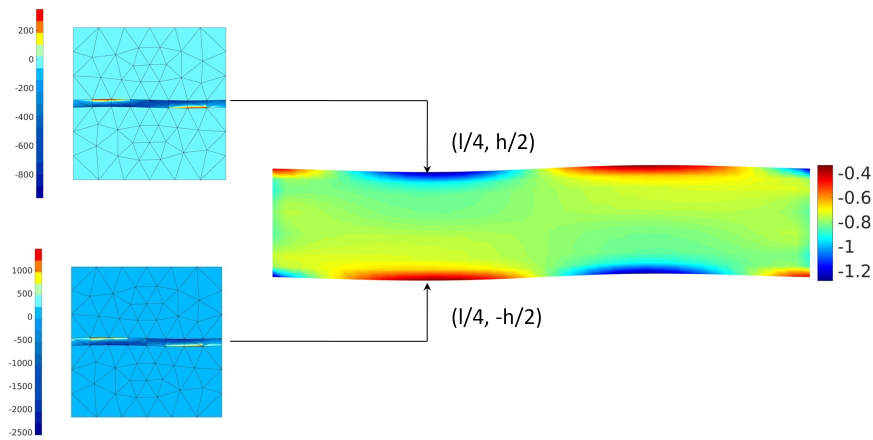
Figure 6.14: Contour plots of stress field $\overline{S}_{xx}$ and S_{xx} at $(l/4, h/2)$ and $(l/4, -h/2)$. Dimension in [Pa].

Figure 6.15: Macroscale axial stress variation versus the load parameter and RVE axial stress contour plots at $(l/4, h/2)$.

produces a smaller macroscopic disturbance. Intuitively, for curves with one cycle of sinusoidal geometric imperfection, the curve with larger wavelengths is flatter. Displacement curves for $\overline{u}_z$ at $(l/4, -h/2)$ are shown in Fig 6.20. The difference among the results starts at $\overline{u}_z^* = 0.06$. Similar results are found for the global variable $\overline{S}_{xz}$ as shown
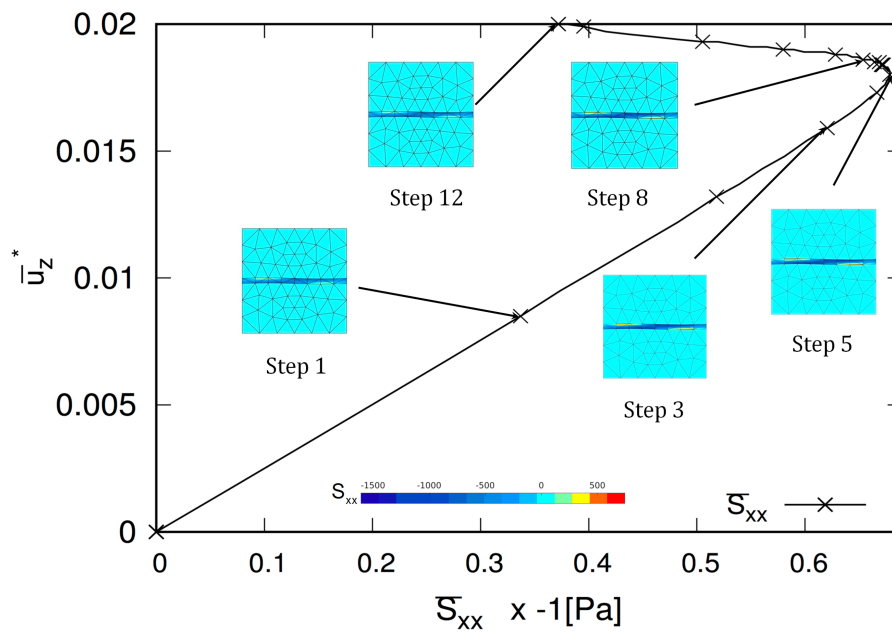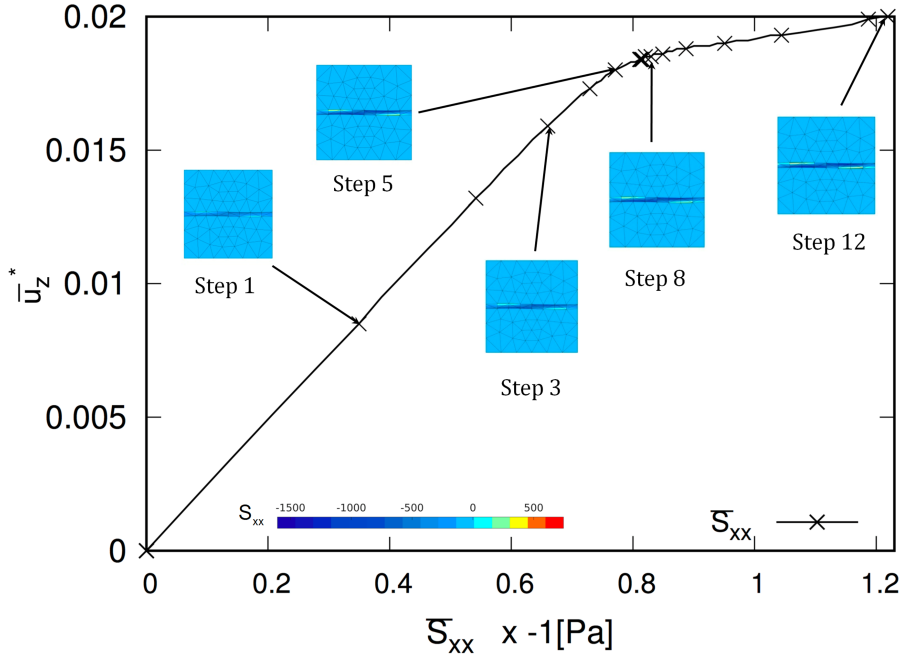
Figure 6.16: Macro-scale axial stress variation versus the load parameter and RVE axial stress contour plots at $(l/4, -h/2)$.
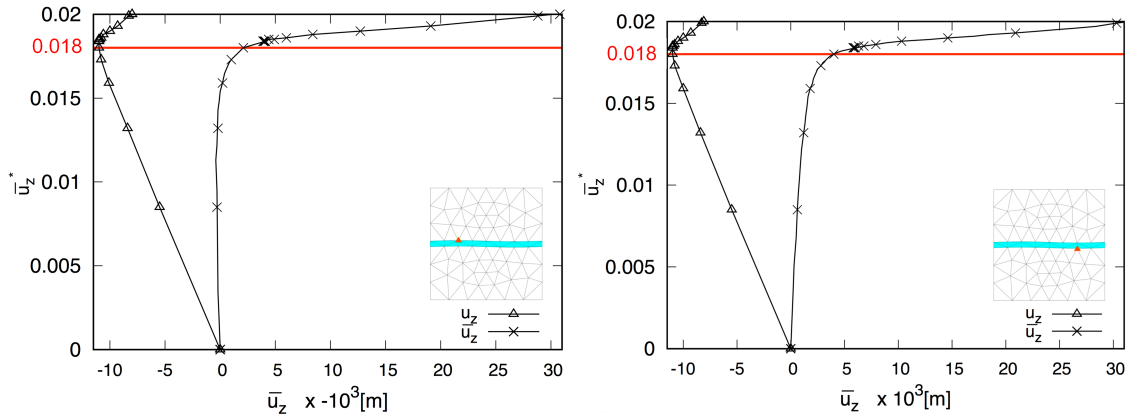
Figure 6.17: Load-displacement curve for $\overline{u}_z$ at $(l/4, -h/2)$ and u_z at $(L_R/4, h_f/2)$ (left) and load-displacement curve $\overline{u}_z$ at $(3l/4, h/2)$ and u_z at $(3L_R/4, -h_f/2)$ (right).

in Fig 6.21.

 Amplitude effect Next, the amplitude of geometric imperfections is investigated. Fig. 6.22 shows the effect of different amplitude values on the axial stress $\overline{S}_{xx}$. A higher amplitude value yields a higher critical load value. In the range of $\overline{u}^* = 0$ to $\overline{u}^* = 0.017$, the three curves are coincident. The curve with amplitude $A_1 = 1.00A_0$ has a critical buckling value $\overline{u}_{cr}^* = 0.0180$, the curve with amplitude $A_2 = 1.05A_0$ has a critical buckling
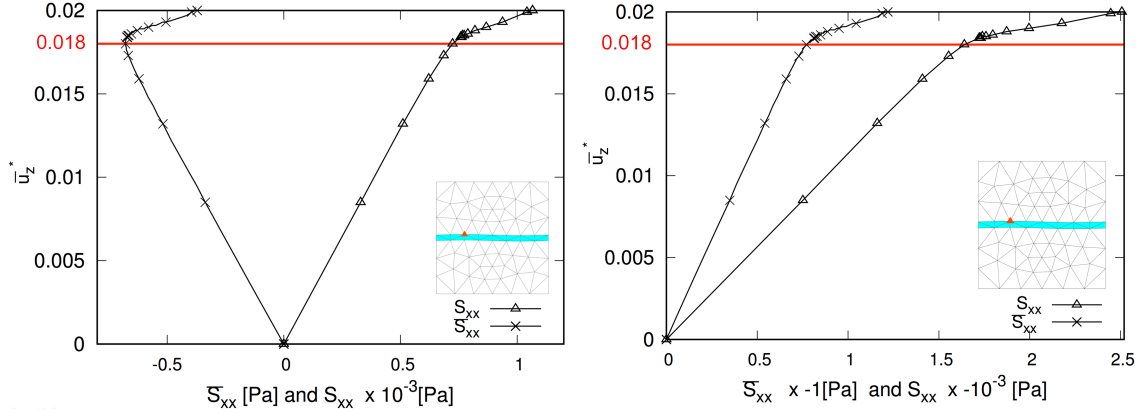
Figure 6.18: Load-stress curve for $\overline{S}_{xx}$ at $(l/4, h/2)$ and S_{xx} at $(L_R/4, h_f/2)$ (left) and load-displacement curve $\overline{S}_{xx}$ at $(l/4, -h/2)$ and S_{xx} at $(L_R/4, h_f/2)$ (right).
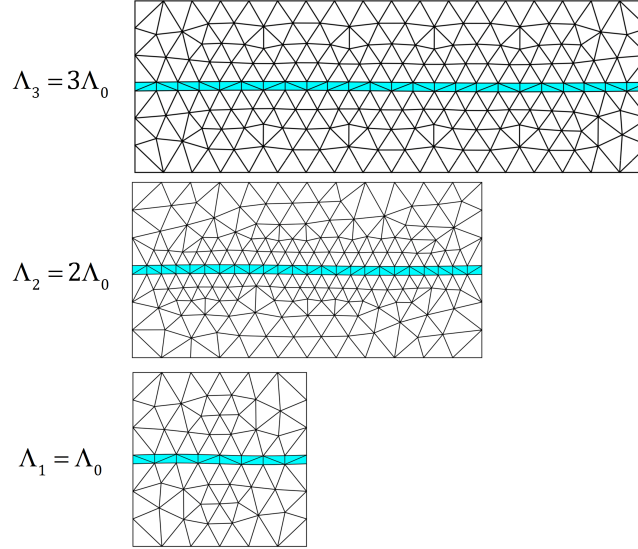
Figure 6.19: Configuration of three RVEs for different imperfection wavelengths.

value $\overline{u}_{cr}^* = 0.0186$, and the curve with amplitude $A_3 = 1.25A_0$ has a critical buckling load of $\overline{u}_{cr}^* = 0.0192$. For shear stress $\overline{S}_{xz}$, Fig 6.23 presents the same tendency. The reason for this result is that: for the same wavelength, a larger amplitude results in a larger fibre/matrix volume ratio. The change in the volume ratio results in a stiffer material.

RVE size effect A key point of the homogenization method is to determine the size of the RVE. A convergence test of macroscopic responses to determine the reasonable size of the RVE is presented in the following.

Three kinds of element (1×1, 2×2, and 3×3) are employed as shown in Fig 6.24. The displacement component $\overline{u}_z$ and shear stress $\overline{S}_{xz}$ are shown in Fig 6.25 and 6.26,

101
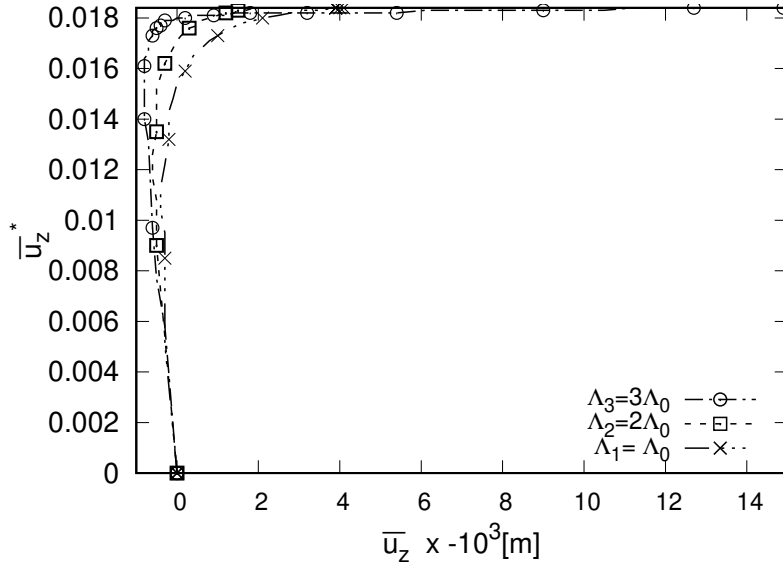
Figure 6.20: Load-displacement curves for $\overline{u}_z$ at ($l/4, -h/2$) in a simply supported beam ($l/h = 5$) with different microscale imperfection wavelengths.
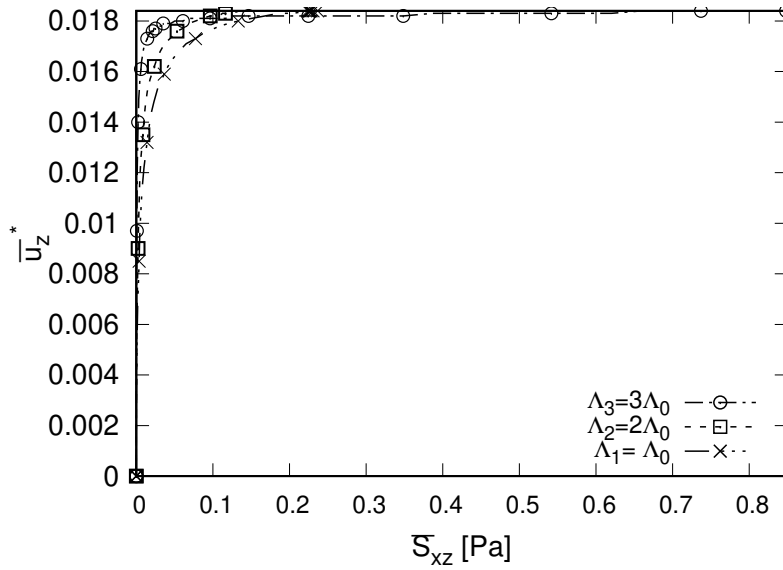
Figure 6.21: Load-stress curves for $\overline{S}_{xz}$ at ($l/2,0$) for a simply supported beam ($l/h = 5$) with different microscale imperfection wavelengths.

respectively.

It can be seen that these three curves share the same instability value. Meanwhile, It is evident that the curve for the 3×3 RVEs is the sharpest one, and the curve of 1×1 RVE is the bluntest one. It was already discussed in Fig. 2.7 that when using periodic boundary conditions, the RVE size influences convergence. In the range from $\overline{u}_z^* = 0$ to
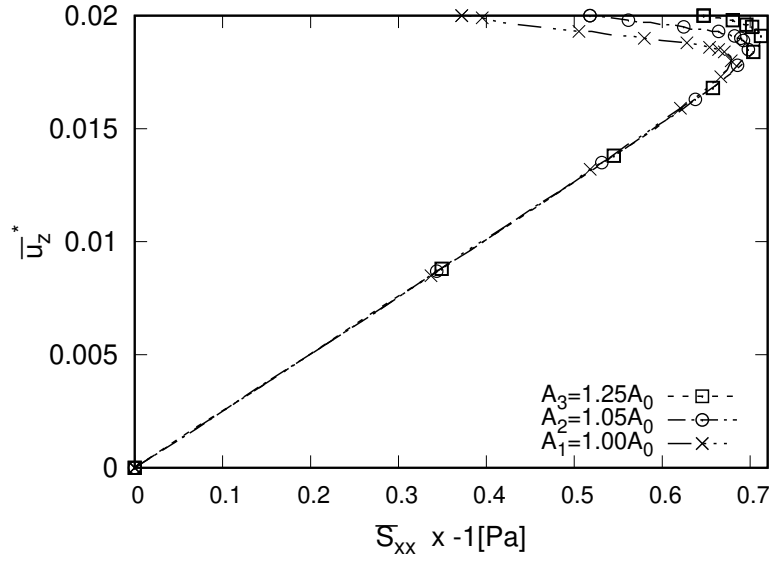
Figure 6.22: Load-stress curves for $\overline{S}_{xx}$ at (l/4, h/2) in simply supported beams ($l/h = 5$) with different microscale imperfection amplitudes.
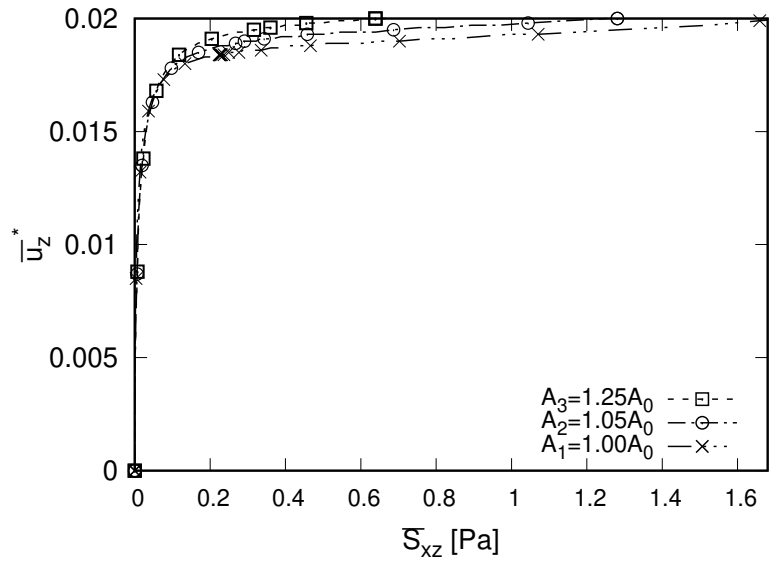
Figure 6.23: Load-stress curves for $\overline{S}_{xz}$ at (l/2,0) in simply supported beams ($l/h = 5$) with different microscale imperfection amplitudes.

$\overline{u}_z^* = 0.01$, three curves are coincident. In the non-linear response, the results of 2×2 RVEs and 3×3 RVEs tend to converge. Although the overall trend of the curve of 1×1 RVE is the same, the results of the bifurcation point and the post-buckling response are significantly different.

3×3

2×2

1×1

Figure 6.24: Considered RVEs.

Figure 6.25: Load-displacement curves for $\overline{u}_z$ at $(l/4, -h/2)$ in simply supported beams ($l/h = 5$) with different RVEs' sizes.
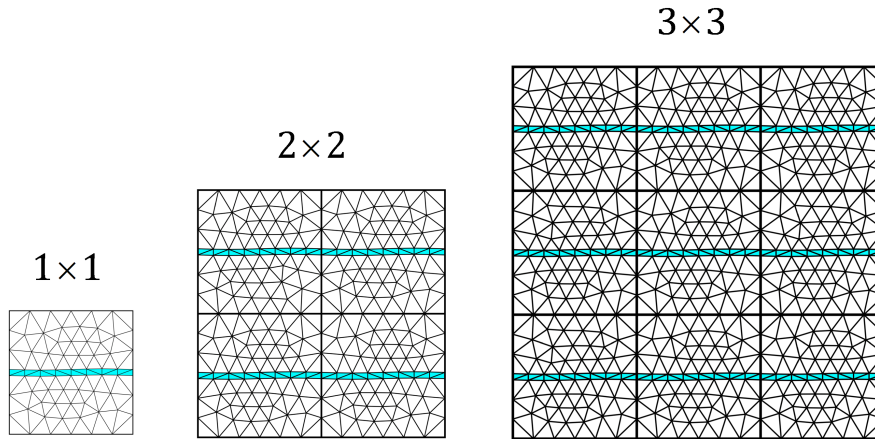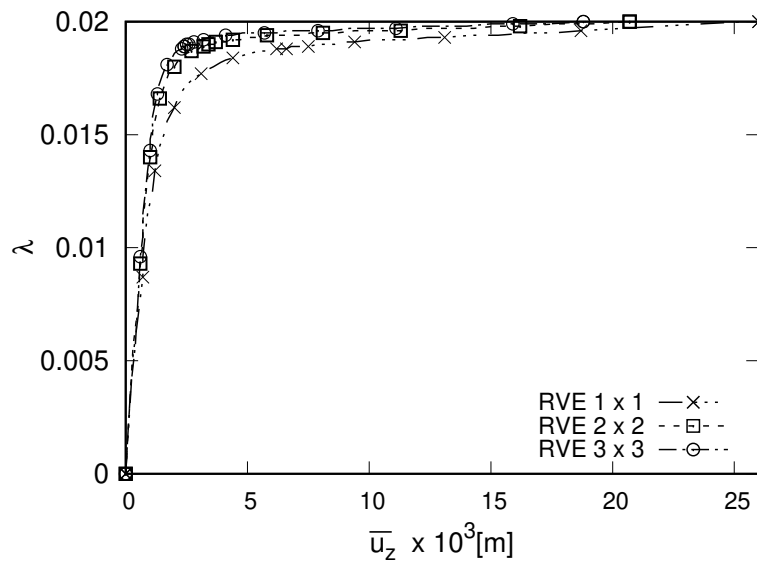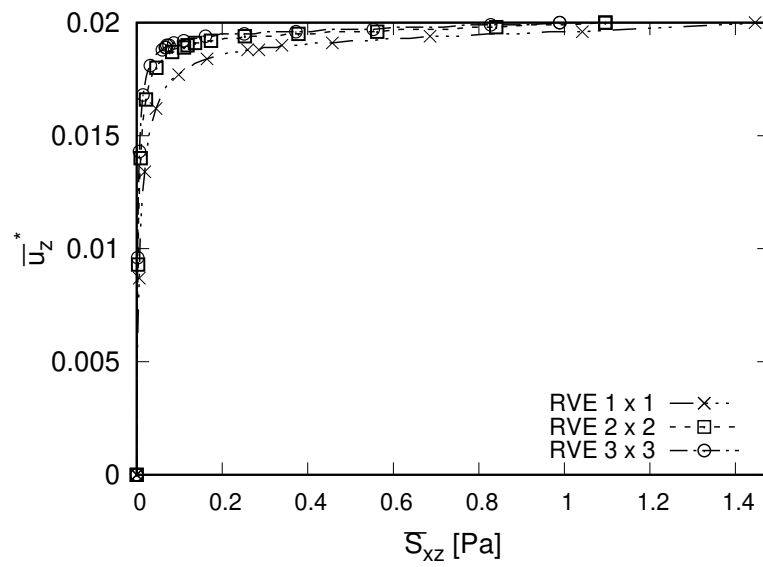
Figure 6.26: Load-stress curves for $\overline{S}_{xz}$ at (l/2,0) in simply supported beams (l/h = 5) with different RVEs' sizes.

Chapter 7

Conclusions and Outlook

7.1 Conclusive Remarks

In this study, a macro-scale non-linear CUF-based beam model and a multi-scale CUF-based beam model have been derived.

For the first time, a hierarchical nonlinear beam model based CUF and the advanced nonlinear solver ANM are coupled. Thanks to CUF, several higher-order beam theories have been derived in a concise and unified form. The computational time has been reduced by up to four times when employing NRM. This model has been employed for the post-buckling and snap-through analyses of beam structures, and the corresponding load-displacement and load-stress curves have been assessed. Results have been compared with two-dimensional FEM solutions. It has been shown that, for the considered cases, a quadratic through-the-thickness description ensures accurate displacements and normal axial stress component. Higher expansion order is required to accurately predict the shear stress component, especially for very high load levels. In the considered post-buckling analysis, both high-order and low-order one-dimensional CUF models have detected the bifurcation point accurately. However, accurate results for the shear stress call for a higher-order model. In the snap-through analysis, a refined beam theory ($N = 5$) is required for tracking the equilibrium path accurately, which is also crucial for determining the initial state of the second stage. Meanwhile, the importance of employing a hierarchical solution has been well shown for conveniently choosing an appropriate approximation order of the cross-sectional displacement field

Then, a geometrically nonlinear CUF-based multi-scale beam model has been derived by coupling the advanced CUF beam model and the nonlinear solver ANM under the FE^2 framework. It is the first known attempt of the extension application of nonlinear CUF-based model to multi-scale problems. Under the framework of FE^2, the introduction of one-dimensional CUF theory has accelerated the resolution of the multi-scale problem without compromising accuracy. It is due to the following two reasons: first, in general in a one-dimensional/beam model, the resulting computational cost is significantly lower than that of a two-dimensional finite element model. Secondly, the number

of microscopic problems is significantly reduced due to the reduction in the number of corresponding RVEs at the Gauss points. Results are compared with reference solutions. Compared to the 2D FE^2 model, the number of degrees of freedom is reduced up to four times. For the fibre-reinforced material case, the relation between the microscopic imperfection and macroscopic instability has been demonstrated thanks to the proposed multiscale nested geometrically nonlinear model. Load-displacement and load-stress curves have been gathered for both microscopic and macroscopic buckling, whose bifurcation points are coincident. Results show that the Multiscale-CUF with $N \geq 4$ and the reference 2D FE^2 compare well. The maximum error between the critical buckling load from these two models is 2.94%. Following this analysis, three factors have been identified for an imperfection sensitivity parametric analysis: imperfection wavelength, imperfection amplitude and the size of RVE. For the wavelength, a higher value induces sharper load-displacement and load-stress curves. The imperfection amplitude has a direct correlation with the value of instability load. The RVE size affects the convergence of nonlinear: 2×2 or 3×3 microstructural arrays for the RVE ensure a better convergence.

7.2   Outlook for Future Research

The current work lays the foundations for future research on advanced one-dimensional models for multi-scale structural mechanics. Not only beam (1D), plate (2D) and shell (2D) elements could also be derived in the multi-scale framework. Concerning further developments inside the multi-scale modelling framework, several improvements can be entailed. First, a second-order homogenisation theory can be employed to generalise the proposed models. Secondly, the component-wise concept based on CUF can be integrated into the presented framework. Finally, this model is limited to address two-dimensional problems. It can be further extended to three-dimensional problems.

Bibliography

[1]   A. Abdulle and B. Engquist. "Finite element heterogeneous multiscale methods with near optimal computational complexity". In: *Multiscale modeling & simulation* 6.4 (2007), pp. 1059–1084.

[2]   J. Aboudi. "A continuum theory for fiber-reinforced elastic-viscoplastic composites". In: *International Journal of Engineering Science* 20.5 (1982), pp. 605–621.

[3]   J. Aboudi. "The generalized method of cells and high-fidelity generalized method of cells micromechanical models—A review". In: *Mechanics of Advanced Materials and Structures* 11.4-5 (2004), pp. 329–366.

[4]   J. Aboudi, M.J. Pindera, and S.M. Arnold. "Higher-order theory for periodic multiphase materials with inelastic phases". In: *International Journal of Plasticity* 19.6 (2003), pp. 805–847.

[5]   K. Attipou, S. Nezamabadi, and H. Zahrouni. "A multiscale approach for the vibration analysis of heterogeneous materials: Application to passive damping". In: *Journal of sound and vibration* 332.4 (2013), pp. 725–739.

[6]   K. Attipou, S. Nezamabadi, and H. Zahrouni. "A multiscale approach for the vibration analysis of heterogeneous materials: Application to passive damping". In: *Journal of sound and vibration* 332.4 (2013), pp. 725–739.

[7]   W.L. Azoti et al. "Mean-field constitutive modeling of elasto-plastic composites using two (2) incremental formulations". In: *Composite Structures* 105 (2013), pp. 256–262.

[8]   I. Babuška. "Homogenization and its application. Mathematical and computational problems". In: *Numerical Solution of Partial Differential Equations–III*. Elsevier, 1976, pp. 89–116.

[9]   E.J. Barbero. *Finite Element Analysis of Composite Materials*. Composite Materials. CRC Press, 2007.

[10]   C. Basaglia and D. Camotim. "Buckling analysis of thin-walled steel structural systems using generalized beam theory (GBT)". In: *International Journal of Structural Stability and Dynamics* 15.01 (2015), p. 1540004.

[11] K.J. Bathe. "Finite element method". In: *Wiley encyclopedia of computer science and engineering* (2007), pp. 1–12.

[12] J.L. Batoz and G. Dhatt. "Incremental displacement algorithms for nonlinear problems". In: *International Journal for Numerical Methods in Engineering* 14.8 (1979), pp. 1262–1267.

[13] A. Bensoussan et al. *Asymptotic analysis of periodic structures*. 1979.

[14] V.L. Berdichevsky. "Variational-asymptotic method of shell theory construction". In: *PMM* 43.4 (1979), pp. 664–687.

[15] P.G. Bergan et al. "Solution techniques for non-linear finite element problems". In: *International Journal for Numerical Methods in Engineering* 12.11 (1978), pp. 1677–1696.

[16] D.P. Boso, M. Lefik, and B.A. Schrefler. "A multilevel homogenised model for superconducting strand thermomechanics". In: *Cryogenics* 45.4 (2005), pp. 259–271.

[17] M.L. Bucalem and K.J. Bathe. "Higher-order MITC general shell elements". In: *International Journal for Numerical Methods in Engineering* 36.21 (1993), pp. 3729–3754.

[18] B. Budiansky. "On the elastic moduli of some heterogeneous materials". In: *Journal of the Mechanics and Physics of Solids* 13.4 (1965), pp. 223–227.

[19] E. Carrera. "A study on arc-length-type methods and their operation failures illustrated by a simple model". In: *Computers & Structures* 50.2 (1994), pp. 217–229.

[20] E. Carrera. "Theories and finite elements for multilayered, anisotropic, composite plates and shells". In: *Archives of Computational Methods in Engineering* 9.2 (2002), pp. 87–140.

[21] E. Carrera and A. Ciuffreda. "A unified formulation to assess theories of multilayered plates for various bending problems". In: *Composite Structures* 69.3 (2005), pp. 271–293.

[22] E. Carrera and L. Demasi. "Two benchmarks to assess two-dimensional theories of sandwich, composite plates". In: *AIAA journal* 41.7 (2003), pp. 1356–1362.

[23] E. Carrera, F.A. Fazzolari, and M. Cinefra. *Thermal Stress Analysis of Composite Beams, Plates and Shells: Computational Modelling and Applications*. Academic Press, 2016.

[24] E. Carrera and G. Giunta. "Exact, hierarchical solutions for localized loadings in isotropic, laminated, and sandwich shells". In: *Journal of Pressure Vessel Technology* 131.4 (2009), p. 041202.

[25] E. Carrera and G. Giunta. "Refined Beam Theories based on a Unified Formulation". In: *International Journal of Applied Mechanics* 2.1 (2010), pp. 117–143.

110

[26] E. Carrera, G. Giunta, and M. Petrolo. *Beam Structures: Classical and Advanced Theories*. Wiley-Blackwell, 2011.

[27] E. Carrera, A.G. de Miguel, and A. Pagani. "Hierarchical theories of structures based on Legendre polynomial expansions with finite element applications". In: *International Journal of Mechanical Sciences* 120 (2017), pp. 286–300.

[28] E. Carrera et al. "A refined 1D element for the structural analysis of single and multiple fiber/matrix cells". In: *Composite Structures* 96 (2013), pp. 455–468.

[29] E. Carrera et al. "Higher order beam finite elements with only displacement degrees of freedom". In: *Proceedings of the XIX Conference of Italian Association of Applied and Theoretic Mechanics (AIMETA), Ancona, Italy, September*. 2009, pp. 14–17.

[30] E Carrera, A.G. de Miguel, and A. Pagani. "Extension of MITC to higher-order beam models and shear locking analysis for compact, thin-walled, and composite structures". In: *International Journal for Numerical Methods in Engineering* 112.13 (2017), pp. 1889–1908.

[31] C.E.S. Cesnik and D.H. Hodges. "VABS: a new concept for composite rotor blade cross-sectional modeling". In: *Journal of the American helicopter society* 42.1 (1997), pp. 27–38.

[32] J.L. Chaboche et al. "Towards a micromechanics based inelastic and damage modeling of composites". In: *International Journal of Plasticity* 17.4 (2001), pp. 411–439.

[33] R. Chiu. "Third Order GBT Terms And Its Expression". In: *The Twenty-second International Offshore and Polar Engineering Conference*. International Society of Offshore and Polar Engineers. 2012.

[34] J. Chu et al. "Flow based oversampling technique for multiscale finite element methods". In: *Advances in Water Resources* 31.4 (2008), pp. 599–608.

[35] B. Cochelin, N. Damil, and M. Potier-Ferry. *Méthode asymptotique numérique*. Hermes Lavoissier, 2007.

[36] G.R. Cowper. "The shear coefficient in Timoshenko's beam theory". In: *Journal of applied mechanics* 33.2 (1966), pp. 335–340.

[37] M. A. Crisfield. *Non-linear finite element analysis of solids and structures*. Vol. 1. Chichester, England: John Wiley and Sons, 1991.

[38] M.A. Crisfield. "A fast incremental/iterative solution procedure that handles "snap-through"". In: *Computational Methods in Nonlinear Structural and Solid Mechanics*. Elsevier, 1981, pp. 55–62.

[39] M. D'Ottavio and E. Carrera. "Variable-kinematics approach for linearized buckling analysis of laminated plates and shells". In: *AIAA journal* 48.9 (2010), pp. 1987–1996.

[40] M. D'Ottavio et al. "A Sublaminate Generalized Unified Formulation for buckling and wrinkling of sandwich plates". In: *EMI International Conference 2016*. 2016.

[41] M. D'Ottavio. "A Sublaminate Generalized Unified Formulation for the analysis of composite structures". In: *Composite Structures* 142 (2016), pp. 187–199.

[42] N. Damil and M. Potier-Ferry. "A new method to compute perturbed bifurcations: application to the buckling of imperfect elastic structures". In: *International Journal of Engineering Science* 28.9 (1990), pp. 943–957.

[43] J.M. Davies and P. Leach. "First-order generalised beam theory". In: *Journal of Constructional Steel Research* 31.2-3 (1994), pp. 187–220.

[44] J.M. Davies, P. Leach, and D. Heinz. "Second-order generalised beam theory". In: *Journal of Constructional Steel Research* 31.2-3 (1994), pp. 221–241.

[45] L. Demasi. "∞^3 Hierarchy plate theories for thick and thin composite plates: the generalized unified formulation". In: *Composite Structures* 84.3 (2008), pp. 256–270.

[46] G. Dhondt. *The finite element method for three-dimensional thermomechanical applications*. John Wiley & Sons, 2004.

[47] P.B. Dinis, D. Camotim, and N.G. Silvestre. "GBT formulation to analyse the buckling behaviour of thin-walled members with arbitrarily 'branched' open cross-sections". In: *Thin-Walled Structures* 44.1 (2006), pp. 20–38.

[48] S.B. Dong, J.B. Kosmatka, and H.C. Lin. "On Saint-Venant's problem for an inhomogeneous, anisotropic cylinder—Part I: Methodology for Saint-Venant solutions". In: *Journal of Applied Mechanics* 68.3 (2001), pp. 376–381.

[49] G.J. Dvorak and M.S.M. Rao. "Axisymmetric plasticity theory of fibrous composites". In: *International Journal of Engineering Science* 14.4 (1976), pp. 361–373.

[50] A.V. Dyskin. "Effective characteristics and stress concentrations in materials with self-similar microstructure". In: *International Journal of Solids and Structures* 42.2 (2005), pp. 477–502.

[51] W. E and B. Engquist. "The heterognous multiscale methods". In: *Communications in Mathematical Sciences* 1.1 (2003), pp. 87–132.

[52] W. E and J. Lu. "Multiscale modeling". In: *Scholarpedia* 6.10 (2011), p. 11527.

[53] W. E and Y.X. Yue. "Heterogeneous multiscale method for locally self-similar problems". In: *Commun Math Sci (1)* (2004), pp. 137–144.

[54] Y. Efendiev and T.Y. Hou. *Multiscale finite element methods: theory and applications*. Vol. 4. Springer Science & Business Media, 2009.

[55] M. El Hachemi et al. "An intuitive computational multi-scale methodology and tool for the dynamic modelling of viscoelastic composites and structures". In: *Composite Structures* 144 (2016), pp. 131–137.

[56] A. Eriksson and R. Kouhia. "On step size adjustments in structural continuation problems". In: *Computers & structures* 55.3 (1995), pp. 495–506.

[57] J.D. Eshelby. "The elastic field outside an ellipsoidal inclusion". In: *Proceedings of the Royal Society of London A: Mathematical, Physical and Engineering Sciences*. Vol. 252. 1271. The Royal Society. 1959, pp. 561–569.

[58] C. Farhat, I. Harari, and L.P. Franca. "The discontinuous enrichment method". In: *Computer methods in applied mechanics and engineering* 190.48 (2001), pp. 6455–6479.

[59] C. Farhat, R. Tezaur, and P. Weidemann-Goiran. "Higher-order extensions of a discontinuous Galerkin method for mid-frequency Helmholtz problems". In: *International journal for numerical methods in engineering* 61.11 (2004), pp. 1938–1956.

[60] F. Feyel and J.L. Chaboche. "FE^2 multiscale approach for modelling the elasto-viscoplastic behaviour of long fibre SiC/Ti composite materials". In: *Computer methods in applied mechanics and engineering* 183.3 (2000), pp. 309–330.

[61] M. Filippi et al. "Static and free vibration analysis of laminated beams by refined theory based on Chebyshev polynomials". In: *Composite Structures* 132 (2015), pp. 1248–1259.

[62] J. Fish. *Multiscale methods: bridging the scales in science and engineering*. Oxford University Press on Demand, 2010.

[63] J. Fish. *Practical multiscaling*. John Wiley & Sons, 2013.

[64] J. Fish and Q. Yu. "Computational mechanics of fatigue and life predictions for composite materials and structures". In: *Computer methods in applied mechanics and engineering* 191.43 (2002), pp. 4827–4849.

[65] J. Fish and Z. Yuan. "Multiscale enrichment based on partition of unity". In: *International Journal for Numerical Methods in Engineering* 62.10 (2005), pp. 1341–1359.

[66] J. Fish and Z. Yuan. "Multiscale enrichment based on partition of unity for non-periodic fields and nonlinear problems". In: *Computational Mechanics* 40.2 (2007), pp. 249–259.

[67] J. Fish et al. "Computational plasticity for composite structures based on mathematical homogenization: Theory and practice". In: *Computer Methods in Applied Mechanics and Engineering* 148.1-2 (1997), pp. 53–73.

[68] M.G.D. Geers, V. Kouznetsova, and W.A.M. Brekelmans. "Gradient-enhanced computational homogenization for the micro-macro scale transition". In: *Le Journal de Physique IV* 11.PR5 (2001), Pr5–145.

[69] M.G.D. Geers et al. "Computational homogenization of structures and materials". In: *Proceedings of the 9th Neuvième Colloque National en Calcul des Structures, Giens, France.* 2009, pp. 17–28.

[70] S. Ghosh, K. Lee, and S. Moorthy. "Two scale analysis of heterogeneous elastic-plastic materials with asymptotic homogenization and Voronoi cell finite element model". In: *Computer methods in applied mechanics and engineering* 132.1-2 (1996), pp. 63–116.

[71] S. Ghosh and Y. Liu. "Voronoi cell finite element model based on micropolar theory of thermoelasticity for heterogeneous materials". In: *International journal for numerical methods in engineering* 38.8 (1995), pp. 1361–1398.

[72] S. Ghosh and R.L. Mallett. "Voronoi cell finite elements". In: *Computers & Structures* 50.1 (1994), pp. 33–46.

[73] S. Ghosh and P. Raghavan. "Multiscale model for damage analysis in fiber-reinforced composites with interfacial debonding". In: *International Journal for Multiscale Computational Engineering* 2.4 (2004).

[74] G Giunta. "Deterministic and stochastic hierarchical analysis of failure and vibration of composite plates and shells". PhD thesis. PhD Thesis, Politecnico di Torino, 2008.

[75] G. Giunta et al. "Hierarchical modelling of doubly curved laminated composite shells under distributed and localised loadings". In: *Composites Part B: Engineering* 42.4 (2011), pp. 682–691.

[76] G. Giunta et al. "Newton's series expansion based theories in the framework of Carrera's unified formulation for the analysis of plates". In: *First International Conference on Mechanics of Advanced Materials and Structures, Proceedings.* Vol. 72. 2018.

[77] V. Gravemeier. *The variational multiscale method for laminar and turbulent incompressible flow.* 2003.

[78] R.M.J. Groh and A. Pirrera. "Generalised path-following for well-behaved nonlinear structures". In: *Computer Methods in Applied Mechanics and Engineering* 331 (2018), pp. 394–426.

[79] Q.Z. He et al. "Multi-scale modelling of sandwich structures using hierarchical kinematics". In: *Composite Structures* 93.9 (2011), pp. 2375–2383.

[80] R. Hill. "A self-consistent mechanics of composite materials". In: *Journal of the Mechanics and Physics of Solids* 13.4 (1965), pp. 213–222.

[81] R. Hill. "Elastic properties of reinforced solids: some theoretical principles". In: *Journal of the Mechanics and Physics of Solids* 11.5 (1963), pp. 357–372.

[82] R. Hill. "The elastic behaviour of a crystalline aggregate". In: *Proceedings of the Physical Society. Section A* 65.5 (1952), p. 349.

[83] D.H. Hodges. *Nonlinear composite beam theory*. American Institute of Aeronautics and Astronautics, 2006.

[84] T.Y. Hou and X.H. Wu. "A multiscale finite element method for elliptic problems in composite materials and porous media". In: *Journal of computational physics* 134.1 (1997), pp. 169–189.

[85] T.Y. Hou, X.H. Wu, and Z. Cai. "Convergence of a multiscale finite element method for elliptic problems with rapidly oscillating coefficients". In: *Mathematics of Computation of the American Mathematical Society* 68.227 (1999), pp. 913–943.

[86] H. Hu, S. Belouettar, and M. Potier-Ferry. "Multi-scale modelling of sandwich structures using the Arlequin method Part I: Linear modelling". In: *Finite Elements in Analysis and Design* 45.1 (2008), pp. 37–51.

[87] H. Hu, N. Damil, and M. Potier-Ferry. "A bridging technique to analyze the influence of boundary conditions on instability patterns". In: *Journal of computational physics* 230.10 (2011), pp. 3753–3764.

[88] H. Hu et al. "A novel finite element for global and local buckling analysis of sandwich beams". In: *Composite Structures* 90.3 (2009), pp. 270–278.

[89] H. Hu et al. "Review and assessment of various theories for modeling sandwich composites". In: *Composite Structures* 84.3 (2008), pp. 282–292.

[90] Q. Huang et al. "A Fourier-related double scale analysis on the instability phenomena of sandwich plates". In: *Computer Methods in Applied Mechanics and Engineering* 318 (2017), pp. 270–295.

[91] Q. Huang et al. "A new Fourier-related double scale analysis for wrinkling analysis of thin films on compliant substrates". In: *Composite Structures* 160 (2017), pp. 613–624.

[92] W. Huang et al. "A Fourier based reduced model for wrinkling analysis of circular membranes". In: *Computer Methods in Applied Mechanics and Engineering* (2018).

[93] C. Huet. "Universal conditions for assimilation of a heterogeneous material to an effective continuum". In: *Mechanics research communications* 9.3 (1982), pp. 165–170.

[94] T.J.R. Hughes et al. "The variational multiscale method—a paradigm for computational mechanics". In: *Computer methods in applied mechanics and engineering* 166.1-2 (1998), pp. 3–24.

115

[95]   J.W. Hutchinson. "Buckling and initial postbuckling behavior of oval cylindrical shells under axial compression". In: *Journal of Applied Mechanics* 35.1 (1968), pp. 66–72.

[96]   J.W. Hutchinson and W.T. Koiter. "Postbuckling theory". In: *Appl. Mech. Rev* 23.12 (1970), pp. 1353–1366.

[97]   D. Ieşan. "On Saint-Venant's problem". In: *Archive for Rational Mechanics and Analysis* 91.4 (1986), pp. 363–373.

[98]   C.H. Jochum and J.C. Grandidier. "Microbuckling elastic modelling approach of a single carbon fibre embedded in an epoxy matrix". In: *Composites science and technology* 64.16 (2004), pp. 2441–2449.

[99]   I. Kaleel et al. "Micromechanical Progressive Failure Analysis of Fiber-Reinforced Composite Using Refined Beam Models". In: *Journal of Applied Mechanics* 85.2 (2018), p. 021004.

[100]   T. Kanit et al. "Determination of the size of the representative volume element for random composites: statistical and numerical approach". In: *International Journal of solids and structures* 40.13 (2003), pp. 3647–3679.

[101]   P. Kanouté et al. "Multiscale methods for composites: a review". In: *Archives of Computational Methods in Engineering* 16.1 (2009), pp. 31–75.

[102]   R.K. Kapania and S. Raciti. "Recent advances in analysis of laminated beams and plates. Part I-Sheareffects and buckling." In: *AIAA journal* 27.7 (1989), pp. 923–935.

[103]   B. Klusemann and B. Svendsen. "Homogenization methods for multi-phase elastic composites: Comparisons and benchmarks". In: *Technische Mechanik* 30.4 (2010), pp. 374–386.

[104]   W.T. Koiter. *The stability of elastic equilibrium*. Tech. rep. STANFORD UNIV CA DEPT OF AERONAUTICS and ASTRONAUTICS, 1970.

[105]   Y. Koutsawa, I. Charpentier, and M. Cherkaoui. "A generic approach for the solution of nonlinear residual equations. Part I: The Diamant toolbox". In: *Computer Methods in Applied Mechanics and Engineering* 198.3-4 (2008), pp. 572–577.

[106]   V.G. Kouznetsova, M.G.D. Geers, and W.A.M. Brekelmans. "Multi-scale second-order computational homogenization of multi-phase materials: a nested finite element solution strategy". In: *Computer Methods in Applied Mechanics and Engineering* 193.48 (2004), pp. 5525–5550.

[107]   P. Ladevèze, P. Sanchez, and J. Simmonds. "Beamlike (Saint–Venant) solutions for fully anisotropic elastic tubes of arbitrary closed cross section". In: *International Journal of Solids and Structures* 41.7 (2004), pp. 1925–1944.

[108] P. Ladevèze and J. Simmonds. "New concepts for linear beam theory with arbitrary geometry and loading". In: *European Journal of Mechanics-A/Solids* 17.3 (1998), pp. 377–402.

[109] W.F. Lam and C.T. Morley. "Arc-length method for passing limit points in structural calculation". In: *Journal of structural engineering* 118.1 (1992), pp. 169–185.

[110] D. Lanc et al. "Buckling analysis of thin-walled functionally graded sandwich box beams". In: *Thin-Walled Structures* 86 (2015), pp. 148–156.

[111] A.D. Lanzo and G. Garcea. "Koiter's analysis of thin-walled structures by a finite element approach". In: *International Journal for Numerical Methods in Engineering* 39.17 (1996), pp. 3007–3031.

[112] M. Lefik and B. Schrefler. "Modelling of nonstationary heat conduction problems in micro-periodic composites using homogenisation theory with corrective terms". In: *Arch. Mech.* 52.2 (2000), pp. 203–223.

[113] Y. Liu et al. "A robust Riks-like path following method for strain-actuated snap-through phenomena in soft solids". In: *Computer Methods in Applied Mechanics and Engineering* 323 (2017), pp. 416–438.

[114] M. Maiarú, M. Petrolo, and E. Carrera. "Evaluation of energy and failure parameters in composite structures via a component-wise approach". In: *Composites Part B: Engineering* 108 (2017), pp. 53–64.

[115] J. Mandel. "Contribution théorique à l'étude de l'écrouissage et des lois de l'écoulement plastique". In: *Applied Mechanics*. Springer, 1966, pp. 502–509.

[116] P. Marcellini. "Periodic solutions and homogenization of non linear variational problems". In: *Annali di matematica pura ed applicata* 117.1 (1978), pp. 139–152.

[117] K. Matouš et al. "A review of predictive nonlinear theories for multiscale modeling of heterogeneous materials". In: *Journal of Computational Physics* 330 (2017), pp. 192–220.

[118] K. Matsui, K. Terada, and K. Yuge. "Two-scale finite element analysis of heterogeneous solids with periodic microstructures". In: *Computers & Structures* 82.7 (2004), pp. 593–606.

[119] M. Mattea, M.J. Urbicain, and E. Rotstein. "Computer model of shrinkage and deformation of cellular tissue during dehydration". In: *Chemical engineering science* 44.12 (1989), pp. 2853–2859.

[120] J.C. Michel and P. Suquet. "Nonuniform transformation field analysis". In: *International journal of solids and structures* 40.25 (2003), pp. 6937–6955.

[121] J.H. Michell. "The theory of uniformly loaded beams". In: *Quart. J. Math* 32 (1901), pp. 28–42.

[122] C. Miehe, J. Schröder, and J. Schotte. "Computational homogenization analysis in finite plasticity simulation of texture development in polycrystalline materials". In: *Computer methods in applied mechanics and engineering* 171.3 (1999), pp. 387–418.

[123] A.G. de Miguel et al. "Micromechanics of periodically heterogeneous materials using higher-order beam theories and the mechanics of structure genome". In: *Composite Structures* 180 (2017), pp. 484–496.

[124] R.D. Mindlin and H. Deresiewicz. *Timoshenko's shear coefficient for flexural vibrations of beams.* Tech. rep. COLUMBIA UNIV NEW YORK, 1953.

[125] T. Mori and K. Tanaka. "Average stress in matrix and average elastic energy of materials with misfitting inclusions". In: *Acta metallurgica* 21.5 (1973), pp. 571–574.

[126] A. Najah et al. "A critical review of asymptotic numerical methods". In: *Archives of Computational Methods in Engineering* 5.1 (1998), pp. 31–50.

[127] S. Nemat-Nasser and M. Taya. "On effective moduli of an elastic body containing periodically distributed voids". In: *Quarterly of Applied Mathematics* 39.1 (1981), pp. 43–59.

[128] S. Nemat-Nasser, N. Yu, and M. Hori. "Solids with periodically distributed cracks". In: *International Journal of Solids and Structures* 30.15 (1993), pp. 2071–2095.

[129] S. Nezamabadi. "Méthode Asymptotique Numérique pour l'étude multi échelle des instabilités dans les matériaux hétérogenes". PhD thesis. Université Paul Verlaine Metz, 2009.

[130] S. Nezamabadi et al. "A multilevel computational strategy for handling microscopic and macroscopic instabilities". In: *Computer Methods in Applied Mechanics and Engineering* 198.27 (2009), pp. 2099–2110.

[131] S. Nezamabadi et al. "A multiscale finite element approach for buckling analysis of elastoplastic long fiber composites". In: *International Journal for Multiscale Computational Engineering* 8.3 (2010).

[132] S. Nezamabadi et al. "Compressive failure of composites: A computational homogenization approach". In: *Composite Structures* 127 (2015), pp. 60–68.

[133] A.K. Noor and J.M. Peters. "Reduced basis technique for nonlinear analysis of structures". In: *Aiaa journal* 18.4 (1980), pp. 455–462.

[134] A. Pagani. "Strong-form governing equations and solutions for variable kinematic beam theories with practical applications". PhD thesis. City, University of London, 2016.

[135] A. Pagani and E. Carrera. "Unified formulation of geometrically nonlinear refined beam theories". In: *Mechanics of Advanced Materials and Structures* (2017), pp. 1–17.

[136] G. Petrone et al. "Behaviour of fibre-reinforced honeycomb core under low velocity impact loading". In: *Composite Structures* 100 (2013), pp. 356–362.

[137] D.V. Phillips and O.C. Zienkiewicz. "Finite element non-linear analysis of concrete structures". In: *Institution of Civil Engineers, Proceedings*. Vol. 61. 1976.

[138] E.J. Pineda et al. "Progressive failure of a unidirectional fiber-reinforced composite using the method of cells: discretization objective computational results". In: *International Journal of Solids and Structures* 50.9 (2013), pp. 1203–1216.

[139] T. Rahman and E.L. Jansen. "Finite element based coupled mode initial postbuckling analysis of a composite cylindrical shell". In: *Thin-Walled Structures* 48.1 (2010), pp. 25–32.

[140] E. Ramm. "Strategies for tracing the nonlinear response near limit points". In: *Nonlinear finite element analysis in structural mechanics*. Springer, 1981, pp. 63–89.

[141] J.N. Reddy. "A simple higher-order theory for laminated composite plates". In: *Journal of applied mechanics* 51.4 (1984), pp. 745–752.

[142] J.N. Reddy. *An Introduction to Nonlinear Finite Element Analysis: with applications to heat transfer, fluid mechanics, and solid mechanics*. OUP Oxford, 2014.

[143] W. Ren and W. E. "Heterogeneous multiscale method for the modeling of complex fluids and micro-fluidics". In: *Journal of Computational Physics* 204.1 (2005), pp. 1–26.

[144] A. Reuss. "Calculation of the yield point of mixed crystals". In: *Math. Mech* 9 (1929), p. 55.

[145] E. Riks. "An incremental approach to the solution of snapping and buckling problems". In: *International Journal of Solids and Structures* 15.7 (1979), pp. 529–551.

[146] A.J. Ritchey et al. *Micromechanics Simulation Challenge Level I Results*. 2015. URL: https://cdmhub.org/resources/948.

[147] M. Ritto-Corrêa and D. Camotim. "On the arc-length and other quadratic control methods: Established, less known and new implementation procedures". In: *Computers & Structures* 86.11-12 (2008), pp. 1353–1368.

[148] E. Sánchez-Palencia. "Non-homogeneous media and vibration theory". In: *Lecture notes in physics* 127 (1980).

[149] R. Schardt. "Generalized beam theory—an adequate method for coupled stability problems". In: *Thin-walled structures* 19.2-4 (1994), pp. 161–180.

[150] J. Schröder. "A numerical two-scale homogenization scheme: the FE^2 method". In: *Plasticity and Beyond*. Springer, 2014, pp. 1–64.

[151]   H.M. Sertse et al. "Challenge problems for the benchmarking of micromechanics analysis: Level I initial results". In: *Journal of Composite Materials* 52.1 (2018), pp. 61–80.

[152]   S.J. Song and A.M. Waas. "Effects of shear deformation on buckling and free vibration of laminated composite beams". In: *Composite Structures* 37.1 (1997), pp. 33–43.

[153]   A. Tchalla et al. "An ABAQUS toolbox for multiscale finite element computation". In: *Composites Part B: Engineering* 52 (2013), pp. 323–333.

[154]   K. Terada et al. "Simulation of the multi-scale convergence in computational homogenization approaches". In: *International Journal of Solids and Structures* 37.16 (2000), pp. 2285–2311.

[155]   R. Tezaur and C. Farhat. "Three-dimensional discontinuous Galerkin elements with plane waves and Lagrange multipliers for the solution of mid-frequency Helmholtz problems". In: *International journal for numerical methods in engineering* 66.5 (2006), pp. 796–815.

[156]   H. T. Thai and T. P. Vo. "Bending and free vibration of functionally graded beams using various higher-order shear deformation beam theories". In: *International Journal of Mechanical Sciences* 62.1 (2012), pp. 57–66.

[157]   J.M.T. Thompson and A.C. Walker. "The non-linear perturbation analysis of discrete structural systems". In: *International Journal of Solids and Structures* 4.8 (1968), pp. 757–768.

[158]   E. Tikarrouchine et al. "Three-dimensional FE^2 method for the simulation of non-linear, rate-dependent response of composite structures". In: *Composite Structures* 193 (2018), pp. 165–179.

[159]   S.P. Timoshenko and J.M. Gere. "Theory of elastic stability. 1961". In: *McGrawHill-Kogakusha Ltd, Tokyo* (1961), pp. 9–16.

[160]   Digimat Users'manual. *version 4.2. 1.* 2011.

[161]   R. Vescovini et al. "Buckling and wrinkling of anisotropic sandwich plates". In: *International Journal of Engineering Science* 130 (2018), pp. 136–156.

[162]   V.Z. Vlasov. "Thin-walled elastic beams". In: *PST Catalogue* 428 (1959).

[163]   V. Volovoi et al. "Applications of an asymptotic/modal approach for dynamical modeling of anisotropic beams". In: *39th AIAA/ASME/ASCE/AHS/ASC Structures, Structural Dynamics, and Materials Conference and Exhibit.* 1998, p. 2081.

[164]   G.A. Wempner. "Discrete approximations related to nonlinear theories of solids". In: *International Journal of Solids and Structures* 7.11 (1971), pp. 1581–1599.

[165]   J. Yang et al. "A new family of finite elements for wrinkling analysis of thin films on compliant substrates". In: *Composite Structures* 119 (2015), pp. 568–577.

120

[166]   K. Yu et al. "Multi-scale techniques to analyze instabilities in sandwich structures". In: *Composite Structures* 96 (2013), pp. 751–762.

[167]   W. Yu. "Structure genome: fill the gap between materials genome and structural analysis". In: *56th AIAA/ASCE/AHS/ASC Structures, Structural Dynamics, and Materials Conference.* 2015, p. 0201.

[168]   H. Zahrouni, B. Cochelin, and M. Potier-Ferry. "Computing finite rotations of shells by an asymptotic-numerical method". In: *Computer methods in applied mechanics and engineering* 175.1-2 (1999), pp. 71–85.

[169]   H. Zahrouni et al. "Asymptotic numerical method for strong nonlinearities". In: *Revue Européenne des Eléments* 13.1-2 (2004), pp. 97–118.

[170]   O.C. Zienkiewicz and R.L. Taylor. *The finite element method.* Vol. 36. McGraw-hill London, 1977.

[171]   T.I. Zohdi, J.T. Oden, and G.J. Rodin. "Hierarchical modeling of heterogeneous bodies". In: *Computer methods in applied mechanics and engineering* 138.1-4 (1996), pp. 273–298.

Curriculum Vitae

Name:	Yanchuan
Surname:	Hui
Gender:	Male
Date of birth:	24 September 1990
Place of birth:	Liaoning, China
e-mail:	yanchuan.hui@list.lu, yanchuan.hui@polito.it

Research Interests

⬦ Instability Phenomena of Heterogeneous Materials
⬦ Multi-scale Finite Element Method (FE^2)
⬦ Carrera's Unified Formulation

Education

⬦ EU Marie Curie fellow
Ph.D student in Mechanical and Aerospace Engineering, 2015- present
Politecnico di Torino, Italy
Supervisor: Prof. Erasmo Carrera
Luxembourg Institute of Science and Technology, Luxembourg
Supervisor: Dr. Gaetano Guinta, Dr. Salim Belouettar
⬦ Master-Ph.D student in Solid Mechanics, 2013-present,
Wuhan University, China
Supervisor: Prof. Heng Hu
⬦ Bachelor student in Engineering Mechanics, 2009-2013,
Wuhan University, China

Engineering Software Knowledge

⬦ FEM: ANSYS, ABAQUS
⬦ Mathematics: MATLAB

General Computer Skills

◇ OS: Linux, Windows, Mac OS
◇ Programming: Fortran, C++
◇ Office Software: LaTeX, MS Office

Language Proficiency

◇ Chinese: Native Speaker
◇ English: (IELTS 6.0) Good spoken and written
◇ Italian: Basic (A1) Basic words and phrases only

Publications

Journal Papers

◇ Y. Hui, G. De Pietro, G. Giunta, S. Belouettar, H. Hu, E. Carrera, A. Pagani, Geometrically non-linear analysis of beam structures via hierarchical one-dimensional finite elements, Mathematical Problems in Engineering, 2018.
◇ Y. Hui, G. Giunta, S. Belouettar, Q. Huang, H. Hu, and E. Carrera, A free vibration analysis of three-dimensional sandwich beams using hierarchical one-dimensional finite elements, 110: 7-19, 2017.
◇ G. De Pietro, Y. Hui, G. Giunta, S. Belouettar, E. Carrera, H. Hu, Hierarchical onedimensional finite elements for the thermal stress analysis of three-dimensional functionally graded beams, Composite Structures, 153: 514-528, 2016.
◇ Y. Hui, G. Giunta, S. Belouettar, H. Hu, E. Carrera, Multi-scale CUF-FE^2 Nonlinear Analysis of Beam Structures (under preparation).
◇ Y. Hui, G. Giunta, S. Belouettar, H. Hu, E. Carrera, Geometrically Nonlinear Analysis of Beam Structures via a Unified Formulation and the Asymptotic Numerical Method (under preparation).
◇ Y. Hui, G. Giunta, S. Belouettar, H. Hu, E. Carrera, A hygro-thermal stress finite element analysis of beam structures by hierarchical modelling (under preparation).

Book chapters

◇ Y. Hui, G. Giunta, S. Belouettar, H. Hu, E. Carrera, Multi-scale Nonlinear Analysis of Beam Structures by means of Carrera's Unified Formulation, Advances in Predictive Models and Methodologies for Numerically Efficient Linear and Nonlinear Analysis of Composites, Springer (submitted).

Conference proceedings

⬦ Y. Hui, G. De Pietro, G. Giunta, S. Belouettar, H. Hu, E. Carrera. Asymptotic numerical method for the analysis ofcomposite beams by Carrera's unified formulation. ICOMP2018, Wuhan, China, 2018.

⬦ R. Xu, Y. Hui, Q. Huang, H. Hu, H. Zahrouni, T. Ben Zineb, S. Zhu, A reduced model for handling the instabilities of long fiber reinforced composite with multilevel finite element method. ICMAMS2018, Torino, Italy, 2018.

⬦ Y. Hui, G. Giunta, G. De Pietro, S. Belouettar, H. Hu, E. Carrera, Hierarchical beam finite elements for multi-scale geometrically nonlinear analysis of beam structures via multi-scale asymptotic numerical method. ICMAMS2018, Torino, Italy, 2018.

⬦ Y. Hui, G. Giunta, G. De Pietro, R. Xu, S. Belouettar, H. Hu, E. Carrera, Multi-scale CUF-FE^2 Nonlinear Analysis of Beam Structures, DeMEASS2018, Sesimbra, Portugal.

⬦ G. De Pietro, G. Giunta, Y. Hui, S. Belouettar, E. Carrera, H. Hu, One-Dimensional Hierachical Modeling of Bistable Composite Beams, DeMEASS2018, Sesimbra, Portugal.

⬦ G. Giunta, G. De Pietro, Y. Hui, S. Belouettar, Newton's series expansion based theories in the framework of Carrera's Unified Formulation for the analysis of plates. ICMAMS2018, Torino, Italy, 2018.

⬦ G. De Pietro, G. Giunta, Y. Hui, S. Belouettar, H. Hu, E. Carrera, Geometrically nonlinear hierarchical finite elements for the analysis of bi-stable beam structures. ICMAMS2018, Torino, Italy, 2018.

⬦ Y. Hui, G. Giunta, S. Belouettar, E. Carrera, H. Hu, A hygro-thermal stress finite element analysis of laminated beam structures by hierarchical one-dimensional modelling. DeMEASS VII, Moscow, Russia, 2017.

⬦ Y. Hui, G. Giunta, S. Belouettar, E. Carrera, H. Hu, A multi-scale model of fibre reinforced beams using hierarchical one-dimensional finite elements. ICCS20, Paris, France, 2017.

⬦ Y. Hui, R. Xu, Q. Huang, H. Hu, A Fourier-related FE^2 Multiscale Model for Instability Phenomena of Long Fiber Reinforced Materials. WCCM & APCOM, Seoul, Korea, 2016.

⬦ Y. Hui, R. Xu, H. Hu, G. Giunta, S. Belouettar, A Novel FE^2 Method Based Fourier Macroscopic Model for Instability Phenomena of Long Fiber Reinforced Composites. ICCS19, Porto, Portugal, 2016.

Training Experience

Conferences

⬦ AIDAA 2015 Conference - XXIII Conference of the Italian Association of Aeronautics and Astronautics (Turin, Italy, 16-19 Nov 2015).

⬦ 19th International Conference on Composite Structures (Porto, Portugal, 5-9 September 2017).

⬦ International Conference on Composite Structures, (CNAM Paris, France, 4-7 September 2017).
⬦ 1st International Conference on Theoretical, Analytical and Computational Methods for Composite Materials and Composite Structures, (Wuhan, China, 23-25 May 2018).
⬦ 1st International Conference on Mechanics of Advanced Materials and Structures, (Turin, Italy, 17-20 June 2018).
⬦ 9th Design Modelling and Experiments of Advanced Structures and Systems (Sesimbra, Portugal, 30 September-3 October 2018).

Seminars

⬦ LIST PhD Day Seminar (Luxembourg, 8 December 2016).
⬦ The Future of Materials Summit, (Luxembourg Congres, Luxembourg, 13-14 November 2017).
⬦ LIST PhD Day Seminar, (LIST, Luxembourg, 30 November 2017)
⬦ LIST PhD Day Seminar (Luxembourg, 15 November 2018).

Workshops

⬦ Journèe de simulation numèrique (Metz, France, 8 July 2016).
⬦ 2nd Exploratory Workshop on Applications of Model Order Reduction Methods, (University of Luxembourg, Luxembourg, 10 March 2017).
⬦ Workshop on Advance in the Analysis and Design of Composite Structures (Politecnico di Torino, Italy, 2 May 2017).
⬦ Workshop on Manufacturing and Experimental Testing, (University of Bristol, UK, 19-21 June 2017).
⬦ 5th Workshop of Asymptotic Numerical Method, (LEM3 Metz, France, 27 November 2017).

Spring School

⬦ Spring School on the Computational Methods for the Analysis, Design and Failure of Composites, (CISM Udine, Italy, 3-7 April).

Soft Skill Courses

⬦ Leadership and communication course for researchers (Luxembourg, 11 June-23 July 2016).
⬦ Media training for researchers (Luxembourg, 16 June 2016).
⬦ Course on Self Management Techniques for Work Environment, (Politecnico di Torino,

Italy, May-June 2017).

⋄ Time management, (Politecnico di Torino, Italy, June 2018).

⋄ The new internet society: entering the black-box of digital innovations (Politecnico di Torino, Italy, June 2018).

⋄ Responsible research and innovation, the impact on social challenges (Politecnico di Torino, Italy, June 2018).

⋄ Self Management: techniques for work environment (Politecnico di Torino, Italy, June 2018).

⋄ Public Speaking (Politecnico di Torino, Italy, June 2018).

⋄ Entrepreneurial Finance (Politenico di Torino, Italy, June 2018).

⋄ Course on International Project Management in CFRP Development Programs, (Politecnico di Torino, Italy, June 2018).

⋄ Communication (Politecnico di Torino, Italy, June 2018).

⋄ Researchers at School-7th edition (Lycee Nic Biever Dudelange, Luxembourg, 27 March 2017).

⋄ Researchers at School-8th edition (École Européenne de Luxembourg I, Luxembourg, 23 March 2018).

Hard Skill Courses

⋄ Excellence course on Multiscale structural mechanics (Turin, Italy, November 2015).

⋄ Course on Mechanical Servosystems(Politecnico di Torino, Italy, May 2017).

⋄ Course on Linear viscoelasticity of materials (Politecnico di Torino, Italy, May 2017).

⋄ Course on Continuum damage model for composite materials, (Politecnico di Torino, Italy, July 2017).

⋄ Course on Numerical Methods in Geomechanics, (Politecnico di Torino, Italy, July 2018).

⋄ Course on Energy for Future Factories, (Politecnico di Torino, Italy, July 2018).

⋄ Lingua Italiana I livello (Politenico di Torino, Italy, July 2018).